THE EFFECTS OF SURFACE TENSION AND ENTANGLEMENTS IN POLYMER FILMS: CAPILLARY DRIVEN FLOWS, THE MARANGONI EFFECT AND CRAZING

THE EFFECTS OF SURFACE TENSION AND ENTANGLEMENTS IN POLYMER FILMS: CAPILLARY DRIVEN FLOWS, THE MARANGONI EFFECT AND CRAZING

By

PAUL D. H. FOWLER, B.Sc.

A Thesis
Submitted to the School of Graduate Studies
in Partial Fulfillment of the Requirements
for the Degree
Master of Science

McMaster University

MASTER OF SCIENCE (2014)
(Physics)

McMaster University
Hamilton, Ontario

TITLE: The effects of surface tension and entanglements in polymer films: Capillary driven flows, The Marangoni effect and crazing

AUTHOR: Paul D. H. Fowler, B.Sc. (McMaster University)

SUPERVISOR: Dr. Kari Dalnoki-Veress

NUMBER OF PAGES: ix, 82

Abstract

This is a ‘sandwich thesis’ consisting of four publications I contributed to during my M.Sc. work. These papers are the results of three types of experiments.

Paper 1 studies the formation of non-uniform spin-cast polymer films. Spincoating is widely used to prepare thin polymer films of reproducible thickness. Typically spincoating produces highly uniform films, however in certain circumstances the process results in films with non-uniform surface topographies. The origin of such topographies is not fully understood and the formation of non-uniform films represents a practical problem in both research laboratories and industrial settings. In Paper 1 we find that the formation of non-uniform films is dependent on temperature. Furthermore, our results indicate that surface instabilities form as a result of the Marangoni effect. Finally, we demonstrate that non-uniformities in spin-cast films can be avoided simply by spincoating at lower temperatures.

In Papers 2 and 3 we study the capillary driven levelling of polymer films with non-uniform surface geometries and compare our results to the theoretical predictions of the two-dimensional capillary-driven thin film equation. In Paper 2 we prepare polymer films with small surface perturbations and track their evolution above T_g as the surface flattens. We find that all perturbations approach a universal self-similar attractor at long times, as predicted by theory. Our results also show that the time taken for the perturbations to convergence to the attractor depends on the initial volume of the perturbation. In Paper 3 we prepare samples with a rectangular trench geometry and follow their evolution above T_g as surface forces cause the trench to fill in. At long times we observe a change in the levelling dynamics that is associated with a change in the boundary conditions governing the flow.

In Paper 4 we use crazing experiments to probe two types of non-equilibrium entanglement networks. First, we study spincast polymer films and find that chains are stretched compared to equilibrium Gaussian chains. Furthermore, we find that the entanglement network relaxes on timescale on the order of one reptation time. Next, we stack two films in the glassy state to create a bilayer. Chains on either side of the mid-plane of the bilayer suffer a loss of entropy because of their restricted conformations. In the melt, the interface heals. We find it takes less than one reptation time for the bilayer film to become indistinguishable from a single film.

Acknowledgements

It is rather ironic that this is perhaps the hardest part of the entire thesis to write. I suppose that's because distilling down the people who made this document possible in just a few paragraphs is nearly impossible. However, there is one clear place to start and that is with my supervisor Kari. It is unfair to call you just my supervisor because I counted on you for so much more than that. You have helped build my scientific career and your training and guidance have given me the opportunity to do extraordinary things. Working in your group made me a much better physicist but more importantly, it has made me a better person. For this, more than anything, I would like to say thank you.

To my friends, who were always there at the end of a frustrating day, thanks for making Hamilton home. Thanks for drinking beer and coffee with me. Thanks for going to shows. Thanks for standing in the baking heat in a crowded field with 10000 strangers getting tired and dehydrated with me; 2014 will forever be the year of the music festival. Friends, you saved my life too many times to count.

To my lab mates, thanks for making experiments fun and having a laugh and a beer when things went haywire. Thanks for letting me control the stereo. A special thanks to those who were not only my lab and office mates, but also my roommates. Congrats, none of us went insane. I would also like to extend a special thanks to Josh McGraw who taught me most of what I know in the lab. Your friendship and support in the early days helped make this document exist.

Finally, thanks to my family who were always there for me when I needed it most. To my parents, I wouldn't have finished this without you. You listened to me complain when I couldn't take it anymore and were also there to share my greatest joys. You have always done anything you possibly can to help me. You are incredible. Thank you, I love you.

Contents

List of Figures

Chapter 1

Introduction

One very interesting fact of nature is that a liquid interface takes on a shape that minimizes its surface area. Examples of this in our everyday life are numerous. After showering hair sticks together in order to minimize the surface area of the water/air interface. As rain falls onto the surface of a waxy leaf, the water beads up into nearly perfect spheres which take their shape to minimize the surface-to-volume ratio of the drop. In contrast to water beading up on a waxy surface, a thin liquid film on a wettable substrate will spontaneously flow until it reaches the equilibrium state of a perfectly flat film. All of these effects are a result of surface tension [1].

Surface tension can be simply thought of in terms of the energetic cost associated with having a liquid molecule at an interface. A molecule at an interface is missing some of its nearest neighbours and is therefore in a higher energy state compared to a molecule in the bulk of the liquid which is completely surrounded by fellow liquid molecules. Therefore, to minimize the free energy of the system, a liquid flows until the smallest possible number of molecules are exposed at the interface. While this is sufficient to explain the phenomena discussed above, on a very fundamental level surface tension is a concept that is surprisingly difficult to understand. Thinking about a liquid on the molecular scale introduces subtleties that complicate the simple picture described above.

Surface tension is the basis of the work presented in this thesis. In fact, it can be said that at the most fundamental level, all of the physics presented in Papers 1, 2 and 3 is ultimately a result of surface tension. In our case, the physics becomes further complicated by the fact that we perform experiments using thin polymer films, typically ~ 100 nm thick. Thin films have a drastically higher surface-to-volume ratio compared to bulk systems. Furthermore, since polymers are macromolecules on the order of $10 - 100$ nm is size, a polymer molecule in a thin film is confined to a system that is comparable to its molecular size. These two effects often result in interesting and surprising physics. Confinement effects are studied in Paper 4, the only paper in this work not directly related to surface tension. At the most fundamental level, the physics in Paper 4 results from the fact that polymers are long chain-like molecules which cannot pass through each other. This gives rise to entanglements which are like knots between polymer chains. Entanglements are responsible for many of the interesting properties observed in polymer systems such as a high melt viscosities and non-Newtonian flows.

In this thesis, the topics which have been briefly mentioned here will be explained in detail. Chapter 1 provides an overview of the physics required to understand the papers presented in this work. In particular, the focus is on polymer melts and entanglements. In Section 1.4 the thin film equation (TFE) which describes the surface tension driven flow for a thin liquid film with a non-uniform interface is derived. The TFE is central to the work presented in Papers 2 and 3. In Chapter 2 an overview of the experimental techniques used in each of the papers is presented. Since a full outline of the procedures is given in each paper, here the focus is on particular details that are not included in the papers but which may be useful to those attempting similar sample preparation techniques. Finally in Chapter 3 the four papers which comprise the bulk of this thesis are presented. First a brief summary of each paper is given, along with an outline of my particular contributions to the project. Following this, each paper is presented.

Paper 1 is about the preparation of thin polymer films. We study the formation of non-uniform films, which are a practical problem in both research labs and industrial settings. We present a simple technique to avoid the formation of non-uniform films which we are able to explain in terms of the Marangoni effect. In Papers 2 and 3 we study the surface tension driven levelling of a non-flat liquid interface. Our results are compared to the theoretical predictions of the TFE. Finally, in Paper 4 we study non-equilibrium entanglement networks in thin polymer films.

1.1 Polymers

One common thread of the work presented in this thesis is that all experiments were performed on polymeric systems. Polymers are macromolecules composed of repeating subunits called monomers that are joined together by covalent bonds. Polymers are ubiquitous in both technology and our daily lives. Naturally occurring polymers include DNA and proteins while synthetically produced polymers range from rubbers to glues and resins. Polymers can be prepared with a wide variety of molecular architectures including rings, stars, combs and random networks. In this thesis we are concerned with the physics of linear polymers which are formed by successively linking together monomeric units to create a long chain-like molecule.

One common example of such a molecule, polystyrene, is depicted in Fig. 1.1. Here, the monomer unit is styrene and N refers to the degree of polymerization - the number of monomers linked together to form the polymer chain. Although the type of monomeric unit influences the properties of the molecule, all polymers share a number of universal physical properties resulting from their long chainlike structure. Furthermore, the size of a polymer molecule is amongst the most important factors affecting its physical properties [2]. The size of a polymer molecule can be characterized by its end-to-end distance (R_{ee}) - the distance between the two ends of the molecule.

The molar mass of the molecule is defined as $M = mN$ where m is the molec-

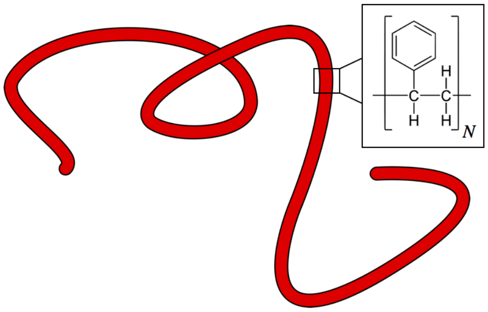

Figure 1.1: Schematic of a polystyrene molecule. The long chain-like molecule is composed of many styrene monomers covalently bonded together. The degree of polymerization, N refers to the number of monomeric units linked together to form the chain.

ular mass of a monomer unit. In this work, we are concerned with linear polymers composed of only one type of monomer unit, so M can be thought of as simply the length of the polymer backbone. For a polymeric system composed of many chains we must consider the fact that typical polymerization processes used to synthesize polymer molecules result in chains with varying lengths. If we consider a polymer sample with some distribution of chain lengths, the average length is most commonly defined using either the number average, M_n or the weight average, M_w

$$M_n = \frac{\sum\limits_i n_i M_i}{\sum\limits_i n_i} \tag{1.1}$$

$$M_w = \frac{\sum\limits_i w_i M_i}{\sum\limits_i w_i} = \frac{\sum\limits_i n_i M_i^2}{\sum\limits_i n_i M_i}. \tag{1.2}$$

Here n_i is the number of chains with molar mass M_i and we have defined $w_i = n_i M_i$ (the total mass of molecules with molar mass M_i). M_n represents the first moment of the distribution while M_w is the second moment. The polydispersity index, defined as $\mathrm{PI} = M_w/M_n$ is a measure of the uniformity of chain lengths in the sample. A polymeric system in which every chain has the same length is perfectly monodisperse and has $\mathrm{PI} = 1$. Research grade polymer of the type used in this thesis typically has $\mathrm{PI} < 1.1$ and polydispersity effects are safely ignored.

Throughout this work I will distinguish between polymer melts and glasses. At high temperatures, a polymer system is found in a liquid state known as a melt. The system possesses a large amount of kinetic energy and on a microscopic level, individual polymer chains are continuously exploring new configurations through their thermal fluctuations. On a macroscopic level, a polymer melt exhibits a highly viscous flow over long time scales but behaves like an elastic solid on short time scales. The details of polymer melts will be further discussed in Section 1.2.

At low temperatures, a polymer system is most often found in the glassy state [1].

---

[1] It should be noted that some polymers can also form crystalline or semicrystalline structures. Most polymers do not readily crystallize because of the inherent disorder within the molecule arising from the random orientation of side groups along the backbone of the chain. However, if the side groups are regularly ordered (for example isotactic polymers for which all of the side groups are on same side of the backbone), upon cooling the melt, the system may crystallize. None of the polymers used in this thesis readily crystallize.

In the glassy state, individual polymer chains do not exhibit long range motion. Mechanically, a polymer glass behaves like a solid, however the molecules in the glass do not exhibit any long range order [3]. We can imagine the molecular structure of a polymer glass is like a melt (liquid) but with the chains frozen in place. One everyday example of a polymer glass is a polystyrene coffee cup. Transitions between the glassy state and the melt state occur at the glass transition temperature, T_g. Most experiments in this thesis were performed using polystyrene which has a glass transition temperature of approximately 100°C [4].

1.2 Polymer melts

In Section 1.1 it was mentioned that a polymer melt behaves as an elastic solid on short time scales and a highly viscous liquid on long time scales. This effect known as viscoelasticity will be discussed in Section 1.2.3. We first address the question, what is the molecular conformation of a polymer chain in the melt? Consider a chain with a degree of polymerization N where each monomeric link in the backbone has length a. As shown schematically in Fig. 1.2, the end-to-end vector, $\mathbf{R_{ee}}$ is the sum of the N bond vectors along the chain, $\mathbf{a}_i$, which represent the orientation of each monomer unit: $\mathbf{R_{ee}} = \sum_{i=1}^{N} \mathbf{a}_i$. On short length scales, the orientation of monomer segments may be correlated. However, these correlations typically decay very rapidly (fewer than 10 segments for most polymers [4]) and there is no correlation between widely separated segments of the chain. We now consider a simple model where the real polymer chain is broken into $\mathcal{N}$ segments of length b, where b is greater than the length scale over which the segments a_i are correlated. When b is chosen in this manner, the $\mathcal{N}$ segments of length b are uncorrelated and free to orient in random directions [4]. We also note that the length scale b, which is known as the Kuhn length is chosen such that the real and model chain have the same contour length and end-to-end distance: $L = Na = \mathcal{N}b$ and $\mathbf{R_{ee}} = \sum_{i=1}^{N} \mathbf{a}_i = \sum_{i=1}^{\mathcal{N}} \mathbf{b}_i$. Therefore the real chain is entirely equivalent to the ideal freely jointed chain and the Kuhn length is uniquely defined.

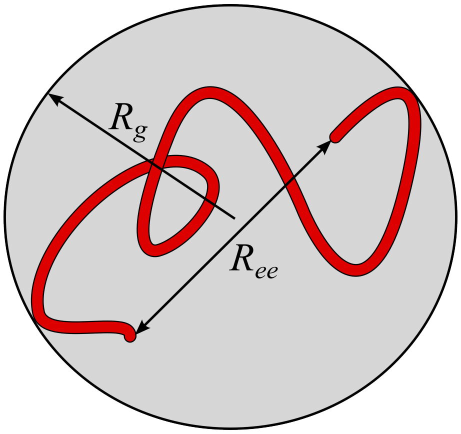

Figure 1.2: Schematic of the dimensions of a polymer chain in the melt. A polymer molecule in the melt is accurately described as a random walk and the end-to-end distance of the molecule (R_{ee}) scales with molecular wight as $R_{\mathrm{ee}} \sim M_w^{1/2}$. It can be shown that the radius of gyration (R_g) is related to R_{ee} by $R_g = R_{\mathrm{ee}}/\sqrt{6}$. The pervaded volume is a sphere which envelops the chain: $V_p \sim {R_g}^3 \sim {R_{ee}}^3$.

If we now consider the average end-to-end distance of a such chain, we have

$$\begin{aligned} {R_{\mathrm{ee}}}^2 = \langle \mathbf{R_{ee}} \cdot \mathbf{R_{ee}} \rangle &= \left\langle \left(\sum_{i=1}^{\mathcal{N}} \mathbf{b}_i \cdot \sum_{i=1}^{\mathcal{N}} \mathbf{b}_i \right) \right\rangle \\ &= \left\langle \sum_{i=1}^{\mathcal{N}} \sum_{j=1}^{\mathcal{N}} \mathbf{b}_i \cdot \mathbf{b}_j \right\rangle \\ &= \mathcal{N} b^2 + \left\langle \sum_{i \neq j}^{\mathcal{N}} \mathbf{b}_i \cdot \mathbf{b}_j \right\rangle . \end{aligned} \tag{1.3}$$

Since the chain is freely jointed, the orientation of different monomers is uncorrelated and the cross terms disappear leaving

$${R_{\mathrm{ee}}}^2 = \mathcal{N} b^2. \tag{1.4}$$

Finally, noting that $\mathcal{N} \sim N \sim M_w$ we have,

$$R_{\mathrm{ee}} \sim \sqrt{N} \sim \sqrt{M_w}. \tag{1.5}$$

The above formalism relies on the assumption that on average, there is no interaction between chain segments that are widely separated. This is valid for the melt. In the melt each chain is surrounded by many other chains and interactions between monomers on the same chain are indistinguishable from interactions between chains [2]. Neutron scattering experiments have confirmed that the conformation of a chain in the melt is accurately described as a random walk [5,6]. This fundamental result underlies a great deal of modern polymer theory and offers a simple model to quantitatively describe the behaviour of polymer melts [4].

As shown in Fig. 1.2, the dimensions of a polymer chain can also be described in terms of the radius of gyration, R_g, which is defined is as the root mean square distance of the monomers from the molecule's centre of mass. For a linear polymer chain it can be shown that the radius of gyration is simply related to the end-to-end distance as $R_g = R_{ee}/\sqrt{6}$ [4]. For polymer molecules with non-linear architectures, the end-to-end distance is often poorly defined and R_g is a more useful measure of molecular size. Finally, as depicted in Fig. 1.2, the pervaded volume, V_p, is a measure of the space explored by a polymer chain through its random walk and is typically defined as either a sphere of radius R_{ee} or R_g: $V_p \sim {R_g}^3 \sim {R_{ee}}^3 \sim {M_w}^{3/2}$.

Now imagine stretching a single polymer chain so that it has end-to-end distance $r > R$ where $R = a\sqrt{N}$ is the unperturbed end-to-end distance. How does the chain respond? It can be shown using elementary statistical mechanics that the distribution of possible end-to-end vectors (or radii of gyration) is Gaussian. Therefore the probability of finding a chain with end-to-end vector $\mathbf{r}$ is given by [4]

$$P(\mathbf{r}) = \left(\frac{3}{2\pi R^2}\right)^{3/2} \exp\left(\frac{-3r^2}{2R^2}\right). \tag{1.6}$$

Noting that $P(\mathbf{r}) = \Omega(\mathbf{r})/C$ where $\Omega(\mathbf{r})$ is the number of random walks with end-to-end vector $\mathbf{r}$ and C is a numerical constant representing to total number of possible chain configurations, using Eq. 1.6 we can can write the entropy of a single chain as

$$S(\mathbf{r}) = k \ln \Omega = S_o - k\left(\frac{3r^2}{2R^2}\right) \tag{1.7}$$

where S_o is a numerical constant and k is Boltzmann's constant. The free energy of the chain is given by

$$F(\mathbf{r}) = U - TS = U - TS_o + \frac{3kTr^2}{2R^2}. \tag{1.8}$$

In our model the internal energy, U, is independent of chain conformation so the change in free energy upon stretching the chain is

$$\Delta F = F(\mathbf{r}) - F(\mathbf{R}) = \frac{3kTr^2}{2R^2} + \text{const}. \tag{1.9}$$

Therefore, the force required to stretch the chain is

$$f = -\frac{\partial \Delta F}{\partial r} = -\frac{3kTr}{2R^2}. \tag{1.10}$$

Qualitatively, this allows us to think of a polymer chain like a Hookean entropic spring. If a chain is stretched or compressed away from its ideal random walk conformation there is an entropic restoring force proportional to the deformation, resulting from the decreased entropy of the chain. Simply put, perturbing a polymer chain away from its random walk reduces its number of possible configurations. In an entangled melt, or cross-linked rubber, the network made up of these interconnected Hookean springs results in non-linear elasticity [3]. This will be discussed in detail in Section 1.2.3.

1.2.1 Entanglements

Above, we defined the space occupied by the random walk configuration of a polymer chain in the melt as the pervaded volume, $V_p \sim R_{ee}^3 \sim N^{3/2}$. Within a sphere of radius R_{ee} the volume occupied by a single chain is given by $V_c \sim N$. Therefore, the fraction of space filled by a single polymer chain in its own pervaded volume, $V_c/V_p \sim N^{-1/2}$ is small since $N > 100$ for a typical polymeric system. Polymer melts fill space so a consequence of this fact is that many chains must share the same pervaded volume. Therefore, in the melt there are many interactions between chains.

To emphasize this point, consider a typical polymeric system, polystyrene (PS) of $M_w = 10^6$ g/mol. For PS it has been measured that $R_{ee}/M_w = 5.4 \times 10^{-3}$ nm^{2}mol/g [4, 7]. Using this we calculate, $R_{ee} = \sqrt{(5.4 \times 10^{-3})(10^6)} \approx 74$ nm. The pervaded volume of the chain is $V \sim \frac{4}{3}\pi {R_{ee}}^3 \approx 1.6 \times 10^6$ nm^3. The mass of a single chain is

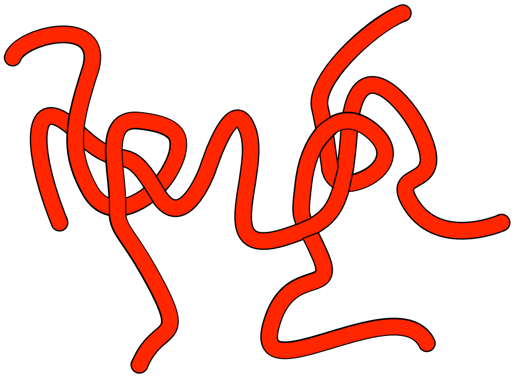

Figure 1.3: Schematic of polymer entanglement. Although the exact molecular conformations giving rise to entanglements remain unknown, it has been established that the topology of the contact is important. As a simple picture, we can imagine that entanglements are like knots between chains. The entanglement molecular weight, M_e is defined as the average mass of chain between entanglements.

given by $m_c = 10^6/N_A$ where N_A is Avagadro's number.

Therefore the density of a single chain in the pervaded volume is $\rho_c = m_c/V \sim 1$ kg/m^3. But the density of PS in the melt is $\rho = 1000$ kg/m^3 [4]. So the number of chains sharing the same volume is $\rho/\rho_c \sim 1000$. We note that since the density of the melt is constant and independent of N, it follows that longer chains interact with each other more frequently than shorter chains.

The fact that there are many interactions between chains results in the phenomenon of entanglement. When two chains share the same pervaded volume, they may take on a conformation that severely restricts the movement of the chains in the direction perpendicular to their backbones [2]. Such conformations are referred to as entanglements. On a fundamental level, entanglements arise due to the simple fact that polymer backbones cannot pass through one another. Although the precise molecular configurations giving rise to entanglements are unknown [8], as a simple picture, we can think of entanglements as knots between polymer chains, as depicted in Fig. 1.3. It is important to note that in the melt, polymers are constantly exploring new space meaning entanglements represent temporary constraints. Many of the physical properties exhibited by polymer melts including viscoelasticity and high viscosities are a result of entanglements [2].

Before proceeding to discuss some of the physical phenomena resulting from entanglements, we will briefly explain the entanglement molecular weight, M_e which is defined as the average molecular weight between two entanglements. In Fig. 1.3, M_e represents the mass of the chain between the two knots. Related to M_e is the entanglement density, ν_e, the number of entanglements per unit volume [2]:

$$M_e \propto \frac{1}{\nu_e}. \tag{1.11}$$

It is important to note that in order for polymer chains to entangle, they must have some minimal length [2]. M_e can also be thought of as the minimum chain length required to form entanglements. As an analogy, imagine holding two pieces of string. If the strings are very long it is easy to knot them together. As the length of the strings becomes smaller, it becomes more and more difficult to a to tie a knot between the strings. We can imagine that at some point, the length of the strings will become so short that it is impossible to knot them together. The shortest possible length of string we can knot represents the entanglement molecular weight.

The onset of entanglement is experimentally observed through measurements of viscosity. As discussed above, entanglements restrict the motion of polymer chains and therefore increase the viscosity of the melt. Above M_e the viscosity of a polymer melt, η, scales as $\eta \sim {M_w}^{3.4}$ [4]. Below M_e, $\eta \sim M_w$ and the viscosity of the melt is simply attributed to the friction of polymer chains sliding past one another.

1.2.2 Tube model and reptation

The dynamics of an entangled polymer melt can be explained using the tube model and the concept of reptation which was originally proposed by de Gennes, Edwards and Doi [3]. Using the basic principle that no chains can pass through one another, we can consider each polymer chain to be confined to a tube, as shown in Fig. 1.4. If we consider a single chain in the melt, other chains represent obstacles restricting its motion. Entanglements with other chains, which are represented as $\times$ in Fig. 1.4(a) define a tube of diameter d. Motion of the chain perpendicular to the tube is severely restricted by these entanglements, but the chain is able wriggle back and forth along the tube like a two-headed snake or worm. This type of wriggling motion is referred to as reptation [2]. If we imagine entanglements with other chains as fixed obstacles,

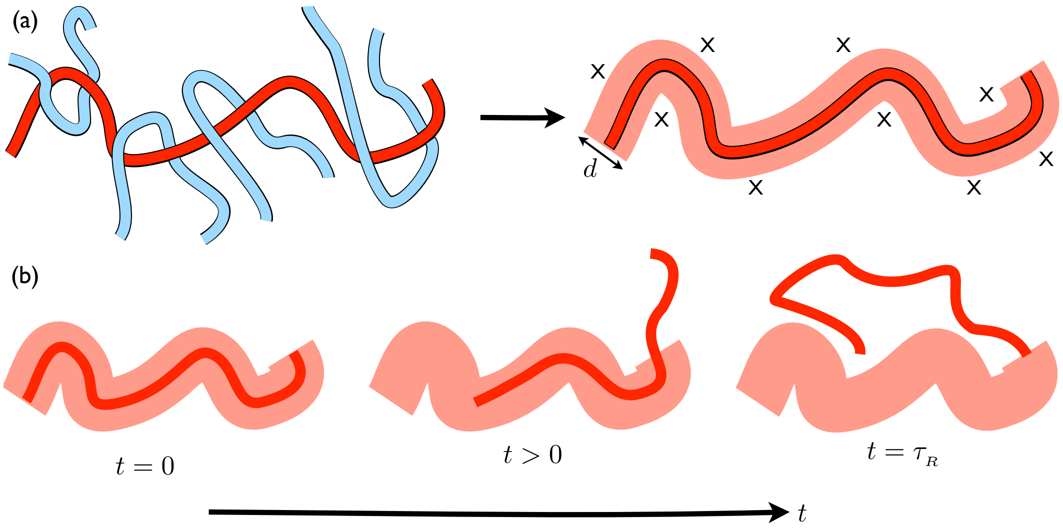

Figure 1.4: Schematic of the tube model and reptation. (a) For the red 'test chain', entanglements with other chains represent obstacles restricting motion. We can imagine that the 'test chain' is confined to a tube of diameter $d \sim M_e^{1/2}$. Motion perpendicular to the tube is hindered by entanglements, which are represented with the symbol $\times$ but the chain is free to reptate along the tube like a snake. (b) At $t = 0$ we define a tube and assume that the constraints which determine this tube remain fixed. For $t > 0$ the chain reptates and 'forgets' some of the original tube. At some point, the chain will have completely forgotten the tube defined at $t = 0$. This time, averaged over many such chains, is the reptation time, τ_R.

the time it takes a polymer chain to reptate out of its tube is called the reptation time, τ_R.

To further understand this picture imagine we take a snapshot of a polymer melt and call this $t = 0$. If we look at a single 'test chain' at $t = 0$, we can define its tube by viewing the other chains in the system as obstacles. Now let us assume that all chains are frozen in place except for the test chain which is free to reptate along its tube. As time proceeds the test chain will begin to wriggle out of the tube it was originally constrained to. The time it takes for the test chain to completely leave the tube we defined at $t = 0$ is the reptation time. This process is depicted schematically in Fig. 1.4(b).

In this picture we are heavily relying on the assumption that the test chain's constraints remain fixed over time. In reality this is not true. Since other chains are also moving, as time progresses new constraints form while others relax. Therefore we have two competing mechanisms - the diffusion of the chain within its tube and the renewal of obstacles. P. G. de Gennes showed that reptation is faster than the decay of constraints which validates the tube picture described above [2]. Experiments have also validated the reptation model [9, 10]. From the point of view of the 'test chain' entanglements with other chains represent permanent obstacles on short times, $t < \tau_R$.

To calculate the reptation time, first recall from Section 1.2.1 that we defined the entanglement molecular weight as the average mass of chain between entanglement points. If we assume that a chain has an entanglement every $N_e \sim M_e$ segments then since the chain is a random walk, the distance between entanglement points is $d \sim bN_e^{1/2}$. This determines the tube diameter. For chain motion on length scales smaller than d, entanglements are not noticed but for motions on length scales larger than d, the chain is restricted by other chains and 'feels' its tube. This picture leads us to the blob model originally developed by de Gennes [2]. We can imagine breaking the chain down into blobs of diameter d, each of which contains on average N_e segments. The blobs define the tube and within each blob, the chain is simply an ideal coil. It is important to emphasize that the blobs do not exclude one another.

The primitive path of the tube, which can be thought of as the length of a curved line passing through the centre of the tube, is simply the number of blobs multiplied by the size of each blob. As mentioned above the size of each blob is given by $d \sim bN_e^{1/2}$ and there must be N/N_e blobs so

$$\Lambda = d\frac{N}{N_e} = b\frac{N}{\sqrt{N_e}}. \tag{1.12}$$

Since the wriggling of the chain along its tube is governed by Brownian motion, the reptation time can be estimated using Einstein's relation which expresses the diffusion constant (D) in terms of a friction coefficient (ζ): $D = kT/\zeta$. For the chain within the tube, the friction results from its monomers sliding past other chains in the melt. If we define μ as the monomeric friction coefficient then the total friction felt by the chain is $\zeta = N\mu$ and we have $D = kT/N\mu$. Viewing the motion of the chain as a 1-D Browning particle, we can write the mean squared displacement as $\langle x^2 \rangle = 2Dt$. The reptation time, τ_R, is the time it takes the chain to diffuse a distance of its primitive path, Λ, so we have

$$\Lambda^2 = 2D\tau_{_R}. \tag{1.13}$$

Substituting Eq. 1.12 into the above relation and solving for $\tau_{_R}$ gives

$$\tau_{_R} \sim \frac{b^2\mu}{kT}\frac{N^3}{N_e}. \tag{1.14}$$

One of the most important results of the reptation theory is the prediction $\tau_{_R} \sim N^3 \sim M^3$.

1.2.3 Viscoelasticity

In previous sections we have briefly mentioned the fact that a polymer melt exhibits properties of both an elastic solid and a viscous liquid. In particular, when a stress is applied to a polymer melt the response is dependent on the time scale over which the stress is applied. Here, we fully explain this phenomenon which is known as viscoelasticity.

Suppose a shear stress, σ is applied to the melt. The simplest model of viscoelasticity assumes that on short timescales ($t < \tau_{_R}$) the system behaves like a Hookean solid while on long timescales ($t > \tau_{_R}$) the melt flows like a Newtonian liquid. That is on short timescales, the applied stress σ results in a shear strain ϵ. The strain is proportional to the applied stress, $\sigma = G\epsilon$ where G is the shear modulus. On long timescales, the applied stress results in a flow with a constant strain rate, $\sigma = \eta\dot{\epsilon}$ where η is the viscosity. At every point in the liquid the shear strain rate is proportional to the viscous stresses induced by the flow. More simply, the viscosity is independent of the shear stress.

In Fig. 1.5 is shown the response of a viscoelastic material to a step stress: a shear stress (σ) applied at $t = 0$ and held constant. From this plot we note that equating the slopes at $\tau_{_R}$ gives the important approximation relationship

$$\eta \approx G\tau_{_R}. \tag{1.15}$$

The viscoelastic response of a polymer melt is an effect of entanglement [2]. When

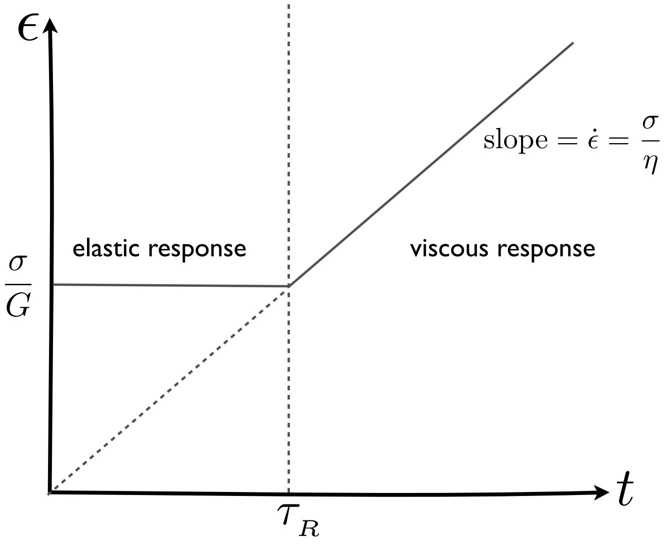

Figure 1.5: A stress σ is applied to a polymer melt at $t = 0$ and held constant. Initially the melt behaves as an elastic solid: $\sigma = G\epsilon$. At long times the melt flows as a Newtonian liquid: $\sigma = \eta\dot{\epsilon}$. The boundary between the elastic and viscous regimes is τ_R.

a stress is rapidly applied to a polymer melt, qualitatively we can imagine that entanglements behave like temporary cross-links, restricting the motion of individual polymer chains, and making it difficult to deform the system [3]. If a stress is applied on timescales longer than τ_R, polymer chains are able to move over larger distances, establishing flow. With this picture in mind, it is natural that τ_R is the boundary between the viscous and elastic regimes. For a good example of the viscoelastic effects in a polymer melt, consider Silly Putty. If we roll Silly Putty into a ball and drop it onto the floor, it bounces: an elastic response. If we then place the ball of Silly Putty on the table, it will gradually flow into a pancake shape: a viscous response.

Now, let us further consider the elasticity of the melt. In Section 1.2, we showed that a polymer chain behaves as an entropic spring. When a chain is deformed away from its ideal random walk conformation, there is a restoring force resulting from the chain's loss of entropy. At a fundamental level, the elastic response of the melt is a result of this loss of entropy. As mentioned above, on short timescales we can imagine that entanglements behave like permanent cross-links. This means that on timescales, $t < \tau_R$, we can treat the melt as a rubber (a cross-linked polymer network) with a cross-link density equal to the entanglement density, ν_e. In this way, the elastic response can be explained using the idea of rubber elasticity.

The theory of rubber elasticity assumes that between cross-links the chains are ideal. Therefore we can treat the system as a network of Gaussian 'sub-chains' with length proportional to M_x where $M_x = mN_x$ is the mass of chain between cross-links and N_x is the number of monomers between cross-links. When a stress is applied to the rubber, each sub-chain exerts an entropic restoring force governed by Eq. 1.10. It can be shown that for an affine deformation, the tensile stress (Q) and extensional strain (e), obey the relation

$$Q = \frac{\rho N_A kT}{M_x}\left[(1+e) - \frac{1}{(1+e)^2}\right] \tag{1.16}$$

where ρ is the density and N_A is Avagadro's number. Expanding the above equation for small strains gives $Q \approx (3\rho N_A kT/M_x)e$ so we can estimate the Young's modulus as

$$E \equiv \frac{Q}{e} = \frac{3\rho N_A kT}{M_x}. \tag{1.17}$$

If we assume incompressibility (the density of the rubber does not change for small stresses), then since the rubber is homogenous and isotropic, the shear modulus is simply related to the Young's modulus by $G = E/3$ [3] which gives

$$G = \frac{\rho N_A kT}{M_x}. \tag{1.18}$$

As previously emphasized, on short timescales ($t < \tau_R$) the melt behaves like a rubber with a cross-link density equal to the entanglement density. Therefore, in analogy with Eq. 1.18 we can write the shear modulus of the melt as

$$G_m = \frac{\rho N_A kT}{M_e} \tag{1.19}$$

by simply replacing M_x with the entanglement molecular weight, M_e. It is important to remember that although we are making the assumption that entanglements behave as permanent cross-links over short timescales, entanglements are not permanent and relax on a timescale on the order of τ_R.

Finally, recalling Eqs. 1.14 and 1.15 the above expression for the elastic modulus of the melt allows us to write

$$\eta \approx G_m \tau_{_R} \sim \frac{{M_w}^3}{{M_e}^2} \tag{1.20}$$

The prediction $\eta \sim {M_w}^3$ is a fundamentally important scaling relation in polymer physics and has been tested numerous times using a variety of experimental techniques [4, 11–14]. Experimentally it is found that, $\eta \sim {M_w}^{3.4}$. The slight discrepancy between theory and experiment remains an important unsolved problem in polymer physics [2].

Before proceeding from our discussion of polymer melts, we will briefly consider the effect of temperature on viscosity, which is important for Papers 2, 3 and 4. It has been empirically determined that viscosity depends exponentially on temperature according to

$$\eta(T) = \eta_{_0} \exp\left(\frac{T_A}{T - T_V}\right) \tag{1.21}$$

where $\eta_{_0}$ and T_A are constants which depend the type of polymer and its M_w and T_V is the Vogel-Fulcher temperature. T_V can be determined experimentally and is usually found to be about 50° C below the glass transition temperature [4]. Eq. 1.21 is referred to as the Vogel-Fulcher law. It is simple to show that the Vogel-Fulcher law is equivalent to the so-called Williams-Landel-Ferry (WLF) equation

$$a_T = \frac{\eta(T)}{\eta(T_0)} = \exp\left(B_0 \left[\frac{T_0 - T}{T - T_V}\right]\right). \tag{1.22}$$

Here B_0 is a numerical constant and $\eta(T_0)$ is the viscosity at some reference temperature T_0. Eq. 1.22 is central to the time-temperature superposition principle which says for some viscoelastic property of the melt, F, that depends on time and temperature (for example creep or relaxation modulus) we can write

$$F(t, T) = F(a_T t, T_0) \tag{1.23}$$

where a_T is defined as above and referred to as the shift factor and T_0 is a reference temperature. Note that since $\eta \sim \tau_{_R}$ we can write $a_T = \eta(T)/\eta(T_0) = \tau_{_R}(T)/\tau_{_R}(T_0)$. This means that for a polymer melt, increasing the temperature is equivalent to waiting a longer time for viscous flow to occur. In general, when applying the time temperature superposition principle, the reference temperature is typically chosen as T_g [4].

1.3 Crazing

When a strain is applied to an unentangled polymer glass, the polymer may fracture much like a pane of window glass. However, for entangled polymer systems, applying a strain in the glassy state may result in the formation of crack-like structures called crazes [15, 16]. As a common example of craze formation, imagine slowly stretching a plastic bag. A crazed plastic bag is shown in Fig. 1.6. The deformed regions of material, which appear lighter than the undeformed plastic are crazes.

Crazes form as a mechanism to dissipate energy in response to an applied stress. On a molecular level, the strain causes individual polymer chains to stretch which results in a thinning of the material [15]. The details of craze nucleation and growth have been extensively studied and it has been established that crazes can be characterized by their extension ratio, λ, which is the ratio of the width of the craze, to the width of the undeformed material that went into forming the craze [17–19]. Furthermore, it has been shown that the width of craze is not correlated with its

Figure 1.6: Slowly stretching a plastic bag may lead to the formation of crazes. In this picture, the crazes are the deformed regions of material which appear lighter in colour than the undeformed plastic.

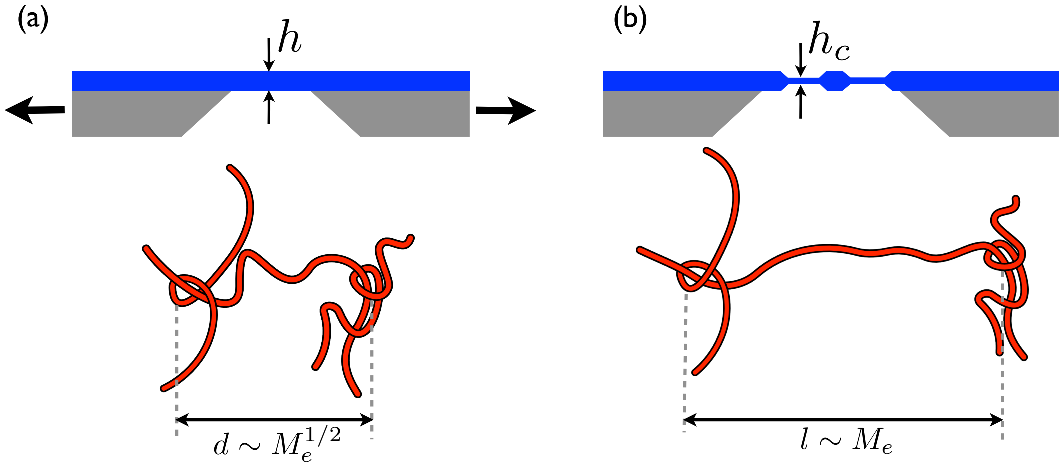

Figure 1.7: Schematic of a crazing experiment. (a) A freestanding film of thickness h is suspended across two blocks which are pulled apart to strain the film. Before crazing the distance between entanglements is $d \sim M_e^{1/2}$. (b) The strain causes the film to craze. The deformed regions of material have thickness $h_c < h$. Within the craze, the chains have been stretched such that the distance between entanglements is $l \sim M_e$.

height, h_c [15, 20]. This can be understood by considering the fact that once the chains within the craze have reached a certain level of deformation, it is mechanically easier to draw new chains into the craze rather than continuing to stretch the already deformed material. In other words, once a craze has nucleated, the width of the deformation continues to grow by drawing undeformed material into the craze, thereby causing an increase in the volume of crazed material and a decrease in the volume of undeformed material.

Although crazing experiments were initially used to study the mechanical properties of polymer glasses, in pioneering work by Donald and Kramer it was shown that crazing may be used to elucidate properties of the entanglement network [17, 21]. Recent work has used the technique of crazing to probe entanglement properties in thin polymer films [22, 23]. Fig. 1.7 shows the setup of a typical crazing experiment. A polymer glass of thickness h is suspended between two supports and then strained until crazes form. As shown in Fig. 1.7 the deformed regions of material have thickness $h_c < h$ and within the craze the chains are highly stretched as compared to their equilibrium Gaussian conformation.

The fundamental assumption made by Donald and Kramer is that since crazing occurs deep in the glassy state, entanglements act as cross-links which remain fixed during the crazing process. This assumption has been extensively verified by experiments [15–17, 21] and has also been validated with computer simulations [24, 25]. Before crazing, the chains within the undeformed film take on random walk conformations so the distance between entanglements is given by

$$d \propto {M_e}^{\frac{1}{2}}. \tag{1.24}$$

After crazing, if we assume that the chains within the deformed material are maximally stretched (an assumption which was validated in [17, 20]) then the distance between entanglements is

$$l \propto M_e. \tag{1.25}$$

Using conservation of volume and assuming that the extension ratio of the craze is the same as that of the polymer chains we have

$$\frac{h_c}{h} \propto \frac{d}{l} \propto \frac{\sqrt{M_e}}{M_e} \propto \frac{1}{\sqrt{M_e}}. \tag{1.26}$$

Noting that $\nu_e \propto 1/M_e$ (Eq. 1.11), the above equation tells us

$$\left(\frac{h_c}{h}\right)^2 \propto \nu_e. \tag{1.27}$$

Equation 1.27 is the fundamental crazing relationship used in Paper 4. We emphasize that h_c and h are measurable *macroscopic* quantities. Therefore, crazing experiments allow us to directly infer the details of *molecular* chain conformations through macroscopic measurements. It is also worth reinforcing that crazing experiments are performed deep in the glassy state, meaning chain entanglements can be thought of as permanent knots between polymer chains. Since chain conformations in the glassy state are inherited from either the melt state or through the process of spin coating which will be discussed in Section 1.5.1, crazing experiments offer a robust way to probe entanglement effects in thin polymer films. The experiments presented in Paper 4 use the technique of crazing to study the evolution of two types of non-equilibrium entanglement networks.

1.4 Surface tension

It is not an exaggeration to say that on the most fundamental level, all the physics studied in Papers 1, 2 and 3 arises because of surface tension. The phenomenon of surface tension is often thought of in terms of the energetic cost associated with increasing the surface area of a liquid [26]. To understand why it costs energy to create surface, we must examine a liquid at the molecular scale. As shown in Fig. 1.8 a molecule in the bulk of the liquid feels a cohesive interaction with each of its nearest neighbours. However, a molecule at the surface of the liquid is missing some of its nearest neighbours and thus some of its cohesive interactions. Therefore, molecules at the surface are in a higher energy state compared to those in the bulk of the liquid. To minimize the free energy of the system, the liquid interface will take the shape that minimizes the number of molecules exposed at the surface. This is the reason that liquids flow in order to minimize their surface-to-volume ratio.

A more rigorous description comes from considering the Leonard-Jones potential which describes the interaction energy between two molecules separated by a distance r [3]. At short ranges there is a repulsive Coulombic interaction that scales as $\sim r^{-12}$, which arises due to the overlapping of electron clouds. At long ranges there is an attractive force resulting from van der Waals interactions which goes as $\sim r^{-6}$. The van der Waals interactions stem from instantaneous dipole moments which appear due to fluctuations in a molecule's electron distribution. This dipole then induces a dipole on a neighbouring molecule, causing an attraction between them.

The total interaction potential, shown in Fig. 1.8(b) is a combination of the two effects described above: the long range van der Waals interaction and the short range Coulombic repulsion. It is favourable for molecules to be separated by a distance which corresponds to the minimum in the potential, U_0. Therefore, a molecule at the surface which is missing half its cohesive interactions will have approximately $U_0/2$ excess energy. The surface tension is a measure of the extra energy per unit area so if we assume a molecular size of a then the molecule's surface area goes as a^2 and we approximate the surface tension as $\gamma \approx U_0/2a^2$. The surface tension is more

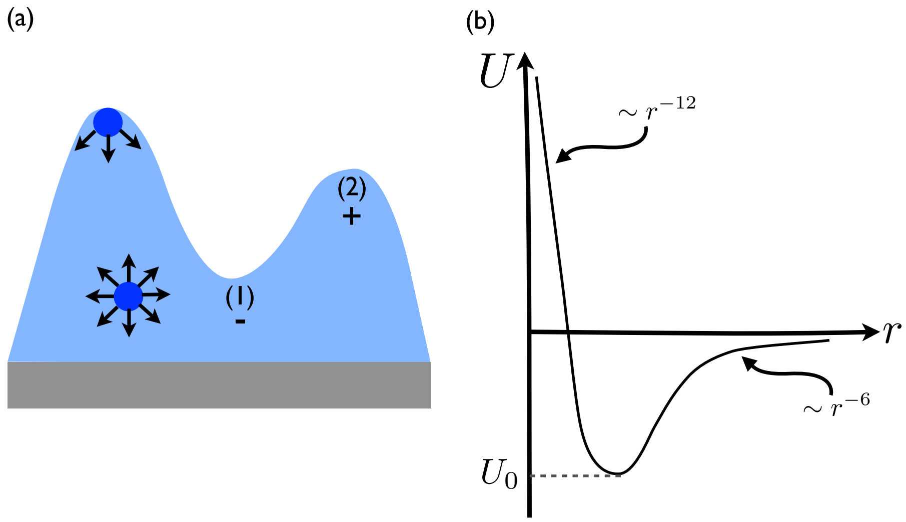

Figure 1.8: (a) A molecule in the bulk of a liquid experiences cohesive interactions with each of its neighbours. Since a molecule at the interface is missing some of its cohesive interactions, there is an energetic cost associated with having a molecule at the surface. This is the phenomenon of surface tension. Gradients in curvature at the interface result in pressure gradients caused by surface tension. The Laplace pressure is lower at point (1) compared to point (2) as indicated by the signs. (b) The Leonard-Jones potential describes the interaction energy between two molecules. At short ranges there is a Coulombic repulsion and at long ranges there is an attractive van der Waals interaction. Molecules tend to be separated by a distance which corresponds to the minimum in the potential.

commonly defined as the energy required to increase the surface area of the liquid by one unit [1]. For a system with volume V, composed of N molecules at temperature T we write

$$\gamma = \left(\frac{\partial F}{\partial A}\right)_{T,V,N} \tag{1.28}$$

which has dimensions of energy per area and is typically expressed in units of $\mathrm{mJ/m^2}$.

We can also consider surface tension from a mechanical point of view. A molecule in the bulk of the liquid feels an attractive force from each of its nearest neighbours. The molecule is pulled equally in every direction and experiences no net force. However, a molecule at a curved surface is missing some of its nearest neighbours and only feels cohesive forces on the sides of the molecule which neighbour the liquid. This imbalance results in a net force pulling the molecule at the surface inward toward the bulk of the liquid [2].

The manifestation of surface tension in everyday life is remarkable. Insects such as water striders rely on surface tension to walk on water. The insect's feet deform the liquid interface causing an increase in its surface area. The water resists this change, behaving like a thin elastic sheet and supporting the weight of the insect. The same effect is seen in common laboratory demos when an object denser than water such as a paper clip floats after being carefully placed onto the liquid interface. Adding a drop of surfactant to the liquid, such as soap lowers the surface tension and the paper clip immediately sinks to the bottom of the dish.

Now, returning to the curved interface depicted in Fig. 1.8, we consider the pressure difference between the inside and outside of the surface. To understand this pressure difference, known as Laplace pressure, we simplify the problem and consider a spherical drop of radius R. Following the discussion of Laplace pressure presented in [1], let us imagine a drop of oil suspended in water. Suppose we increase the radius of the drop by dR. The work done by capillary forces (surface tension) and pressure is

$$\delta W = -P_o dV_o - P_w dV_w + \gamma_{ow} dA \tag{1.29}$$

where the subscripts o and w refer to oil and water respectively: dV_o and dV_w are the changes in volume, dA is the change in surface area of the drop, P_o and P_w are the pressures in the liquids and γ_{ow} is the interfacial tension. For a spherical drop we have $dV_o = 4\pi R^2 dR$ and $dA = 8\pi R dR$. Conservation of volume requires $dV_o = -dV_w$ giving

$$\delta W = -(P_o - P_w)(4\pi R^2 dR) + \gamma_{ow} 8\pi R dR. \tag{1.30}$$

At equilibrium $\delta W = 0$ and we have

---

[2] It should be emphasized that this is an overly simplistic treatment of the problem. In particular, the net force acting on the molecule is only inward in the case of a curved surface. Here we have only considered the attractive forces between molecules, but a proper description must also take into account repulsive forces arising from pressure. For a perfectly flat surface, a molecule feels a force parallel to the interface, a result which is surprisingly non-trivial and often misunderstood. See [27] for example.

$$\Delta P = P_o - P_w = \frac{2\gamma_{ow}}{R}. \tag{1.31}$$

Of course, Eq. 1.31 describes the pressure jump across the surface of a drop for any two fluids if we simply replace γ_{ow} by the appropriate interfacial tension. Eq. 1.31 explains why small oil drops merge into larger ones when oil and water are mixed. Smaller drops have a higher Laplace pressure and are therefore less stable compared to larger drops. The same effect is observed when two soap bubbles, one large and one small, join allowing air to flow between them. The small bubble has a higher pressure than the larger one, resulting in a pressure gradient which drives flow. Fluids flow from areas of high pressure toward lower pressure regions, so the small bubble empties into the larger one.

The above expression for Laplace pressure can also be generalized to any curved surface,

$$\Delta P = \gamma\kappa \tag{1.32}$$

where the curvature of the surface, κ, is defined in terms of the radii of curvature, R_1 and R_2 as $\kappa = 1/R_1 + 1/R_2$. Quite simply, Eq. 1.32 tells us that curvature at an interface results in a pressure caused by surface tension. One consequence of this fact is that for an interface with non-constant curvature, there exists a pressure gradient along the interface of the fluid. In general, pressure gradients result in flow.

Consider the interface shown in Fig. 1.8(a). Such a surface geometry is only dependent on the x coordinate so the interface can be described by a function $h = h(x)$. In this case the curvature of the interface can be written as [28]

$$\kappa = \frac{-\partial_x^2 h}{\left[1 + (\partial_x h)^2\right]^{3/2}}. \tag{1.33}$$

Assuming the height gradients are small (the so-called lubrication approximation which will be discussed in detail in Section 1.4.1), $[1 + (\partial_x h)^2] \approx 1$ and Eq. 1.33 simplifies to $\kappa \approx -\partial_x^2 h$. Therefore the local Laplace pressure in the fluid is given by

$$P(x) \approx -\gamma\partial_x^2 h. \tag{1.34}$$

Therefore according to Eq. 1.34, regions of the interface which are concave up have a lower pressure than those which are concave down. This is shown in Fig. 1.8, where the signs at points (1) and and (2) indicate the the pressure is lower at point (1) compared to point (2). Since fluid flows from regions of high pressure toward regions of low pressure, in this case, fluid will flow from (1) to (2) to level the interface and minimize the surface area of the system.

The physics of Papers 2 and 3 can be summarized in the simplest possible terms by stating that Laplace pressure gradients which arise because of surface tension drive a fluid with a non-equilibrium surface geometry to level.

1.4.1 Capillary driven flows and the thin film equation

Papers 2 and 3 make extensive use of the thin film equation (TFE) to describe surface tension driven flows in thin polymer films. In this section we develop the thin film equation, starting from the Navier-Stokes equation and applying the lubrication approximation. The Navier Stokes equation which is a statement of Newton's second law per unit volume of fluid reads

$$\rho\left(\frac{\partial \mathbf{v}}{\partial t}+\mathbf{v}\cdot\nabla\mathbf{v}\right)=-\nabla P+\eta\nabla^2\mathbf{v}+\mathbf{f} \tag{1.35}$$

where $\mathbf{v}=(v_x,v_y,v_z)$ is the velocity field and $\mathbf{f}$ are body forces (such as gravity) per unit volume acting on the fluid. The left side of Eq. 1.35 is the inertial term and describes the acceleration while the right hand side is the summation of the forces acting on a unit of fluid: pressure, viscous forces and body forces. We also introduce the incompressibility condition

$$\nabla\cdot\mathbf{v}=0. \tag{1.36}$$

In general, Navier-Stokes equation represents a significant mathematical challenge due to the fact that it is system of coupled, second order non-linear equations. To date the equation remain unsolved. However in certain limits the problem becomes tractable. Our first simplification comes from considering the Reynolds number, Re, which evaluates the relative importance of inertial to viscous forces in the system and the capillary length, l_c which is length scale beyond which gravity must be considered:

$$\mathrm{Re} = \frac{h_0 \rho v}{\eta} \tag{1.37}$$

$$l_c = \sqrt{\frac{\gamma}{\rho g}} \tag{1.38}$$

where h_0 is the typical length scale in the system and v is a characteristic flow velocity. The experiments presented in Papers 2 and 3 are performed using polymer films with a thickness $h_0 \sim 100$ nm which have viscosity $\eta \sim 1$ MPa s and surface tension $\gamma \sim 30$ mN/m. The flow velocity is characterized by the capillary velocity, $v_c = \gamma/\eta$. These parameters give $\mathrm{Re} \ll 1$ and $l_c \sim 1$ mm $\gg h_0$. Therefore, gravity is negligible and since the Reynolds number is small, we assume viscous forces dominate and ignore the inertial terms of Eq. 1.35. In these conditions, the Navier-Stokes equation reduces to

$$-\nabla P + \eta \nabla^2 \mathbf{v} = 0 \tag{1.39}$$

which is known as Stokes equation. Expanding Eq. 1.39 we have the following system of partial differential equations:

$$-\frac{\partial P}{\partial x} + \eta \left(\frac{\partial^2 v_x}{\partial x^2} + \frac{\partial^2 v_x}{\partial y^2} + \frac{\partial^2 v_x}{\partial z^2} \right) = 0 \tag{1.40a}$$

$$-\frac{\partial P}{\partial y} + \eta \left(\frac{\partial^2 v_y}{\partial x^2} + \frac{\partial^2 v_y}{\partial y^2} + \frac{\partial^2 v_y}{\partial z^2} \right) = 0 \tag{1.40b}$$

$$-\frac{\partial P}{\partial z} + \eta \left(\frac{\partial^2 v_z}{\partial x^2} + \frac{\partial^2 v_z}{\partial y^2} + \frac{\partial^2 v_z}{\partial z^2} \right) = 0. \tag{1.40c}$$

Papers 2 and 3 study films which are invariant in the y-direction so $v_y = 0$ and all ∂_y terms vanish leaving a two dimensional problem. We now apply the lubrication approximation which assumes $l \gg h$ where l is the typical length scale in the x-direction (parallel to the interface) and h is the typical length scale in the z-direction (perpendicular to the interface). The two main consequences of the lubrication approximation are: 1) flow in the z-direction is negligible so $v_z \approx 0$ and 2) flow gradients are only significant in z, $\partial_z v_x \gg \partial_x v_x$. Therefore, Stokes equations simplify to

$$-\frac{\partial P}{\partial x} + \eta \frac{\partial^2 v}{\partial z^2} = 0 \tag{1.41a}$$

$$\frac{\partial P}{\partial z} = 0. \tag{1.41b}$$

where we have defined $v \equiv v_x(z)$ for simplicity. For boundary conditions, we assume no slip at the solid/liquid interface so $v(0) = 0$, and no shear at the liquid/air interface, $\partial_z v|_{z=h} = 0$ where h is the film thickness. As discussed in Section 1.4, pressure gradients are attributed to Laplace pressure gradients in the x-direction which arise due to non-constant curvature at the liquid/air interface. In particular, $P = P(x)$. Therefore integrating Eq. 1.41a with respect to z gives

$$\frac{\partial v}{\partial z} = \frac{1}{\eta}\left(\frac{\partial P}{\partial x} z + C_1\right) \tag{1.42}$$

where C_1 is a constant of integration. We integrate again to obtain

$$v(z) = \frac{1}{\eta}\left(\frac{\partial P}{\partial x}\frac{z^2}{2} + C_1 z + C_2\right) \tag{1.43}$$

where another constant of integration, C_2 has been introduced. Applying the no-slip and no-shear boundary conditions we arrive at

$$v(z) = \frac{1}{2\eta}\frac{\partial P}{\partial x}\left(z^2 - 2zh\right) \tag{1.44}$$

which is a parabolic flow profile commonly referred to as Poiseuille flow.

We now the define the flow rate Q as the amount of fluid flowing into a cross section per unit time:

$$Q = \int_0^h v(z)\mathrm{d}z = -\frac{1}{3\eta}\frac{\partial P}{\partial x}h^3. \tag{1.45}$$

The incompressibility condition, Eq. 1.36 requires that volume is conserved so we must have $\partial_x Q = -\partial_t h$. Therefore using Eq. 1.45, conservation of volume implies

$$\frac{\partial h}{\partial t} - \frac{1}{3\eta}\frac{\partial}{\partial x}\left(h^3 \frac{\partial P}{\partial x}\right) = 0. \tag{1.46}$$

Finally, applying Eq. 1.34 which says that within the lubrication approximation, the Laplace pressure is given by $P(x) \approx -\gamma\partial_x^2 h$ we arrive at the thin film equation

$$\frac{\partial h}{\partial t} + \frac{\gamma}{3\eta}\frac{\partial}{\partial x}\left(h^3\frac{\partial^3 h}{\partial x^3}\right) = 0. \tag{1.47}$$

which describes the levelling of a non-equilibrium interface where the flow is driven by surface tension and mediated by viscosity.

From an analytical perspective, one important feature of Eq. 1.47 is that it permits self-similar solutions of the form $h(x,t) = h(x/t^{1/4})$, a fact which is exploited in Papers 2 and 3. In these works, TFE is numerically solved by non-dimensionalizing the equation through the change of variables, $H = h/h_0$, $X = x/x_0$ and $T = \frac{\gamma t}{3\eta h_0}$. This allows us to write a dimensionless version of the thin film equation

$$\partial_T H + \partial_X\left(H^3\partial_X^3 H\right) = 0 \tag{1.48}$$

which has self-similar solutions $F(U) = H(X,T)$ where $U = X/T^{1/4}$. Further details on the analytical treatment of the TFE used in Papers 2 and 3 can be found in [29–31] for example. These works are the result of a fruitful collaboration with Prof. Elie Raphael's theory group (ESPCI, Paris) while the experiments were carried out at McMaster University. Details of the experiments are described in [11, 12, 32].

1.4.2 Marangoni effect

We now turn our attention to the Marangoni effect, which is the flow of liquid along an interface due to the presence of a surface tension gradient. The most common example of the Marangoni effect is the phenomenon known as 'tears of wine'. Imagine slowly swirling a glass of wine so that the sides of the glass are coated in a thin layer of wine. The surface area of the fluid coating the glass is high so evaporation happens quickly. Both water and alcohol evaporate but alcohol is more volatile than water, which results in a liquid film with a higher concentration of water compared to the wine in the glass. Water has a higher surface tension than alcohol and therefore the fluid coating the glass has a higher surface tension than the wine below. The gradient in surface tension between the wine in the glass and the fluid coating the glass induces flow. Wine flows up the glass from the region of low surface tension, toward the area

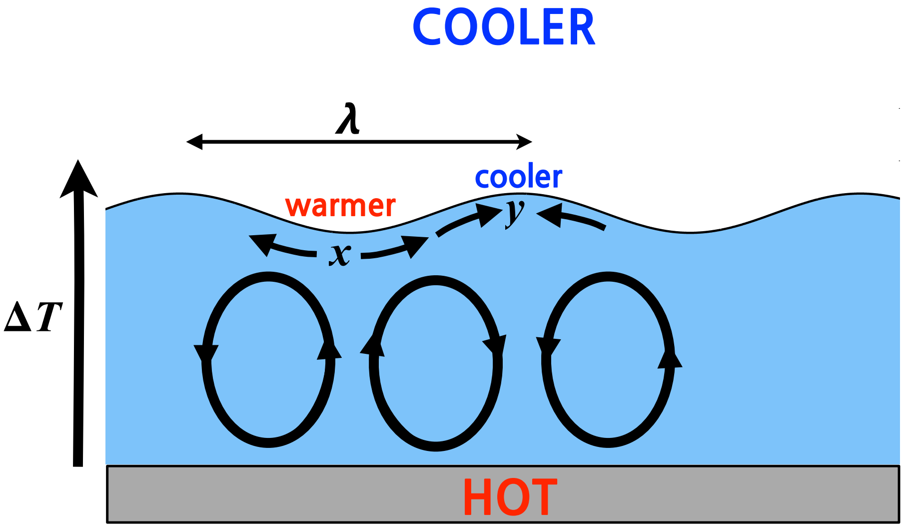

Figure 1.9: Schematic of Marangoni driven instabilities in a thin liquid film which is heated from below. If there is a perturbation to the free surface, the region of fluid which is closer to the heat source is warmer than the fluid in the surrounding regions. Surface tension decreases with temperature so the surface tension is lower at x compared to y. This surface tension gradient induces flow. Under certain conditions this effect leads to convection cells in the fluid. The wavelength of these cells scales with the depth of the fluid: $\lambda \sim h$.

of high surface tension. As the wine flows up the glass it forms drops which fall back down the glass under their own weight.

Marangoni driven instabilities can be observed when a thin liquid film is heated from below to induce a temperature gradient ΔT across the film [28,33,34]. If there is any perturbation to the free surface, the fluid which is closer to the heated substrate will be hotter than the fluid in the surrounding regions. Since surface tension decreases with temperature, the regions of interface which are closer to the heat source have a lower surface tension compared to those farther from the substrate. This is shown schematically in Fig. 1.9, where the surface tension at point x is lower than at y. The gradient in surface tension drives flow. As shown in Fig. 1.9, fluid flows away from the areas of low surface tension (x) toward areas of high surface tension (y). As liquid is pulled away from the low surface tension regions, fluid from below must come in to take its place. Normally, the surface tension driven flow is mediated by viscosity and thermal diffusion, and the interface simply flattens. However, under certain conditions, the process described above is amplified establishing convection cells in the fluid. The ratio between surface forces and dissipation due to thermal diffusivity and viscosity is expressed by the Marangoni number

$$M = -\frac{d\gamma}{dT}\frac{h\Delta T}{\eta\alpha} \tag{1.49}$$

where α is the thermal diffusivity. It has been shown that for a there is some critical Marangoni number, M_c, above which instabilities occur [28, 36]. For $M > M_c$ surface tension drives the formation of convection cells. It has been established that the wavelength of these cells scales with the depth of the fluid, $\lambda \sim h$ [28, 35–38]. Marangoni driven convection is fundamental to the work presented in Paper 1.

At the most basic level, the Marangoni effect is a surface tension driven process. In the example of tears of wine discussed above, surface tension gradients arise because of concentration gradients in the liquid. For the case of a heated liquid film, surface tension gradients which occur because of temperature gradients may lead to the formation of convection cells. In either case, a surface tension gradient results in flow.

1.5 Thin films

Up until this point, we have primarily discussed the physics of polymers in bulk systems. All of the papers presented in this work involve thin polymer films. Polymers which have been confined to thin films often exhibit remarkably different properties from those in the bulk state [39–41]. Many of the surprising phenomena observed in thin polymer films stem from two major differences between thin films and bulk systems. Firstly, the surface-to-volume ratio is dramatically greater in a thin film compared to the bulk. Secondly, in thin films polymer molecules are confined to a small space and thus the chains explore a smaller volume than in the bulk. The idea of confinement is explored in Paper 4, where polymers are confined to films thinner than the equilibrium size of the molecule which results in a non-equilibirum entanglement network. By probing the temporal evolution of the entanglement network we are able to learn about chain conformations under confinement.

1.5.1 Spincoating

In addition to the effects discussed above, the process of film preparation itself may lead to non-equilibrium effects that are not observed in bulk systems. Thin polymer films typically inherit their structure through the process of spin coating. A small amount of polymer solution is dropped onto a substrate which is then rapidly rotated. Initially, most of the solvent is ejected. The remaining solvent rapidly evaporates typically leaving behind a glassy polymer film with a thickness on the order of nanometres to microns.

It has been well established that the violent spincoating process leaves polymer chains out of their equilibrium conformation [41–47]. This effect is often attributed to the rapid evaporation of solvent during spinning but the precise details of both the non-equilibirum chain conformations and the factors affecting their formation remain unknown. Annealing a spincast film above T_g allows the mobile chains to relax toward their equilibrium state. It has been shown that for a sufficiently thick, well annealed film, the chain conformations are the same as those in the bulk [6]. One question that has been frequently addressed in recent literature is - how long does it take for a spin-cast polymer film to recover bulk-like behaviour?

Recent work by Barbero and Steiner [46] and Thomas *et al.* [41] has probed the effect of annealing on the viscosity of a spincast film. In particular, Thomas *et al.* characterize the annealing time required for a spincast film to recover bulk rheology and find that the process takes several orders of magnitude longer than the reptation time [41]. Work by Raegan *et al.* has shown that the behaviour of spin cast films is strongly dependent on conditions of film preparation [43]. Furthermore, the authors find that the recovery of bulk-like behaviour for high M_w spincast films requires months of annealing above T_g, a conclusion similar to the one presented in [41]. These results are in conflict with the idea that the longest relaxation time in a polymer melt is τ_R. In Paper 4 we address the issue of non-equlibirum behaviour in spin-cast films by directly probing the temporal evolution of the entanglement network as a function of annealing time. In contrast to the works discussed above, we find that the entanglement network relaxes on a timescale on the order of τ_R.

Spincoating is also used industrially to apply coatings and has applications to a diverse range of technologies including solar cell production, the development of

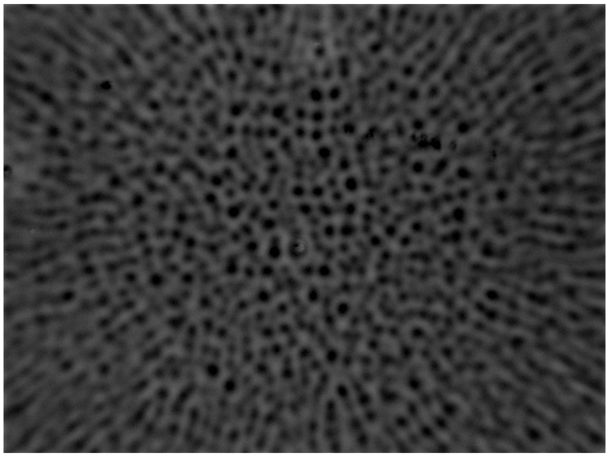

Figure 1.10: Optical image of a non-uniform spin-cast polymer film. This image (1400 μm across) shows a polystyrene film spincast from toluene. The centre of the image corresponds to the axis of rotation of the spincoater.

polymer based semiconductors and biomedical engineering. In most circumstances spincoating produces high quality uniform films, however under certain conditions spincast films exhibit non-uniform surface topographies such as the one shown in Fig. 1.10. Since the spincoating process is so prevalent, much effort has gone into characterizing the factors giving rise to such topographies [38,48–54]. Despite this, the formation of non-unifom spincast films remains a practical problem in both research laboratories and industrial settings.

Some authors have proposed that spincoating from solvent blends or in an environment saturated with solvent may suppress the formation of non-uniform films [50–52, 55]. Although these techniques are routinely tried in research laboratories, they are often cumbersome and their success depends on the particular combination of polymer/solvent in use. Furthermore, a thorough description of the physics governing the formation of non-uniform spincast films remains elusive.

In Paper 1 we address these issues by presenting a simple technique to avoid the formation of non-uniform spincast films. Furthermore, we are able to understand the physics governing the system in terms of the Marangoni effect, which was outlined in Section 1.4.2.

Chapter 2

Experimental Details

The full details of each experiment are clearly outlined in the papers. Here we give a brief overview of the experimental techniques, particularly focusing on details not included in the papers which may be useful for those attempting similar sample preparation. All sample preparation begins by spincoating thin polymer films onto either Si substrates or freshly cleaved mica. Typical film thicknesses range from $50 < h < 600$ nm. Almost all the experiments presented in the papers use polystyrene (PS) with molecular weights ranging from $8.8 < M_w < 1140$ kg/mol. In Papers 2 and 3 we follow the spincoating procedure outlined in Section 1.5.1. However, in Papers 1 and 4 we use a specially designed spincoater setup which allows us to easily and accurately adjust the spincoating temperature. The details of this setup are outlined in Section 2.1. In either case, to obtain high quality films we keep the spin speed (ω) in the range $2000 < \omega < 5000$ rpm. We note that for most of the work presented here, the cleaning of substrates prior to spincoating was was kept to a minimum. In particular, it was found that when Si is properly cleaved most additional treatments such as solvent cleaning offer little to no improvement and in many cases reduce the cleanliness of the substrate. The only standard treatment was to spray both the Si and mica substrates with a jet of nitrogen immediately after cleaving to remove any large pieces of dust which may result from the cleaving process. In certain cases, the Si wafers were also exposed to air plasma and rinsed with water, methanol and toluene prior to spincoating.

The second stage of sample preparation which was common to the papers presented in this thesis is an initial annealing (pre-annealing) of the freshly spincast films. This removes any residual solvent left in the film after spincoating and relaxes stresses in the film induced by spincoating. In most cases, the pre-annealing was done in a home built vacuum oven and the films were always annealed for at least $5\tau_R$. It was shown in Paper 4 that as-cast films equilibrate on a timescale on the order of τ_R so our pre-annealing procedure is more than sufficient to ensure the chains have relaxed to their equilibrium state [1]. Annealing procedures were particularly important for Paper 4 since reptation times, which were used extensively in the analysis, depend exponentially on temperature. Therefore, our experiments were sensitive to temperature gradients of only a few degrees. To combat this problem a specially designed annealing setup for which the temperature of the sample is known to within 1° C was used. A detailed description of this annealing setup can be found in [32]. These annealing procedures were originally implemented in the experiments presented in Paper 4 but were also applied to all other experiments presented in this thesis.

We will now proceed to describe the sample preparation techniques particular to each project.

2.1 Spincoating

Here, we explain the specially designed spincoating setup used in Paper 1. A schematic of the setup is shown in Fig. 2.1. The substrate is placed onto a large aluminum disk which we refer to as the spincoater 'chuck'. The spincoating temperature is controlled by changing the temperature of the chuck. First, to ensure good heat transfer between the chuck and substrate, the substrate is forced into contact with the chuck using four small screws. The screws make contact with the substrate only at its very edges so as to not impede the spincoating process. In addition, we use 20×20 mm Si wafers (rather than the 10×10 mm wafers which are typically used for the type of experiments in this thesis) to further ensure that the screws interfere with a minimal

---

[1] In Paper 4 it was shown that spin-cast films inherit a non-equilibrium entanglement network. Through crazing measurements it was found that the entanglement network relaxes on a timescale on the order of one bulk reptation. Therefore, annealing for at least $5\tau_R$ is sufficient to ensure an equilibrium entanglement network within the resolution of a crazing measurement.

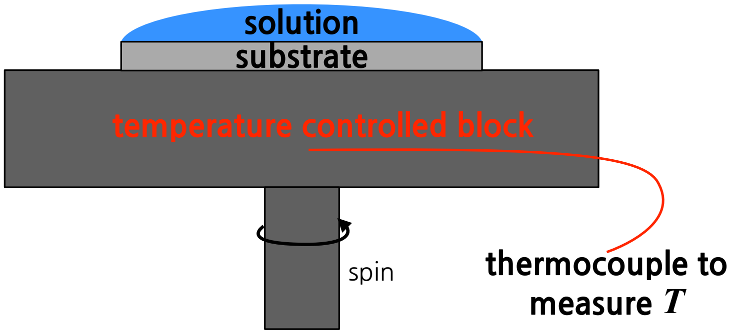

Figure 2.1: Schematic of the spincoating setup used in Paper 1. The substrate placed onto a temperature controlled aluminum block which we refer to as the ‘chuck’ and held in place with screws to ensure good thermal contact. A thermocouple embedded into the block is used to monitor its temperature. The polymer solution is deposited onto the substrate. The entire system is rotated and the temperature of the chuck is recorded immediately prior to spinning. Note that this schematic is not drawn to scale. The size of the substrate/solution is negligible compared to the chuck.

area of the substrate and do not affect spincoating.

The chuck/substrate is then either placed onto a heater or in a cooled environment. A thermocouple is embedded into the chuck to monitor its temperature. We emphasize that since the thermocouple is deeply embedded into the chuck and sits directly below the substrate it provides an accurate measure of the temperature of the Si wafer. Once the chuck reaches the desired temperature, it is transferred to a commercial spincoating apparatus (Headway Research Inc., Model PWM32). We then deposit solution onto the substrate. Next, the temperature of the chuck is recorded, the thermocouple is removed from the chuck and we begin rotating the chuck/substrate. It is important to note that these steps are done as rapidly as possible so the temperature we measure is an accurate measure of the temperature at the start of spinning. Furthermore, since the substrate/solution is in good thermal contact with the chuck and the thermal mass of the substrate/solution is negligible compared to the chuck, we make the assumption that the temperature of the chuck is that of the solution at the start of spinning. This assumption was validated by placing a second thermocouple into the solution immediately prior to spinning. It was found that the temperature of the solution and chuck were within 1° C which is within experimental error. Once this was confirmed, we proceeded to record only the temperature of the chuck since a setup involving multiple thermocouples is cumbersome.

Spincoating at different temperatures was also done in Paper 1. In this work an earlier version of the spincoating setup described above and shown in Fig. 2.1 was used. In this version of the setup, the thermocouple was simply placed onto the chuck and held in place using either electrical tape or a small weight. Also, this version of the setup did not involve screwing the substrate into contact with the chuck. Nevertheless, the thermal contact between the substrate and chuck was good and the thermocouple provided an accurate measure of the temperature of the chuck. The same test described above where the temperature of the solution was measured and compared to the temperature of the chuck was performed. It was still found that the temperature of the solution and chuck were the same within experimental error.

Finally, we note that in Paper 1 it was found that spincoating at temperatures below room temperature can help suppress the formation of non-uniform films. In Paper 1 the cooling is achieved by placing the chuck setup described above into a cooled environment. However, we emphasize that the same effect may be achieved using any standard spincoating setup by simply placing the solution in a fridge for several minutes prior to spinning.

2.2 Capillary levelling

Here we describe the sample preparation techniques used in the capillary levelling experiments presented in Papers 2 and 3. First we describe 'step levelling' which is an experimental technique used to measure rheological properties in thin polymer films. Step levelling was developed in [11,12] and the sample preparation procedures used in Papers 1 and 2 are based on the techniques presented in [11,12]. Furthermore, in Papers 2 and 3 we use step levelling to measure capillary velocities.

Briefly, as shown in Fig. 2.2 samples are prepared with an initial height profile that is accurately described as a Heaviside function. When the sample is annealed above T_g, capillary forces drive the step to level toward the equilibrium state of a flat film. By measuring the temporal evolution of the film height profile we can extract the capillary velocity, γ/η. The full details of both the sample preparation and analysis

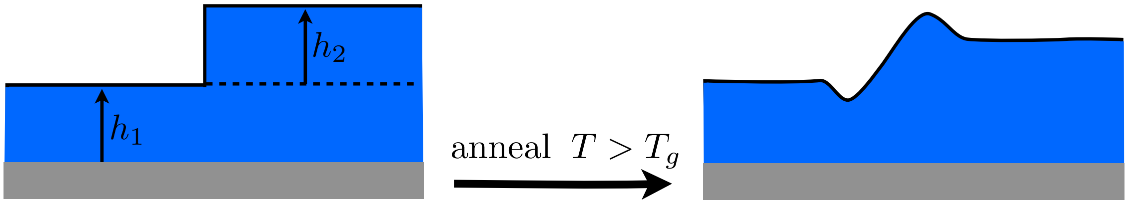

Figure 2.2: Schematic of a step levelling experiment. Samples are prepared with a geometry that is well described by a Heaviside step function. As the sample is annealed at $T > T_g$, capillary forces drives the step to level. By following the time evolution of the film height profile, the capillary velocity γ/η can be extracted as outline in [11,12]

can be found in [11,12,29,30]. Further experimental details can be found in [32].

2.2.1 Steps

Here we outline the procedure for preparing a polymer film with a stepped bilayer geometry. We begin by spincoating a film with thickness h_1 on silicon and a film of thickness h_2 onto mica. We now consider two cases: low M_w films and high M_w films.

For the case of low molecular weight films (M_w near or below M_e), the preparation is relatively straightforward. The film of thickness h_2 is floated off the mica substrate onto the surface of a clean water bath (18.2 Mcm, Pall, Cascada, LS). Since $M_w \leq M_e$, these films readily fracture into many pieces when they are floated onto the water surface. These pieces of film typically have straight edges on the order of $100 - 1000$ μm in length. Next, we pick up one of these pieces using the previously prepared film of thickness h_1 on Si. The straight edges result in a film height profile that is well approximated as a Heaviside function over length scales long enough such that we can consider the height profile invariant in the direction orthogonal to the step (a condition necessary to apply the lubrication approximation outlined in Section 1.4.1).

For the case of high M_w films, the process is significantly more involved. When a well entangled film ($M_w > M_e$) is floated onto the surface of a water bath it does not fracture into pieces with clean edges since the entanglements in the film greatly increase its strength. To circumvent this problem, we use the following procedure.

First, using a scalpel we scribe the film of thickness h_2 on mica into a grid of 10 mm $\times$ 10 mm squares. When scribing it is important to apply as little pressure as possible to avoid the formation of mica dust which may contaminate the film. These 10 mm $\times$ 10 mm sections are then floated onto the surface of a clean water bath. Using a bare, clean Si substrate, these pieces of film (with thickness h_2) are picked up. Prior to this floating step, it can be useful to plasma clean the Si substrate for ≈ 30 seconds. Doing so slightly changes the equilibrium contact angle between PS and Si which makes the floating easier. To minimize the number of wrinkles and folds we pick up the films as follows. Using self-closing tweezers, the plasma cleaned Si substrates are partially submerged in the water bath and held so that the angle between the water surface and submerged wafer is between $30 - 45°$. Using another pair of tweezers one of the 10 mm $\times$ 10 mm sections of film floating on the water surface is gently nudged toward the Si until it makes contact. The Si is then slowly and gently pulled out of the water, allowing the water between the film and wafer to gradually evaporate as the Si is removed.

Once the film of thickness h_2 has been successfully floated onto the Si wafer it is left to dry for ~ 10 min (this drying stage is crucial to avoid the formation of crazes during the cracking procedure which will be explained below). Next, using a diamond scribe, a small 1 mm notch is scribed onto the Si along the crystal axis, avoiding the film which has been floated onto the wafer if possible. Using the diamond scribe, pressure is applied to the notch until the Si breaks along the crystal axis. Along this crack, the PS film will have a clean, straight edge.

Next, the cracked Si wafers are slowly submerged back into the water allowing the PS film with thickness h_2 which now has a clean edge to float off. Finally, these pieces of film with thickness h_2 are picked up using the previously prepared film of thickness h_1 on Si to create a stepped bilayer film. We note that during the final floating step, it is best to float such that the clean edge is the last to leave the water surface.

For high M_w the cracking process often results in the formation of crazes along the split edge. Regions of the edge which are crazed cannot be used for measurement. To check for crazes, we examine the film using an optical microscope (dark field, 50×). In many cases the entire edge will be crazed and the sample preparation will need to be attempted again. For very high M_w films ($M_w > 200$ kg/mol) the formation of crazes makes sample preparation very challenging and only 1 in every 6-10 cracked films will have clean, craze free edges. In these circumstances, it has been found that the formation of crazes can be suppressed by cracking the films in liquid nitrogen. In this case, the Si wafer is submerged in liquid nitrogen and cracked using two pairs of robust self closing tweezers. The one drawback of this technique is that there may be Si dust on the film as a result of the more violent cracking process.

Once a sample has been prepared which has a step that appears clean under optical microscopy, the spot is measured using atomic force microscopy (AFM) to ensure the initial film height profile is well described as a Heaviside function. Provided this is true, the sample is annealed on a Linkam hotstage using a heating rate of 90° C/min. As the sample is annealed above T_g capillary forces drive the step to level. After various times t, the sample is rapidly quenched to room temperature and the film height profile is measured using AFM. Following the series of AFM measurements, a scalpel is used to gently scratch the film and expose the Si substrate (very little pressure is required to scratch the film). The bottom film thickness, h_1 is measured using AFM by scanning a spot on the sample along the scratch where the substrate and film can be simultaneously imaged.

2.2.2 Trenches

In Paper 3 we study the capillary driven levelling of films with a rectangular trench geometry. A schematic of this geometry is shown in Fig. 1 of Paper 3. The procedure used to prepare films with this geometry is similar to the technique used to prepare low M_w stepped films. We begin by spincoating films of thickness h_1 onto Si and thickness h_2 onto mica. The film on mica is floated onto the surface of an ultra pure water bath. In Paper 3 we work exclusively with low M_w films, so these films break into pieces as described above. In particular, the film often contains 'float gaps' where the film has broken into two pieces with long straight edges that are separated by only a few microns. By picking up a piece of film with a float gap using the film of thickness h_1 on Si we create sample with a rectangular trench geometry. The depth of the trench (distance from the bottom of the trench to the total film thickness, $h_1 + h_2$) is h_2. Since the float gaps are long and straight, the width of the trench is invariant the lubrication approximation applies.

2.2.3 Surface perturbations

In Paper 2 we study the capillary driven levelling of polymer films with small surface perturbations. Again, we begin by spincoating a film of thickness h_{Si} onto silicon and a film of thickness h_{Mi} onto mica. The film on mica is scored into 10 mm × 10 mm sections using a scalpel and these sections are floated onto the surface of an ultra pure water bath. These sections are then picked up using the previously prepared films on Si with thickness h_{Si}. During the transfer we intentionally float 'poorly' to create wrinkles and folds in the film, which serve as random surface perturbations. In contrast to the conventional floating technique where the film on the water surface is approached from below with a partially submerged substrate, here samples were prepared by approaching from above - the film of thickness h_{Si} was 'dunked' into the water film side first. Of course this 'poor' floating technique greatly increases the number of folds and wrinkles resulting from the transfer, which is beneficial for this work. Surface perturbations can also be prepared by depositing a polymer fibre onto a film or using laser lithography for example. However, if the ultimate goal is simply to create random perturbations, floating is easiest.

In Paper 2 we work exclusively with low M_w PS so when the film of thickness h_{Mi} is floated onto the water surface, it breaks into many pieces. When the film of thickness h_{Si} is dunked into the water, we attempt to transfer several of these pieces onto the film. Since these pieces have long straight edges, in addition to creating random surface perturbations, portions of the sample will also have a stepped bilayer geometry. Using optical microscopy we examine the sample to see if any of the steps are clean, wrinkle free and suitable for measurement. If no such step exists, small pieces of film with thickness h_{Mi} are floated onto clean regions of the sample until a clean, straight, wrinkle free step is prepared. In practice, a perfect step is usually created during the first transfer and subsequent floating is not necessary. We emphasize that by preparing samples in this manner, each sample has both surface perturbations and a stepped bilayer. We use the stepped bilayer to measure the viscosity *in situ*: while tracking the evolution of the surface perturbation, we also record measurements of the stepped bilayer on the same sample from which we extract the capillary velocity,

γ/η. Using this technique, we reduce measurement error associated with small sample to sample variation.

After the sample is prepared it is annealed for 1 min at 130° C. This short anneal removes any residual water from the system and ensures the floated films are in good contact with the substrate film. We note that although there is some flow during this short anneal above T_g, the evolution of the geometry is negligible because subsequent annealing is performed for longer times at a higher temperature. More importantly, the $t = 0$ state is defined after this initial annealing step.

Finally, the sample is examined under an optical microscope and a perturbation which has a height profile that is invariant in one direction is chosen for measurement (i.e. the height of the perturbation can be taken as $h = h(x, t)$ which allows us to apply the lubrication approximation). Initial height profiles of both the perturbation and step were recorded using AFM. Samples were then annealed on a Linkam hotstage at 140° C using a heating rate of 90° C/min. Following various times t, the sample is quenched to room temperature and height profiles of both the surface perturbation and stepped bilayer are measured with AFM.

2.3 Crazing

Here an outline of the sample preparation techniques used in Paper 4 is presented. In this work two types of samples were prepared: monolayers (single PS film) and bilayers (two PS films stacked on top of each other). For the case of monolayers, films of thickness $h \approx 100$ nm were spincast onto mica. These films were annealed for various times t in a home built vacuum oven (pressure $\sim 10^{-5}$ mbar) at 130° C. As detailed at the start of Chapter 2, the temperature of the sample is known to within 1° C which is crucial for accurate crazing measurements. After annealing, a scalpel was used to gently score the film into 10 mm × 10 mm squares which were floated off the mica onto the surface of an ultra pure water bath. These sections of film were picked up across a fixed 1.5 mm gap between two aluminum blocks. Before films were floated onto the blocks, the blocks were cleaned using acetone and Kimwipes. The blocks were also regularly polished using very fine sandpaper and then sonicated in toluene to remove any aluminum dust left behind after polishing.

After floating, the films were allowed to dry for at least 30 minutes. Next, the aluminum blocks were attached to a translation stage and the gap between the blocks was unfixed, allowing the two blocks to be pulled apart from one another. The blocks were then slowly pulled apart until crazes were visible under an optical microscope. A constant strain rate of $\epsilon = 2 \times 10^{-3}$ s was used and samples were strained to approximately $\epsilon = 0.1$. We emphasize that crazing was performed at room temperature under ambient conditions. We also note that if the films are not left to dry for a sufficient amount of time, the films may not readily craze when strained. Finally, we stress that the edges of the aluminum blocks must be sharp and clean to avoid slippage of the film at the blocks and to ensure crazes do not nucleate from dirt pieces on the aluminum.

Once the PS films were crazed, the gap between the blocks was fixed and the freestanding film was transferred to a clean Si substrate, allowing surface forces to pull the crazed film into contact with the substrate. A scalpel was used to gently scratch the film and expose the Si substrate. By measuring an appropriate spot along a scratch, the height of a craze, h_c and the height of the film, h can be simultaneously determined.

For the case of bilayer films the sample preparation process is as follows. First films of thickness $h_m \approx 50$ nm were spincast onto mica. Films were annealed in the home built vacuum oven for 48 hours at 150° C. This pre-annealing step, which was not part of the monolayer sample preparation ensures that the spincast films have fully a equilibrated entanglement network. After annealing, a film of thickness h_m was floated onto the surface of an ultra pure water bath. We note that for these experiments using perfectly cleaved mica helps to ensure that the entire film of thickness h_m floats cleanly off the mica surface without breaking or wrinkling. Next, a second film with thickness h_m on mica was held using self closing tweezers and carefully placed onto the floating film with the polymer side down, thereby creating a bilayer film of total thickness $2h_m$. The bilayers were then annealed under ambient conditions on a Linkam hostage at 130° C for various times t_b. After annealing, the bilayers were crazed using the procedure described above.

Chapter 3

The papers

In this chapter a brief summary of each of the works I have contributed to over the duration of my M.Sc. is presented. I was not the primary contributor to all of the works presented below. For each project my particular contributions are clearly explained. Following the description of each work and the outline of my contributions, the paper is presented.

Summary of paper 1

Controlling Marangoni induced instabilities in spin-cast polymer films: how to prepare uniform films

Paul D. Fowler, Céline Ruscher, Joshua D. McGraw, James Forrest, and Kari Dalnoki-Veress, to be submitted to European Physical Journal E (2014).

This paper addresses the formation of non-uniform surface topographies in spin-cast polymer films. Although spincoating typically produces flat films, under certain conditions the process results in films with non-uniform surface topographies. Since spincoating is relied upon in both research and industrial settings as a technique to prepare high quality polymer films, the formation of such topographies is a practical problem. Furthermore, a thorough description of the physics governing the formation of non-uniform spincast films remains elusive. In this paper we attempt to address both these problems. We have presented a simple technique to avoid the formation of non-uniform films. Additionally our experiments indicate that non-uniformities in the film thickness form as a result of the Marangoni effect.

For this work, I designed the experiment and developed the sample preparation techniques in collaboration with my supervisor and James Forrest. I performed initial experiments, wrote the MATLAB codes which were used for the data analysis and performed preliminary analysis which confirmed this project's feasibility. Céline Ruscher joined the research group as a visiting student and I co-supervised her throughout her time in the lab. Most of the experiments appearing in the paper were performed by C. Ruscher. Additionally, C. Ruscher completed preliminary data analysis. I performed further analysis and wrote the first draft of the manuscript.

EPJ manuscript No.
(will be inserted by the editor)

Controlling Marangoni induced instabilities in spin-cast polymer films: how to prepare uniform films

Paul D. Fowler[1], Céline Ruscher[1,2] Joshua D. McGraw[3], James Forrest[4], and Kari Dalnoki-Veress[1,5a]

[1] Department of Physics & Astronomy, McMaster University, Hamilton, Ontario, Canada, L8S 4M1
[2] Institut Charles Sadron, Université de Strasbourg, Strasbourg, France
[3] Saarland University, Experimental Physics, 66123 Saarbrücken, Germany
[4] Department of Physics & Astronomy, University of Waterloo, Waterloo, Ontario, Canada, N2L 3G1
[5] Laboratoire de Physico-Chimie Théorique, UMR CNRS 7083 Gulliver, ESPCI ParisTech, PSL Research University.

Received: date / Revised version: date

Abstract. In both research and industrial settings spin coating is extensively used to prepare thin polymer films. Typically spin coating produces highly uniform films, however under certain conditions the spin coating process results in films with non-uniform surface morphologies. Although the spin coating process has been extensively studied, the origin of these morphologies is not fully understood and the formation of non-uniform spincast films remains a practical problem. Here we report on experiments indicating that the formation of surface instabilities during spin coating is dependent on temperature. Our results suggest that non-uniform spin-cast films form as a result of the Marangoni effect. Furthermore, we find that both the wavelength and amplitude of the pattern increase with temperature. Finally, and most important from a practical viewpoint, the non-uniformities in the film thickness can be entirely avoided simply by lowering the the spin coating temperature.

1 Introduction

Spincoating is widely used to produce uniform thin films and has a diverse range of industrial applications including biomedical coatings, microelectronics, and solar cell technology [1–3]. A small amount of polymer dissolved in some volatile solvent is deposited onto a flat substrate which is then rapidly spun (or already spinning) causing most of the solution to be ejected from the substrate. The remaining solvent evaporates leaving behind a polymer film with thicknesses typically on the order of nanometres to microns. In many circumstances this process produces highly uniform films, however under certain conditions spin coating results in films with non-uniform surface morphologies, such as the one shown in fig. 1. Because of its prevalence as a preparation technique, the spincoating process has been widely studied and much effort has gone into characterizing the factors giving rise to such morphologies [4–12]. Although much is known about the spincoating of films, the formation of non-uniform spincast films remains a practical problem in both industrial settings and research laboratories.

One of the first successful theoretical models of spincoating was developed by Emslie *et al.* [13] who solved the equations of motion for a non-volatile Newtonian fluid on a rotating disk, by equating centrifugal and viscous forces. Although this model captures the fundamental physics of spin coating, the actual process is significantly more complicated. In practice, films are typically spin-cast from polymer solutions, meaning effects such as surface tension, shear thinning and elasticity must be considered. Furthermore, as spinning proceeds, the properties of the solution change due to solvent evaporation. Later models incorporated some of these effects. In [14], Flack *et al.*, proposed a model which includes the non-Newtonian properties of the solution as well as changes in the solution viscosity due to solvent evaporation. This model breaks the spincoating process into two stages, the first

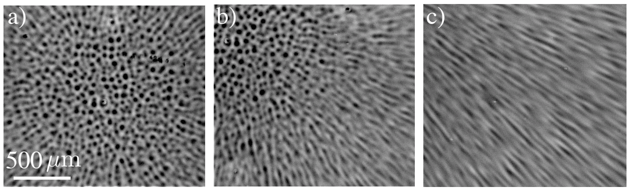

Fig. 1. Optical microscopy images of the typical ‘flowering morphology’ observed in our experiments. (a) The centre of the image corresponds to the axis of rotation of the spincoater, which we refer to as the ‘spinning centre’. Near the spinning centre, the pattern is isotropic and has a well defined wavelength. (b), (c) Farther from the spinning centre, the morphology turns to striations in the film, which point radially outward from the spinning centre.

---

[a] email: dalnoki@mcmaster.ca

controlled by viscous radial flow of the solution and the second dominated by solvent evaporation. One major success of this model is its successful prediction of the experimentally observed dependence of film thickness on spin speed. Later work [15–18] further investigated the effects of solvent evaporation on the properties of spin-cast films. In [16,17] the authors suggest that the concentration of solvent is constant except in a thin boundary region adjacent to the solution/air interface. For the cases of both slow and rapid solvent evaporation, it is found that the final thickness of the spin-cast film depends on the thickness of the boundary layer. Bornside *et al.* proposed a similar model [18] which incorporates variations in viscosity and diffusivity across the thickness of the film. It is found that under certain conditions, a region of low solvent concentration develops at the free surface. Since this surface layer has a high viscosity and low diffusivity, it behaves like a 'solid skin' which retards solvent evaporation. The authors propose that if solvent evaporation is rapid enough, the solid skin will develop while there is still flow in the liquid below, leading to hydrodynamic instabilities. This, in turn, causes inhomogeneities in the film. Such morphologies have been observed in the literature, [4,7–10,19] leading to many further studies on the formation of instabilities during spincoating [11,20–23]. In particular, de Gennes proposed a model to describe the formation of a solid skin or 'crust' which includes an estimate for the minimum film thickness required to develop instabilities [5,6]. Some authors have argued against crust formation, instead suggesting the formation of non-uniform films is driven by the Marangoni effect [4,10,24,12]. To date, the problem remains unsolved and due to the complexity of the spincoating process, efforts to combat the formation of non-uniform films are largely empirically based.

Experimentally, the spincoating process has been extensively studied. It is well known that the properties of a spin-cast film depend on numerous factors including spin speed, solution concentration, solution viscosity and vapour pressure [1,19,25]. More recent literature highlighting the complexity of the process has shown that spincoating may also affect fundamental material properties of the film such as the entanglement network and viscosity [26–30]. Despite significant advancements in the understating of spincoating, it remains an outstanding goal to control the morphology of thin polymer films. One well studied case is that of phase separation in spin-cast polymer blends. In addition to characterizing how the morphology depends on factors such as polymer concentration and spin speed [31–34], more complex effects have been investigated, including confinement [35] and the patterning of substrates [36]. Pattern formation in spin-cast diblock-copolymer films has also received significant attention [37,38]. Furthermore, many authors have studied the morphology of films spin-cast from complex solutions such as colloidal suspensions and sol-gels [4,39–41].

Here, we are primarily focused on the simple and common case of spincoating a thin film from a polystyrene/toluene solution. As mentioned above, non-uniformities are typically attributed to either the formation of a crust or the Marangoni effect. In the case of a Marangoni process, gradients in surface tension drive the formation of convection cells, which ultimately lead to variations in the film thickness. Surface tension gradients may arise due to gradients in temperature or concentration. In either case, once the surface tension gradient has been established, solution begins to flow from the region of low surface tension, toward the area of high surface tension. As liquid flows away from the low surface tension regions, fluid must come in to take its place. Under certain conditions, this effect is amplified and convection cells form. The Marangoni effect has been used to explain pattern formation in spin-cast films and in films formed through the drying of a polymer solution [10,12,24,42]. The details of the Marangoni effect have been known for years [43–45,21,46,47,22] but to date there are few experimental techniques to combat the formation of Marangoni induced instabilities in spin-cast films. In [18] it was suggested that saturating the environment above the solution/air interface with solvent may help to prevent the development of instabilities. Although this technique is routinely used in many research laboratories, the setup can be cumbersome and its success depends on the particular combination of polymer/solvent in use. Other authors have proposed that by appropriately mixing solvents, instabilities can be avoided [7]. Though also practiced in many laboratories, this approach can be tedious and depends on many factors like the molecular weight of the polymer, solubility, solvent ratios and potentially phase separation during spincoating.

In this work we have systematically studied the effects of temperature on the formation of non-uniformities in spin-cast polymer films. We find that the wavelength and amplitude of the morphology is dependent on the spinocating temperature. Furthermore, our results show that the wavelength of the pattern scales with the film thickness which suggests that the formation of thickness variations is driven by a Marangoni process. From a practical perspective, we find that non-uniformities in the film thickness can be entirely avoided, simply by decreasing the spin-coating temperature.

2 Experiment

Samples were prepared using polystyrene (PS) with of nine different weight averaged molecular weights, $8.8 \leq M_w \leq 758.9$ kg/mol, each with a polydispersity index less than 1.10 (Polymer Source, Inc.). Experiments were also performed using a symmetric diblock co-polymer, poly-(styrene-methyl methacrylate) (PS-PMMA) with a total molecular weight of 211 kg/mol and a polydispersity index of 1.13 (Polymer Source Inc.). Each polymer was dissolved into toluene (Fisher Scientific, Optima grade) in various weight fractions ranging from $\phi = 1.5$ to $\phi = 4.5$ wt%. Films were spincast onto clean 20 mm × 20 mm Si wafers (University Wafer) using a spin speed of $\omega = 4000$ rpm. The resulting films ranged in thickness from 100-200 nm.

Spincoating was performed using a simple setup which allowed control of the spincoating temperature. Si wafers were placed onto a large home made aluminum disk, which

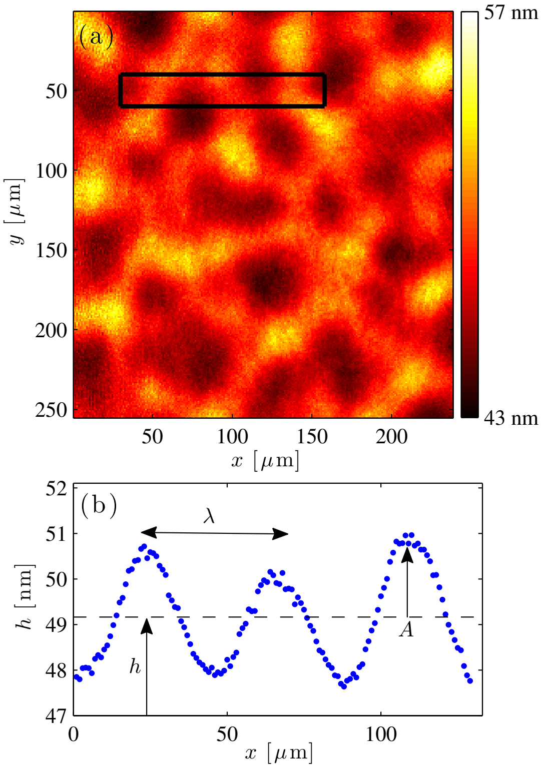

Fig. 2. (a) IE measurement of the topography of a spin-cast film near the spinning centre. (b) Typical height profile of a film. The profile is an average over the region contained in the black box shown in (a). The amplitude (A), the average film thickness (h), maximum film thickness (h_+), minimum film thickness (h_-) and wavelength (λ) are defined in the plot.

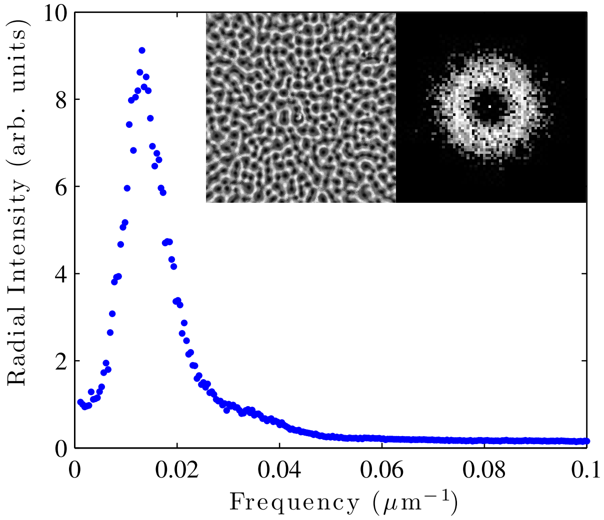

Fig. 3. Radial intensity as a function of frequency obtained from the FFT and contrast enhanced OM image shown in the inset. The bright ring in the FFT, which represents the characteristic frequency in the image corresponds to the sharp peak in the radial intensity.

we refer to as the spincoater chuck, and held in place using small screws. With screws holding the substrate onto the chuck good thermal contact is ensured. The temperature of the chuck was adjusted by placing it on either a heater or in a cooled environment. A thermocouple embedded well within the chuck[1] was used to monitor its temperature, which ranged from $15 \leq T \leq 60\,°$C. Once the chuck reached the desired temperature, it was transferred onto a commercial spincoating apparatus (Headway Research Inc., Model PWM32). Several drops of the polymer/toluene solution were placed onto the wafer and the chuck was rotated at 4000 rpm. Immediately prior to spinning, the thermocouple temperature was recorded and then removed from the chuck.

Since the substrate is in good thermal contact with the chuck and the thermal mass of the solution is negligible compared to the chuck/substrate, we assume that the temperature of the solution is that of the chuck at the start of spinning. To test this, a second thermocouple was used to probe the temperature of the solution immediately following its deposition onto the substrate. The temperature difference between the chuck and solution was less than 1°C, which is within experimental error. Having confirmed that the temperature of the solution can be assumed to be that of the chuck, for all subsequent experiments only the temperature of the chuck at the start of spinning was recorded. We emphasize that spincoating was carried out under typical spincoating conditions: at ambient temperature and in air. Throughout this work the spincoating temperature refers to the temperature of the spincoater chuck at the onset of spinning.

In fig. 1 is shown an optical microscopy (OM) image of the typical 'flowering morphology' observed in our experiments. The variations in the intensity of the greyscale OM image results from the varying reflectivity of the thin transparent film atop the reflective substrate. Thus, the variations in the intensity are related to varying film thickness. Near the centre of the film, the pattern is isotropic with a well defined wavelength. Toward the edge of the film, this pattern turns into radial variations in the film thickness. To characterize this morphology, samples were imaged using both OM and imaging ellipsometry (IE) (Accurion, EP3). Here we focus on the isotropic region near the centre of film and investigate how the amplitude and wavelength of this pattern change with temperature.

Amplitude: Fig. 2(a) shows a typical map of the topography in the central region of the film as measured with imaging ellipsometry. From images such as these we are able extract a height profile of the film. In fig. 2(b) is shown an example of a height profile, where we have

---

[1] The thermocouple is inserted through a small diameter hole that enters deep into the side of the chuck. The contact of the thermocouple well within the large thermal mass ensures an accurate temperature reading as well as easy insertion and removal of the thermocouple.

defined h as average film thickness and h_+ and h_- as the maximum and minimum film thicknesses respectively. The amplitude (A) is defined as half the height difference between the maximal and minimal film thicknesses. The wavelength (λ) is defined as the average distance over which the pattern repeats. For all data shown below, the reported amplitude is an average over multiple ellipsometry measurements of at least 5 samples.

Wavelength: The wavelength was calculated using a two-dimensional Fast Fourier Transform (FFT). The OM image of the central region of the film was contrast enhanced prior to the FFT in order to increase the signal-to-noise ratio. The inset of fig. 3 shows a typical optical image, after contrast enhancement along with its FFT. The bright ring seen in the FFT corresponds to the characteristic frequency in the image. Taking a radial average of the intensity gives the peak frequency of the flowering pattern, which is easily converted into the wavelength. In fig. 3 is shown the plot of radial intensity as a function of frequency which corresponds to the optical image and FFT shown the inset of the figure. For all samples analyzed in our experiments, there is sharp peak in the radial intensity of the FFT, resulting in a well defined wavelength. The reported wavelength represents the average value of measurements taken from 5 to 10 films.

3 Results and discussion

This section is divided into three parts. In sections 3.1 and 3.2 we present the results of experiments performed with spincoating temperatures above ambient temperature. We have systematically studied how both the wavelength and amplitude of the flowering morphology change with increasing spincoating temperature. We establish that the formation of the flowering pattern is consistent with a Marangoni driven process. Finally, in section 3.3 we discuss experiments performed with spincoating temperatures below ambient temperature. We show that by spin-coating at cooler temperatures we are able to suppress the formation of non-uniform films.

3.1 Wavelength

In fig. 4 is shown the results of experiments for films spin-cast from a solution of PS(183k) with $\phi = 2.5\%$ as a function of the spincoating temperature, T. Fig. 4(a) shows a plot of the wavelength as a function of spincoating temperature. In fig. 4(b) is shown the average film thickness plotted as a function of the spincoating temperature. We find that both the wavelength of the flowering morphology and the average film thickness increase linearly with spincoating temperature. Combining the data in figs. 4(a) and (b), we plot the wavelength as a function of the average film thickness in fig. 4(c).

As mentioned in section 1, non-uniformities in spin-cast polymer films are typically attributed to either the formation of a crust at the free surface, or the Marangoni effect [5,6,10,12]. The linear relationship between wavelength and average film thickness shown in fig. 4(c) is suggestive of a Marangoni process [24,45,22]. Marangoni convection is driven by surface tension and there are two clear mechanisms which can result in surface tension gradients across the polymer solution. First, since the solution is heated from below by the spincoater chuck with evaporative cooling at the free interface, there is a temperature gradient across the solution. If there is any perturbation to the free surface, the region of solution which is closer to the heated chuck will be hotter than the fluid which has been pushed away from the substrate. Since surface tension decreases with temperature, the regions of interface which are closer to the heated chuck will have a lower surface tension compared to those farther from the chuck. This gradient in surface tension drives flow. High surface tension regions pull fluid along the interface away from the areas of low surface tension. As solution moves away from areas of low surface tension, fluid from below flows to take its place. Normally, this surface tension driven flow is mediated by viscosity and thermal diffusion and the liquid flattens. However, under certain conditions, the flow induced by surface tension gradients is amplified leading to the formation of convection cells in the liquid. The balance between surface forces and dissipation due to thermal diffusivity and viscosity is characterized by the dimensionless Marangoni number,

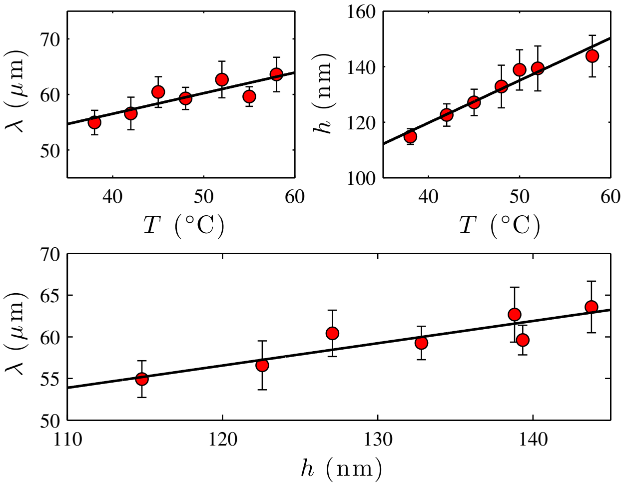

Fig. 4. Measurements of the wavelength and average film thickness as a function of spincoating temperature for films spin-cast from a $\phi = 2.5\%$ solution of PS(183k). Here, each data point represents an average of measurements taken from many films and the distance from the top to bottom of an error bar is the standard deviation. (a) Plot of wavelength as a function of spincoating temperature. (b) Plot of average film thickness as a function of spincoating temperature. (c) Plot of wavelength as a function of average film thickness, obtained from the data in (a) and (b).

$$M = -\frac{d\gamma}{dT}\frac{h\varDelta T}{\eta\alpha} \tag{1}$$

where h is the thickness of the fluid, α the thermal diffusivity and $\varDelta T$ the temperature gradient across the fluid. It has been shown that in order for a Marangoni instability to occur, M must exceed some critical value, M_c [45,48]. Marangoni convection cells can also form as a result of concentration gradients induced by rapid solvent evaporation. Concentration gradients along the free surface establish surface tension gradients which drive the formation of convection cells via the mechanism described above. Due to the complexity of our system, we cannot determine whether the Marangoni process is triggered by gradients in temperature or concentration and it may be the combination of the two effects.

To summarize, we find that both the wavelength of the flowering morphology and the average film thickness increase linearly with the spincoating temperature. Together, these results imply that the wavelength scales with the average film thickness, which is consistent with a Marangoni process [24,45,22]. We note that the measurements shown in fig. 4 (a) and (b) were repeated with varying solution concentrations ranging from $\phi = 1.5$ to $\phi = 4.5$ and for nine PS molecular weights ranging from 8.8 kg/mol to 759 kg/mol (not shown). In all cases, the same trend exemplified in fig. 4 (a) and (b) was observed: the wavelength and average film thickness increase linearly with temperature.

3.2 Amplitude

In the previous section, we established that the formation of the flowering morphology is consistent with a Marangoni process. We now present the results of experiments investigating the affect of temperature on the amplitude of the flowering pattern. In fig. 5(a) is shown a plot of the amplitude as a function of spincoating temperature for films spincast from a $\phi = 2.5\%$ solution of PS(183k). The data in fig. 5(a) shows that the amplitude increases linearly with the spincoating temperature. To explain this trend, we compare with the results of recent studies on the formation of non-uniformities in spin-cast polymer films. In work by Müller-Buschbaum *et al.* the morphology of films spin-cast from various solvents was studied [7]. Qualitatively, the patterns observed in [7] appear similar to those presented in this work. The authors found that the surface roughness of the films increased with increasing vapour pressure. Strawhecker *et al.* also studied morphologies similar to the flowering patterns seen here and found that the surface roughness increased as a function of vapour pressure [10]. To explain this result, the authors propose that the morphologies form during the early stages of spincoating and depend on the competition between two phenomena: 1) The temperature gradient induced by rapid solvent evaporation leads to Marangoni instabilities which roughen the surface. 2) The solution is driven to level in order to minimize the surface energy. To describe the competition between these two effects, the authors define the ratio between the levelling time and evaporation time as [10]

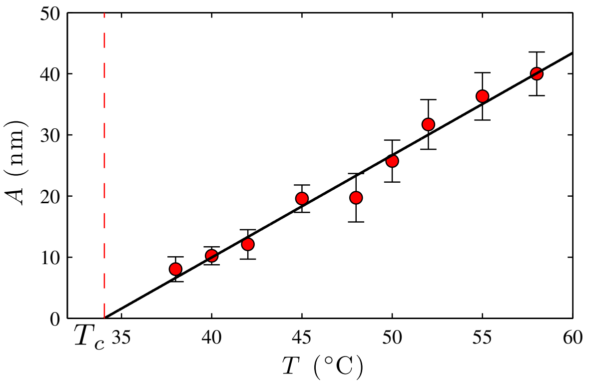

Fig. 5. Measurements of the amplitude as a function of spincoating temperature for films spin-cast from a $\phi = 2.5\%$ solution of PS(183k). Each data point represents an average of many measurements taken with IE and the distance from the top to bottom of an error bar is the standard deviation. The critical temperature T_c is defined by the intersection of the best-fit straight line with the T axis, as indicated by the vertical dashed line.

$$\varLambda = \frac{\tau_{level}}{\tau_{evap}} \propto \frac{\eta E}{\gamma\rho\theta^{m+1}} \tag{2}$$

where η, E, γ and ρ are the viscosity, evaporation rate, surface tension and density of the solvent. θ is the contact angle of a drop of solution and m a positive exponent. During the early stages of spincoating, the dilute solution has a low viscosity and there is a competition between the levelling of the surface and the formation of Marangoni induced roughness. As solvent evaporates, the viscosity increases and eventually the film 'freezes'. If the film vitrifies before the surface has time to level, the resulting film will be non-uniform. Increasing the evaporation rate, reduces the time the film has to flatten before it vitrifies, which leads to rougher films. The authors note that since evaporation rate increases with vapour pressure this simple picture is consistent with their experiment results. This model also explains the trend of increasing roughness with increasing vapour pressure observed in [7]. Similarly, the results shown in fig 5(a) are consistent with the ideas presented in [10]. Increasing the spincoating temperature leads to more rapid solvent evaporation and therefore rougher films. We also note that increasing the spincoating temperature increases both surface tension gradients and the temperature gradient across the polymer solution while lowering the solution viscosity. Therefore raising the spincoating temperature increases the convection velocity and the driving force for Marangoni instabilities. Thus, according to eq. 1 the incerease in the amplitude is consistent with the increasing value of M as the spincoating temperature is increased.

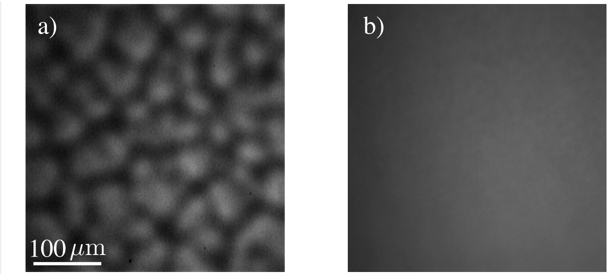

Fig. 6. Optical microscopy images of films spin-cast from a $\phi = 3.5\%$ solution of PS-PMMA. (a) Films spin-cast at room temperature ($T_a \approx 22°$C) exhibit a flowering morphology. (b) Spincoating at $T = 15°$C results in uniform films.

3.3 Cooling experiments

In the results presented above, we have examined how increasing the spincoating temperature affects the wavelength and amplitude of the flowering morphology. We now present the results of experiments performed with spincoating temperatures below room temperature. In fig. 6 are shown optical microscopy images of two films spin-cast from the same $\phi = 3.5\%$ solution of PS-PMMA, one at room temperature, the other at $T = 15°$C. For the film spin-cast at room temperature, $T_a \approx 22°$C, we observe a flowering morphology (fig. 6(a)). The film spin-cast at $T = 15°$C is uniform (fig. 6(b)). This experiment was repeated with varying solution concentrations of PS-PMMA and in each case it was found that films spin-cast at room temperature had variations in the thickness, while spincoating below room temperature resulted in uniform films. This suggests that reducing the spincoating temperature is a simple technique to combat the formation of non-uniform spin-cast films.

This phenomenon is easily explained in the context of the Marangoni effect. As discussed in section 3.1, the formation of convection cells depends the balance of surface tension and dissipation due to thermal diffusivity and viscosity, which is expressed by the Marangoni number (eq. (1)).

Spincoating at cooler temperatures reduces the temperature gradient across the solution caused by evaporative cooling. According to eq. (1), $M \propto \Delta T$ so lowering the spincoating temperature decreases the Marangoni number. If the solution is sufficiently cooled, the Marangoni number will fall below the critical value, $M < M_c$, and the resulting film will be flat.

Furthermore, we can define the critical temperature, T_c as the onset temperature for Marangoni instabilities. That is for spincoating temperatures, $T > T_c$, films exhibit the flowering morphology but films spin-cast at $T < T_c$ are uniform. In fig. 5, T_c is defined by the intersection of the best-fit straight line with the T axis. For the case of PS(183k) shown in fig. 5, T_c is above room temperature ($T_a \approx 22°$) and films can be spin-cast under ambient conditions. However as shown in fig. 6(a) PS-PMMA films spin-cast at room temperature are non-uniform meaning $T_c > T_a$. However, by sufficiently reducing the spincoating temperature such that $T < T_c$, we are able to prepare uniform films, as shown in fig. 6(b).

4 Conclusion

In this work we have presented a systematic study on the effect of temperature on the formation of non-uniformities in spin-cast polymer films. The 'flowering morphology' observed in our experiments consists of an isotropic distribution of cells near the centre of the film, which turn to radial striations in the thickness toward the edge of the sample. We have measured the wavelength and amplitude of the central region of the pattern as a function of the spincoating temperature. We find a linear relationship between the wavelength and average film thickness which suggests the formation of the flowering morphology is driven by a Marangoni process.

Our results also show that the amplitude of the pattern increases linearly with spincoating temperature. We are able to explain this trend using the fact that evaporation rate increases with spincoating temperature. At higher temperatures the film has less time to flatten before vitrifying, which results in rougher films. This idea is consistent with previous studies showing that films spin-cast from more volatile solvents have rougher surfaces.

Finally, we have presented a simple experimental technique to combat the formation of non-uniform films. By spincoating films at cooler temperatures we are able to entirely avoid the formation of non-uniformities in the film thickness. This result is easily explained using the Marangoni effect. The Marangoni number is proportional to the temperature gradient across the solution, $M \propto \Delta T$. Spincoating at cool temperatures decreases the temperature gradient across the solution, therefore decreasing the Marangoni number. If the sample is sufficiently cooled, the Marangoni number will be lower than the critical value required to form an instability ($M < M_c$), and the resulting film will be uniform. We emphasize that spincoating at cooler temperatures is easy to implement, though care must be take to avoid condensation of water from the air if spincoating in air. For our experiments spincoating at low temperatures was performed with a simple home-built setup; however, for an athermal solvent the same effect can be achieved by placing the polymer solution in a cooled environment several minutes prior to spinning. We are hopeful that this protocol may be useful in both research and industrial settings where the formation of non-uniform spin-cast films may be undesirable.

The authors thank NSERC for financial support.

References

1. K. Norrman, A. Ghanbari-Siahkali, and N. B. Larsen, Annu. Rep. Prog. Chem., Sect. C **101**, 174 (2005).
2. H. Sirringhaus, Science **280**, 1741 (1998).
3. S. Walheim, Science **283**, 520 (1999).
4. D. P. Birnie, J. Mater. Res. **16**, 1145 (2011).

5. P.-G. de Gennes, Eur. Phys. J. E **7**, 31 (2002).
6. P.-G. de Gennes, Eur. Phys. J. E **6**, 421 (2001).
7. P. Müller-Buschbaum, J. S. Gutmann, M. Wolkenhauer, J. Kraus, M. Stamm, D. Smilgies, and W. Petry, Macromolecules **34**, 1369 (2001).
8. P. Müller-Buschbaum, J. S. Gutmann, J. Kraus, H. Walter, and M. Stamm, Macromolecules **33**, 569 (2000).
9. P. Müller-Buschbaum and M. Stamm, Macromolecules **31**, 3686 (1998).
10. K. E. Strawhecker, S. K. Kumar, J. F. Douglas, and A. Karim, Macromolecules **34**, 4669 (2001).
11. C.-T. Wang and S.-C. Yen, Chemical engineering science **50**, 989 (1995).
12. D. P. Birnie, III, Langmuir **29**, 9072 (2013).
13. A. G. Emslie, F. T. Bonner, and L. G. Peck, J. Appl. Phys. **29**, 858 (1958).
14. W. W. Flack, D. S. Soong, A. T. Bell, and D. W. Hess, J. Appl. Phys. **56**, 1199 (1984).
15. C. J. Lawrence, Phys. Fluids **31**, 2786 (1988).
16. C. J. Lawrence, Phys. Fluids A **2**, 453 (1990).
17. C. J. Lawrence and W. Zhou, Journal of non-newtonian fluid mechanics **39**, 137 (1991).
18. D. E. Bornside, C. W. Macosko, and L. E. Scriven, J. Appl. Phys. **66**, 5185 (1989).
19. L. L. Spangler, J. M. Torkelson, and J. S. Royal, Polymer Engineering & Science **30**, 644 (1990).
20. B. Reisfeld, S. G. Bankoff, and S. H. Davis, J. Appl. Phys. **70**, 5258 (1991).
21. R. Craster and O. Matar, Rev. Mod. Phys. **81**, 1131 (2009).
22. A. Oron, S. H. Davis, and S. G. Bankoff, Rev. Mod. Phys. **69**, 931 (1997).
23. A. Münch, C. P. Please, and B. Wagner, Phys. Fluids **23**, 102101 (2011).
24. N. Bassou and Y. Rharbi, Langmuir **25**, 624 (2009).
25. D. Meyerhofer, J. Appl. Phys. **49**, 3993 (1978).
26. D. R. Barbero and U. Steiner, Phys. Rev. Lett. **102**, 248303 (2009).
27. K. Thomas, A. Chenneviere, G. Reiter, and U. Steiner, Phys. Rev. E **83**, 021804 (2011).
28. A. Raegen, M. Chowdhury, C. Calers, A. Schmatulla, U. Steiner, and G. Reiter, Phys. Rev. Lett. **105**, 227801 (2010).
29. G. Reiter, M. Hamieh, P. Damman, S. Sclavons, S. Gabriele, T. Vilmin, and E. Raphaël, Nat Mater **4**, 754 (2005).
30. J. D. McGraw, P. D. Fowler, M. L. Ferrari, and K. Dalnoki-Veress, Eur. Phys. J. E **36**, 7 (2013).
31. K. Dalnoki-Veress, J. A. Forrest, J. R. Stevens, and J. R. Dutcher, Physica A: Statistical Mechanics and its Applications **239**, 87 (1997).
32. S. Walheim, M. Böltau, J. Mlynek, G. Krausch, and U. Steiner, Macromolecules **30**, 4995 (1997).
33. S. Y. Heriot and R. A. L. Jones, Nat Mater **4**, 782 (2005).
34. D. T. W. Toolan and J. R. Howse, J. Mater. Chem. C (2013).
35. K. Dalnoki-Veress, J. A. Forrest, and J. R. Dutcher, Phys. Rev. E **57**, 5811 (1998).
36. M. Böltau, S. Walheim, J. Mlynek, G. Krausch, and U. Steiner, Nature **391**, 877 (1998).
37. P. F. Green and R. Limary, Advances in Colloid and interface Science **94**, 53 (2001).
38. S. H. Kim, M. J. Misner, and T. P. Russell, Adv. Mater. **16**, 2119 (2004).
39. D. J. Taylor and D. P. Birnie, Chem. Mater. **14**, 1488 (2002).
40. T. J. Rehg and B. G. Higgins, AIChE Journal **38**, 489 (1992).
41. Y. Zhao and J. S. Marshall, Phys. Fluids **20**, 043302 (2008).
42. S. Sakurai, C. Furukawa, A. Okutsu, A. Miyoshi, and S. Nomura, Polymer **43**, 3359 (2002).
43. M. J. Block, Nature **178**, 650 (1956).
44. L. E. Scriven and C. V. Sternling, Nature **187**, 186 (1960).
45. J. Pearson, J. Fluid Mech **4**, 489 (1958).
46. M. F. Schatz and G. P. Neitzel, Annual review of fluid mechanics **33**, 93 (2001).
47. D. Johnson and R. Narayanan, Chaos **9**, 124 (1999).
48. M. F. Schatz, S. J. Vanhook, W. D. McCormick, J. B. Swift, and H. L. Swinney, Phys. Rev. Lett. **75**, 1938 (1995).

Summary of paper 2

Approach to universal self-similar attractor for the levelling of thin liquid films
Michael Benzaquen*, Paul Fowler*, Laetitia Jubin, Thomas Salez, Kari Dalnoki-Veress and Elie Raphaël, Soft Matter, in press, DOI: 10.1039/C4SM01483A.

This paper is a study investigating the capillary driven levelling of surface perturbations to thin polystyrene films. We prepare samples with various surface geometries and follow their evolution above T_g as capillary forces drive the surface to flatten. We find that the surface profiles are self-similar at long times in accordance with predictions of the two-dimensional thin film equation. Furthermore, all profiles converge toward a universal self-similar attractor as expected from theory. We show that the time taken to converge to the this attractor depends on the volume of the perturbation. Finally, we measure the convergence time of various surface perturbations and find excellent agreement between theory and experiment.

This project was motivated by Michael Benzaquen's previous theoretical study on the convergence of surface perturbations to a universal self similar attractor [31]. M. Benzquen and his supervisor E. Raphaël proposed experiments testing some of the predictions presented in this work. In collaboration with my supervisor, I developed the sample preparation techniques required to create polymer films with random surface perturbations. Laetitia Jubin joined the group as a visiting student and I co-supervised her work on this project. L. Jubin performed approximately half of the measurements presented in this work. I performed further experiments and wrote the MATLAB scripts which were used to analyze the data. I did the data analysis which was guided by M. Benzaquen's theoretical predictions. The manuscript was a collaboration between authors. M. Benzaquen wrote the theory sections of the first draft while I prepared the experimental sections and the figures. Because this paper represents a very equal contribution of the theory, led by Benzaquen, and the experiments led by me, we share 'first authorship' on this paper.

---

*These authors contributed equally to this work.

Soft Matter

PAPER

View Article Online
View Journal

Cite this: DOI: 10.1039/c4sm01483a

Approach to universal self-similar attractor for the levelling of thin liquid films

Michael Benzaquen,†[a] Paul Fowler,†[b] Laetitia Jubin,[b] Thomas Salez,[a] Kari Dalnoki-Veress[ab] and Elie Raphaël*[a]

Received 8th July 2014
Accepted 6th August 2014

DOI: 10.1039/c4sm01483a

www.rsc.org/softmatter

We compare the capillary levelling of a random surface perturbation on a thin polystyrene film with a theoretical study on the two-dimensional capillary-driven thin film equation. Using atomic force microscopy, we follow the time evolution of samples prepared with different initial perturbations of the free surface. In particular, we show that the surface profiles present long term self-similarity, and furthermore, that they converge to a universal self-similar attractor that only depends on the volume of the perturbation, consistent with the theory. Finally, we look at the convergence time for the different samples and find very good agreement with the analytical predictions.

1 Introduction

In the past decades, thin films have been of undeniable interest to scientific and industrial communities.[1–3] Indeed, understanding the dynamics and stability of thin films is essential to technological applications such as nanolithography[4,5] and the development of non-volatile memory storage devices.[6] Moreover, thin films have enabled the study of the effect of confinement on polymers.[7–16] Several experiments have been performed in order to gain insights into the dynamics of these films. Examples are provided by the broad class of dewetting experiments,[17–29] as well as studies on capillary levelling.[30–40] Levelling experiments on thin polymer films in the vicinity of the glass transition temperature have recently given insights into the surface flow in glassy polymers.[41] The effect of viscoelasticity related to the polymeric nature of these films has been addressed as well.[42–44]

Thin liquid films are also of great interest to the hydrodynamics and applied mathematics community, as the viscous relaxation of a perturbed free surface is described by a nonlinear partial differential equation that, to date, remains only partially solved. This equation is called the capillary-driven thin film equation.[1–3] Several analytical[45–47] and numerical[48] studies have led to a deeper understanding of its mathematical features. Recently, it was shown that the solution of the thin film equation for any sufficiently regular initial surface profile uniformly converges in time towards a universal self-similar attractor that is given by the Green's function of the linear capillary-driven thin film equation.[47] In the terminology of Barenblatt,[49] this attractor corresponds to the intermediate asymptotic regime. "Intermediate" refers to time scales that are large enough for the system to forget the initial condition, but also far enough from the generally predictable final equilibrium steady state; which, for capillary-driven thin films is a perfectly flat surface. For thin films, the question of the convergence time to this universal attractor has not been addressed so far and is the focus of this paper.

Here, we report on levelling experiments on thin polystyrene films that corroborate the theoretical predictions on the convergence of the surface profiles to a universal self-similar attractor. In the first part, we recall the main results of the theoretical derivation of the intermediate asymptotic regime, and address the question of the convergence time. In the second part, we present the experiments where we follow the time evolution of samples prepared with different random initial perturbations of the free surface. Consistent with the theory, we show that the surface profiles present long term self-similarity, and converge to a universal self-similar attractor that only depends on the volume of the perturbation. In particular, the convergence times measured in the different samples show very good agreement with the theory.

2 Theory

Here we recall the main theoretical results from our previous work,[47] and derive an expression for the convergence time as a function of the volume of the perturbation.

2.1 Levelling of a thin liquid film

The levelling of a supported thin liquid film can be described within the lubrication approximation. Assuming incompressible viscous flow, together with a no-slip boundary condition at

---

[a] *Laboratoire de Physico-Chimie Théorique, UMR CNRS 7083 Gulliver, ESPCI ParisTech, PSL Research University, France. E-mail: elie.raphael@espci.fr*

[b] *Department of Physics & Astronomy, The Brockhouse Institute for Materials Research, McMaster University, Hamilton, Canada*

† These authors contributed equally to this work.

the substrate and a no-stress boundary condition at the free surface, yields the so-called capillary-driven thin film equation:[1–3]

$$\partial_t h + \frac{\gamma}{3\eta}\partial_x\left(h^3\partial_x{}^3 h\right) = 0, \tag{1}$$

where $h(x, t)$ is the thickness of the film at position x and time t, γ is the surface tension, and η is the viscosity. Eqn (1) can be nondimensionalised through $h = h_0H$, $x = h_0X$ and $t = (3\eta h_0/\gamma)T$, where h_0 is the equilibrium thickness of the film infinitely far from the perturbation. This leads to:

$$\partial_T H + \partial_x(H^3\partial_x{}^3 H) = 0. \tag{2}$$

The height of the film can be written as $h(x, t) = h_0 + \delta(x, t)$, where $\delta(x, t)$ is the perturbation that levels with the passing of time. For the case of small perturbations compared to the overall thickness of the film, eqn (2) can be linearised by letting $H(X, T) = 1 + \Delta(X, T)$ where $\Delta(X, T) \ll 1$. This yields the linear thin film equation:

$$\partial_T\Delta + \partial_x{}^4\Delta = 0\,. \tag{3}$$

For a given sufficiently regular initial condition $\Delta(X, 0) = \Delta_0(X)$, the solution of eqn (3) is given by:

$$\Delta(X, T) = \int \mathrm{d}X'\,\mathcal{G}(X - X', T)\Delta_0(X')\,, \tag{4}$$

where $\mathcal{G}$ is the Green's function of eqn (3), and reads:[47]

$$\mathcal{G}(X, T) = \frac{1}{2\pi}\int \mathrm{d}K\ \mathrm{e}^{-K^4T}\ \mathrm{e}^{iKX}. \tag{5}$$

By 'sufficiently regular', we mean in particular that the initial perturbation of the profile is summable, with a non-zero algebraic volume, and that this perturbation vanishes when $X \to \pm\infty$. The Green's function is obtained by taking the spacial Fourier transform of eqn (3). Eqn (4) and (5) are central to the problem as, for a given initial condition, they give the profile at any time.

2.2 Universal self-similar attractor

Guided by the mathematical structure of eqn (3), we introduce the self-similar change of variables: $U = XT^{-1/4}$ and $Q = KT^{1/4}$, together with $\breve{\Delta}(U, T) = \Delta(X, T)$. These variables, together with eqn (4) and (5), yield:

$$\breve{\Delta}(U, T) = \int \mathrm{d}X'\breve{\mathcal{G}}\left(U - X'T^{-1/4}, T\right)\Delta_0\left(X'\right), \tag{6}$$

where $\breve{\mathcal{G}}(U, T) = T^{-1/4}\phi(U)$, and:

$$\phi(U) = \frac{1}{2\pi}\int \mathrm{d}Q\,\mathrm{e}^{-Q^4}\ \mathrm{e}^{iQU}. \tag{7}$$

Note that the integral in eqn (7) can be expressed in terms of hypergeometric functions (see the Appendix). The main result from our previous work[47] was that, for any given initial condition $\Delta_0(X)$ the rescaled solution $T^{1/4}\breve{\Delta}(U, T)/\mathcal{M}_0$, where $\mathcal{M}_0 = \int \mathrm{d}X\Delta_0(X) \neq 0$ is the algebraic volume of the perturbation, uniformly converges in time to $\phi(U)$ (see Fig. 1):

$$\lim_{T\to\infty}\frac{T^{1/4}\breve{\Delta}(U, T)}{\mathcal{M}_0} = \phi(U). \tag{8}$$

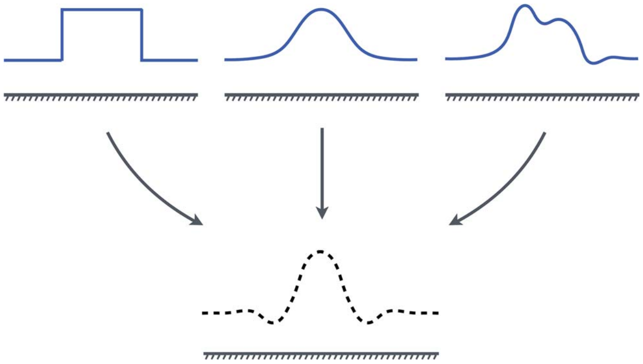

Fig. 1 Schematic illustrating the convergence of any given initial profile to the universal intermediate asymptotic solution.

According to Barenblatt's theory,[49] this is the intermediate asymptotic solution. The solution is universal in the sense that it does not depend on the shape of the initial condition. Note that in the particular case of a zero volume perturbation, the attractor is given by the derivatives of the function $\phi(U)$. The question of the time needed to reach this fundamental solution is important as it quantifies how long one has to wait to forget the initial condition.

2.3 Convergence time

In order to study the approach to the self similar attractor, we look at the surface displacement at $x = 0$ as a function of time. Letting $\Delta_\infty(X, T)$ be the perturbation profile in the intermediate asymptotic regime, then according to eqn (8) at $U = 0$ one has:

$$\Delta_\infty(0, T) = \mathcal{M}_0\phi(0)/T^{1/4}. \tag{9}$$

We then define the convergence time T_c as being the intersection of the initial central height and the central height in the intermediate asymptotic regime:

$$\Delta_0(0) = \Delta_\infty(0, T_c), \tag{10}$$

which leads to:

$$T_c = \left(\frac{\Gamma(5/4)}{\pi}\frac{\mathcal{M}_0}{\Delta_0(0)}\right)^4. \tag{11}$$

Note that the choice of origin, $x = 0$, is arbitrary and will be discussed in the experimental section.

3 Experiments

Samples were prepared using polystyrene (PS) with weight averaged molecular weight $M_w = 31.8$ kg mol^{-1} and polydispersity index PI = 1.06 (Polymer Source Inc.). Solutions of PS in toluene (Fisher Scientific, Optima grade) were prepared with various weight fractions, $1 < \phi < 10$ wt%. Films with thickness h_{Si} were spincast onto clean 10 mm × 10 mm Si wafers (University Wafer) and films with thickness h_{Mi} were spincast onto freshly cleaved 25 mm × 25 mm mica substrates (Ted Pella Inc.).

To prepare samples with various surface geometries the following procedure was used. First, ~10 mm × 10 mm sections of the films prepared on mica were floated onto the surface of an ultrapure water bath (18.2 MΩ cm, Pall, Cascada, LS). These pieces of film were then picked up using the previously prepared films with thickness h_{Si} on the Si substrate. During this transfer, the floating films were intentionally folded back on themselves to create random non-uniform surface geometries. We emphasize that samples were prepared at room temperature, well below the glass transition temperature $T_g \approx 100$ °C. Two types of samples were prepared:

- *Small perturbations*: Films with a relatively small thickness perturbation, where the linear thin film equation is expected to be valid. Such films were prepared with thicknesses $h_{\mathrm{Mi}} \ll h_{\mathrm{Si}}$ to create surface perturbations with $\max[\delta(x, 0)]/h_0 \ll 1$. We used film thickness combinations $\{h_{\mathrm{Si}}, h_{\mathrm{Mi}}\} \approx \{600\text{ nm}, 80\text{ nm}\}$ and $\{200\text{ nm}, 25\text{ nm}\}$.
- *Large perturbations*: Films with large thickness perturbations relative to h_0. Varying geometries were prepared with thicknesses $h_{\mathrm{Mi}} \approx h_{\mathrm{Si}}$ to create surface perturbations with $\max[\delta(x, 0)]/h_0 \sim 1$. Samples were prepared using film thickness combinations $\{h_{\mathrm{Si}}, h_{\mathrm{Mi}}\} \approx \{100\text{ nm}, 100\text{ nm}\}$, $\{150\text{ nm}, 150\text{ nm}\}$, and $\{200\text{ nm}, 200\text{ nm}\}$.

The shapes of the non-uniform perturbations were not prepared by design, rather, during the preparation process many profiles were found on a single sample. Regions of interest were then located and chosen such that, while the height varies in one direction, it is sufficiently invariant in the orthogonal horizontal direction, *i.e.* h can be taken to be a function of x and t alone. Ensuring that the profiles were invariant in one direction was crucial for the comparison with the two-dimensional theory discussed above. Having prepared non-uniform surface perturbations, a second piece of film with thickness h_{Mi} was floated onto a portion of the sample with thickness h_{Si} to create a stepped bilayer geometry, the details of which are fully explained elsewhere.[36] Briefly, the initial height profile of such a step is well described by a Heaviside step function. When a stepped film profile is annealed above T_g the step levels due to capillary forces. For this well defined and well studied geometry, measuring the evolution of the film height profile over time gives an *in situ* measurement of the capillary velocity, γ/η. We emphasize that each sample has *both* the perturbation of interest as well as a region where there is a stepped bilayer. By obtaining the capillary velocity γ/η from the bilayer portion of the sample while also probing the perturbation on the same sample, we reduce the measurement error (for example due to small sample-to-sample variations in annealing temperature). The final stage in the preparation of the samples is 1 min annealing at 130 °C on a hot stage (Linkam Scientific

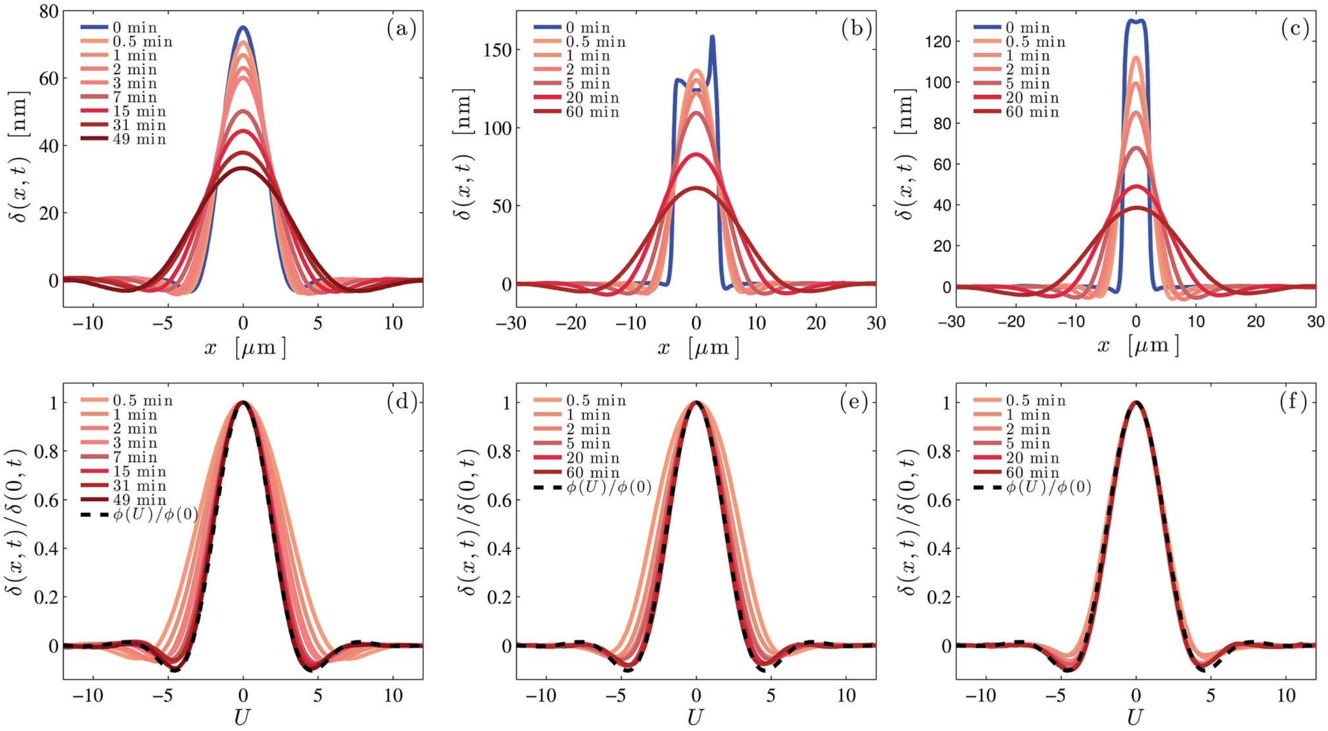

Fig. 2 The results of three experiments on small perturbations. The top panel shows the height of the perturbation, $\delta(x, t) = h(x, t) - h_0$, as a function of position for annealing times $0 \leq t \leq 60$ min for samples with (a) $h_0 = 221$ nm, (b) $h_0 = 681$ nm, and (c) $h_0 = 681$ nm. The bottom row shows the height of the perturbation scaled by the height at $x = 0$ as a function of $U = XT^{-1/4} = x(3\eta/h_0{}^3\gamma t)^{1/4}$. For comparison, we also plot the rescaled self-similar attractor (see eqn (7)) which is shown as a black dashed line in the bottom row.

Instruments Inc.) to ensure that the floated films are in good contact with the substrate film and to remove any water from the system. Note that although there is some evolution of the geometry during this short initial annealing stage, as will become clear below, $t = 0$ is defined after this annealing step.

The initial film height profiles of both the surface perturbation and the stepped bilayer were measured with AFM (Veeco, Caliber). In order to measure the evolution of the surface profiles, samples were annealed under ambient conditions on the hot stage at 140 °C using a heating rate of 90 °C min^{-1}. Above T_g, capillary forces drive the non-uniform surface geometries to level. After sometime the samples were rapidly quenched to room temperature and both the perturbation and bilayer film profiles were measured using AFM. From the AFM scans of the stepped bilayer (not shown), we use the technique described previously[36] to extract the capillary velocity. For all samples we measure the capillary velocity $\gamma/\eta \approx 50$ µm min^{-1}, which is in excellent agreement with previous measurements.[36,39]

4 Results and discussions

4.1 Small perturbations

In Fig. 2(a)–(c) are shown the evolution of three examples of small perturbations, with the highest profiles corresponding to the initial $t = 0$ profiles. Here, we have chosen the coordinate $x = 0$ such that the volume of the perturbation for $x < 0$ is equal to that of $x > 0$. In the initial stages of annealing, the perturbations quickly lose any asymmetry in their shape. With additional annealing, the symmetric profiles broaden and their maximal heights decrease. Since the heights of the linear profiles are small compared to the equilibrium film thicknesses h_0, we expect their evolution to be governed by eqn (3) (the linearized thin film equation). In particular, at long times we expect the profiles to converge to the universal self-similar attractor described in Section 1.2.

To test this prediction we plot the normalized height of the perturbation as a function of the variable $U = XT^{-1/4} = x(3\eta/h_0{}^3\gamma t)^{1/4}$, as shown in Fig. 2(d)–(f). We observe that at late times the profiles converge to the rescaled self-similar attractor $\phi(U)/\phi(0)$ regardless of the initial condition, as predicted in Section 1.2. Here, we emphasize that since we have determined the capillary velocity *in situ* by measuring the evolution of a stepped bilayer geometry near the perturbation on each sample, there is no free parameter in the above rescaling and comparison to the theoretical prediction (shown as a dashed black line in Fig. 2(d)–(f)). Furthermore, at late times, the error between the experimentally measured profiles and the attractor is less than 1%.

4.2 Large perturbations

Measurement of the samples with large perturbations (see the example in Fig. 3) were more challenging because at long annealing times ($t > 100$ min) the lateral extent of the height profiles exceeds the accessible range of the AFM (~100 µm). Here, we resort to imaging ellipsometry (Accurion, EP3) to record height profiles. Imaging ellipsometry (IE) has ~ nm height resolution with lateral resolution comparable to an optical microscope: ~ µm. Thus, IE and AFM are complimentary techniques. For the example in Fig. 3, data were acquired with AFM for $t \leq 63$ min, while IE was used for the three longest annealing times. With IE there is one caveat: in certain ranges of thickness there is a loss of sensitivity depending on the wavelength of laser light and the angle of incidence used (658 nm, 42–50 deg).‡ For the IE data the regions where the IE was insensitive were interpolated with a quadratic spline as indicated by dashed lines to guide the eye.

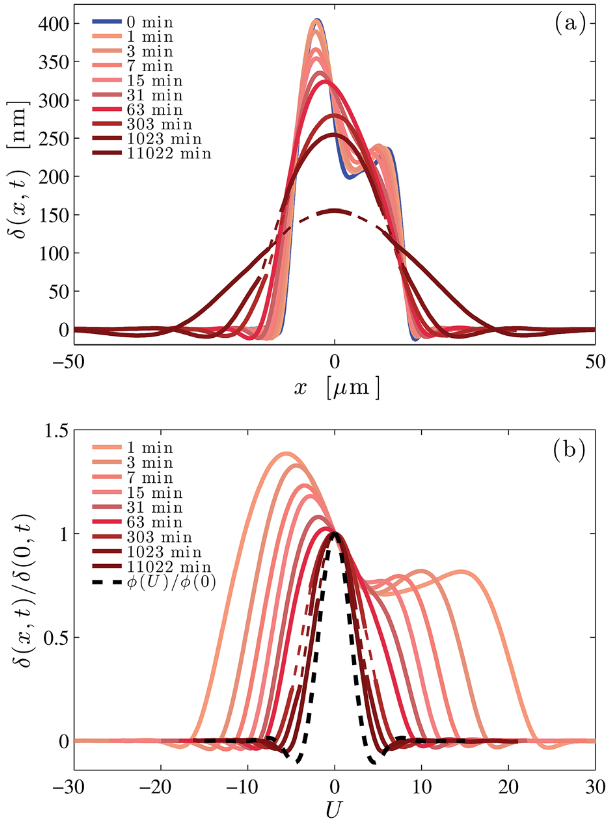

Fig. 3 An example data set with large perturbation. (a) Height of the perturbation as a function of position and annealing time with $h_0 = 216$ nm; (b) the normalized profiles. For times $t \geq 303$ min, profiles were measured using imaging ellipsometry (IE). Regions where IE is insensitive have been interpolated with quadratic splines as indicated by the dashed lines. The black dashed line corresponds to the rescaled self-similar attractor (see eqn (7)).

The evolution of a large perturbation is shown in Fig. 3. In this case, the perturbation does not obey the condition $\delta(0, 0)/h_0 \ll 1$. As can be seen in Fig. 3(a), with sufficient annealing, the large perturbations become symmetric. Similar to the evolution observed for the small perturbations, once the profiles are symmetric, the maximal height $\delta(0, t)$ decreases with further annealing and the profiles broaden.

---

‡ This issue can be circumvented by varying the angle of incidence. However this was not possible for the experiments presented here because changing the angle of incidence also shifts the region of interest slightly.

The normalized profiles are shown in Fig. 3(b). Although the perturbations are initially large, upon long annealing the condition $\delta(0, t) \ll h_0$ can be reached. In particular, the final state of a large perturbation is still expected to be the self-similar attractor. For the data shown in Fig. 3, even after 11 022 min of annealing, the profile did not reach the condition that $\delta(0, t) \ll h_0$. While the height profiles are clearly symmetric at long times, and they converge towards self-similarity, the final profile is not yet equivalent to the final attractor of Fig. 2. The fact that the sample has not yet fully reached the self-similar attractor is simply because the starting profile is so tall, that the long annealing times required and the width of the profile (while still requiring good height resolution) place this outside our experimental window.

4.3 Convergence time

One of the main predictions of the theory outlined in Section 1.3 is that the time taken to converge to the attractor depends on the algebraic volume of the perturbation according to eqn (11). The convergence time is determined in accordance with eqn (10) as the crossover from an initial regime, which is highly dependent on $\delta(x, 0)$, to a universal intermediate asymptotic regime. In Fig. 4, we plot the normalized central height of the perturbation, $\delta(0, t)/\delta(0, 0)$, for the small perturbation shown in Fig. 2(a) and (d). The initial state can be characterized by the central height of the perturbation at $t = 0$ and is given by the horizontal line. At late times, the maximal height of the normalized perturbation $\delta(0, t)/\delta(0, 0)$ decreases in time following the $t^{-1/4}$ power law. Note that the $t^{-1/4}$ line is fit to the last three data points which correspond to the latest profiles shown in Fig. 2(d). These three profiles are in excellent agreement with the calculated asymptotic profile (see the black dashed line in Fig. 2(d)). The crossover from the initial regime to the intermediate asymptotic regime shown in Fig. 4 gives the experimentally determined convergence time, t_c. From t_c, the non-dimensionalized convergence time, T_c, can be obtained.

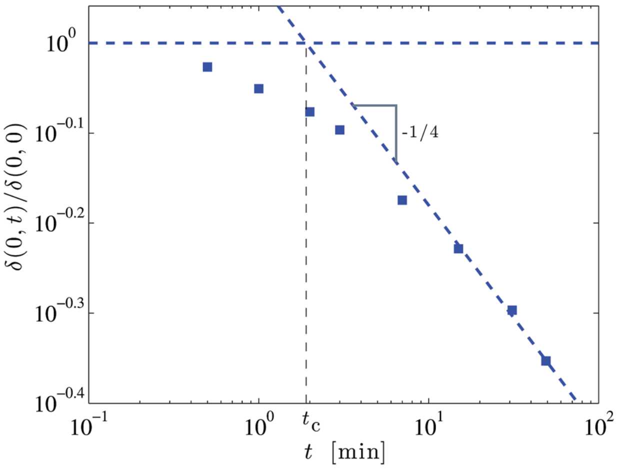

Fig. 4 Central height of the small perturbation shown in Fig. 2(a) and (d) normalized by its initial value as a function of time. The horizontal dashed line represents the initial value. A power law of $t^{1/4}$ is fit to the late time data. In accordance with eqn (10), the convergence time is defined as the intersection of these two regimes, as indicated by the vertical dashed line.

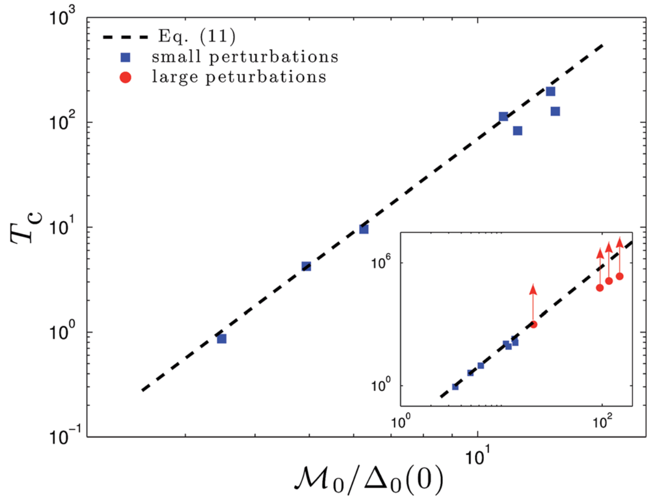

Fig. 5 Non-dimensionalized convergence time as a function of non-dimensionalized width. Here the square data points represent data from small perturbation samples which are in excellent agreement with the dashed black line. The dashed black line is the theoretical prediction of eqn (11). In the inset both the small perturbation results, which have reached the self-similar regime, and the large perturbation data (circles and arrows) which are not yet self-similar are shown.

The theory predicts a very clear dependence of the dimensionless convergence time, T_c, on $M_0/\Delta_0(0)$, a measure of the dimensionless width of the initial profile (see eqn (11)). In Fig. 5 is plotted the dimensionless convergence time obtained as in Fig. 4 as a function of $M_0/\Delta_0(0)$, for seven small perturbations, as well as four large perturbations. For small perturbations, we observe excellent agreement between experiments and the theoretical prediction of eqn (11) with no fitting parameters. We also show the convergence time for the large perturbation data (see the inset of Fig. 5). However, since the large perturbations have not fully reached the intermediate asymptotic regime, the T_c one obtains by forcing a $t^{-1/4}$ power law through the latest data point corresponds to a lower bound. For this reason, the data points provided are shown with vertical arrows.

5 Conclusions

We have studied, both with theory and experiment, the capillary-driven levelling of an arbitrary surface perturbation on a thin liquid film. Using atomic force microscopy and imaging ellipsometry we follow the evolution of the perturbations and compare the results to the theoretical predictions of the two-dimensional capillary-driven thin film equation. We have shown that regardless of the initial condition, the perturbations converge to a universal self-similar attractor that is given by the Green's function of the linear thin film equation. Furthermore, we have shown that the time taken to converge to the attractor depends on the volume of the perturbation. We measured the convergence time for both small and large perturbations and found good agreement between theory and experiment. Specifically, the experimental results are consistent with the theory over two orders of magnitude in the dimensionless typical width of the initial profile and six orders of magnitude in dimensionless convergence time, with no free parameter.

Appendix

We here wish to calculate the integral in eqn (7) in terms of hypergeometric functions. Performing a Taylor expansion of the integrand yields:

$$\phi(U)=\frac{1}{2\pi}\sum_{k=0}^{\infty}\frac{(iU)^k}{k!}\left(\int \mathrm{d}QQ^k\ e^{-Q^4}\right). \tag{12}$$

At this stage one can see that all terms corresponding to an odd $k = 2p + 1$ are null and thus the function f is real. Furthermore, changing the variables through $S = Q^4$ leads to:

$$\phi(U)=\frac{1}{4\pi}\sum_{p=0}^{\infty}\frac{(iU)^{2p}}{(2p)!}\int_0^{\infty}\mathrm{d}SS^{(1+2p)/4-1}\ \mathrm{e}^{-S}, \tag{13}$$

where we recognise a Γ function:

$$\phi(U)=\frac{1}{4\pi}\sum_{p=0}^{\infty}\frac{(iU)^{2p}}{(2p)!}\Gamma\left(\frac{1+2p}{4}\right). \tag{14}$$

Then, separating the sum over p in even $p = 2m$ and odd $p = 2m + 1$ terms yields:

$$\phi(U)=\frac{1}{4\pi}\sum_{m=0}^{\infty}\frac{U^{4m}}{(4m)!}\Gamma\left(m+\frac{1}{4}\right)-\frac{U^2}{4\pi}\sum_{m=0}^{\infty}\frac{U^{4m}}{(4m+2)!}\Gamma\left(m+\frac{3}{4}\right). \tag{15}$$

Developing the Γ function in terms of Pochhammer rising factorials $\Gamma(m + \alpha) = \Gamma(\alpha)(\alpha)_m$ where $(\alpha)_m = \alpha \times (\alpha + 1) \times \ldots \times (\alpha + m - 1)$, and using the relationship $\Gamma(\alpha + 1) = \alpha\Gamma(\alpha)$ yield:

$$\begin{aligned}\phi(U)=&\frac{1}{\pi}\Gamma\left(\frac{5}{4}\right)\sum_{m=0}^{\infty}\frac{U^{4m}}{(4m)!}\left(\frac{1}{4}\right)_m\\&-\frac{U^2}{4\pi}\Gamma\left(\frac{3}{4}\right)\sum_{m=0}^{\infty}\frac{U^{4m}}{(4m+2)!}\left(\frac{3}{4}\right)_m.\end{aligned} \tag{16}$$

Developing the factorials and rising factorials and proving by mathematical induction that:

$$4^{3m}\frac{1\times5\times\ldots\times\left(1+4(m-1)\right)}{4m\times(4m-1)\times\ldots\times1}=\frac{1}{m!}\frac{1}{\left(\frac{1}{2}\right)_m\left(\frac{3}{4}\right)_m}, \tag{17}$$

and that:

$$4^{3m}\frac{3\times7\times\ldots\times\left(3+4(m-1)\right)}{(4m+2)(4m+1)\times\ldots\times1}=\frac{1}{2}\frac{1}{m!}\frac{1}{\left(\frac{3}{2}\right)_m\left(\frac{5}{4}\right)_m}, \tag{18}$$

finally leads to:

$$\begin{aligned}\phi(U)=&\frac{1}{\pi}\Gamma\left(\frac{5}{4}\right){}_0H_2\left[\left\{\frac{1}{2},\frac{3}{4}\right\},\left(\frac{U}{4}\right)^4\right]\\&-\frac{U^2}{8\pi}\Gamma\left(\frac{3}{4}\right){}_0H_2\left[\left\{\frac{5}{4},\frac{3}{2}\right\},\left(\frac{U}{4}\right)^4\right].\end{aligned} \tag{19}$$

where the (0, 2)-hypergeometric function is defined as:[50,51]

$${}_0H_2(\{a,b\},w)=\sum_{m=0}^{\infty}\frac{1}{(a)_m(b)_m}\frac{w^m}{m!}. \tag{20}$$

Acknowledgements

The financial support by the NSERC of Canada and École Normale Supérieure of Paris is gratefully acknowledged. The authors also thank M. Ilton, J. D. McGraw, M. Backholm, O. Bäumchen, and H. A. Stone for fruitful discussions as well as Etienne Raphaël for the cover artwork.

References

1 R. Blossey, *Thin Liquid Films: Dewetting and Polymer Flow*, Springer, 2012.
2 A. Oron, S. Davis and S. Bankoff, *Rev. Mod. Phys.*, 2009, **81**, 1131.
3 R. V. Craster and O. K. Matar, *Rev. Mod. Phys.*, 1997, **69**, 931.
4 J. Teisseire, A. Revaux, M. Foresti and E. Barthel, *Appl. Phys. Lett.*, 2011, **98**, 013106.
5 S. Y. Chou, P. R. Krauss and P. J. Renstrom, *Appl. Phys. Lett.*, 1995, **67**, 3114–3116.
6 J. Ouyang, C.-W. Chu, C. R. Szmanda, L. Ma and Y. Yang, *Nat. Mater.*, 2004, **3**, 918–922.
7 S. Granick and H.-W. Hu, *Langmuir*, 1994, **10**, 3857–3866.
8 J. A. Forrest, K. Dalnoki-Veress and J. R. Dutcher, *Phys. Rev. Lett.*, 1996, **77**, 2002–2005.
9 L. Si, M. V. Massa, K. Dalnoki-Veress, H. R. Brown and R. A. L. Jones, *Phys. Rev. Lett.*, 2005, **94**, 127801.
10 H. Bodiguel and C. Fretigny, *Phys. Rev. Lett.*, 2006, **97**, 266105.
11 K. Shin, S. Obukhov, J.-T. Chen, J. Huh, Y. Hwang, S. Mok, P. Dobriyal, P. Thiyagarajan and T. P. Russell, *Nat. Mater.*, 2007, **6**, 961–965.
12 Z. Fakhraai and J. A. Forrest, *Science*, 2008, **319**, 600–604.
13 D. R. Barbero and U. Steiner, *Phys. Rev. Lett.*, 2009, **102**, 248303.
14 A. Raegen, M. Chowdhury, C. Calers, A. Schmatulla, U. Steiner and G. Reiter, *Phys. Rev. Lett.*, 2010, **105**, 227801.
15 K. R. Thomas, A. Chennevière, G. Reiter and U. Steiner, *Phys. Rev. E: Stat., Nonlinear, Soft Matter Phys.*, 2011, **83**, 021804.
16 R. N. Li, A. Clough, Z. Yang and O. K. C. Tsui, *Macromolecules*, 2012, **45**, 1085–1089.
17 D. J. Srolovitz and S. A. Safran, *J. Appl. Phys.*, 1986, **60**, 255–260.

18 F. Brochard-Wyart and J. Daillant, *Can. J. Phys.*, 1990, **68**, 1084–1088.
19 G. Reiter, *Phys. Rev. Lett.*, 1992, **68**, 75–78.
20 G. Reiter, *Langmuir*, 1993, **9**, 1344–1351.
21 C. Redon, J. B. Brzoska and F. Brochard-Wyart, *Macromolecules*, 1994, **27**, 468–471.
22 F. Brochard-Wyart, P.-G. de Gennes, H. Hervert and C. Redon, *Langmuir*, 1994, **10**, 1566–1572.
23 R. Xie, A. Karim, J. F. Douglas, C. C. Han and R. A. Weiss, *Phys. Rev. Lett.*, 1998, **81**, 1251–1254.
24 R. Seeman, S. Herminghaus and K. Jacobs, *Phys. Rev. Lett.*, 2001, **87**, 196101.
25 C. Neto and K. Jacobs, *Phys. A*, 2004, **339**, 66–71.
26 T. Vilmin and E. Raphaël, *Eur. Phys. J. E*, 2006, **21**, 161–174.
27 O. Bäumchen, R. Fetzer and K. Jacobs, *Phys. Rev. Lett.*, 2009, **103**, 247801.
28 J. H. Snoeijer and J. Eggers, *Phys. Rev. E: Stat., Nonlinear, Soft Matter Phys.*, 2010, **82**, 056314.
29 O. Bäumchen, R. Fetzer, M. Klos, M. Lessel, L. Marquant, H. Hahl and K. Jacobs, *J. Phys.: Condens. Matter*, 2012, **24**, 325102.
30 T. Kerle, Z. Lin, H.-C. Kim and T. P. Russell, *Macromolecules*, 2001, **34**, 3484.
31 E. Buck, K. Petersen, M. Hund, G. Krausch and D. Johannsmann, *Macromolecules*, 2004, **37**, 8647.
32 J. Teisseire, A. Revaux, M. Foresti and E. Barthel, *Appl. Phys. Lett.*, 2011, **98**, 013106.
33 L. Zhu, C. Brian, S. Swallen, P. Straus, M. Ediger and L. Yu, *Phys. Rev. Lett.*, 2011, **106**, 256103.
34 E. Rognin, S. Landis and L. Davoust, *Phys. Rev. E: Stat., Nonlinear, Soft Matter Phys.*, 2011, **84**, 041805.
35 E. Rognin, S. Landis and L. Davoust, *J. Vac. Sci. Technol., B: Nanotechnol. Microelectron.: Mater., Process., Meas., Phenom.*, 2012, **30**, 011602.
36 J. D. McGraw, T. Salez, O. Bäumchen, E. Raphaël and K. Dalnoki-Veress, *Phys. Rev. Lett.*, 2012, **109**, 128303.
37 T. Salez, J. D. McGraw, O. Bäumchen, K. Dalnoki-Veress and E. Raphaël, *Phys. Fluids*, 2012, **24**, 102111.
38 S. Bommer, F. Cartellier, D. Jachalski, Sebastian andPeschka, R. Seemann and B. Wagner, *Eur. Phys. J. E*, 2013, **36**, 87.
39 O. Bäumchen, M. Benzaquen, T. Salez, J. D. McGraw, M. Backholm, P. Fowler, E. Raphaël and K. Dalnoki-Veress, *Phys. Rev. E: Stat., Nonlinear, Soft Matter Phys.*, 2013, **88**, 035001.
40 M. Backholm, M. Benzaquen, T. Salez, E. Raphaël and K. Dalnoki-Veress, *Soft Matter*, 2014, **10**, 2550.
41 Y. Chai, T. Salez, J. D. McGraw, M. Benzaquen, K. Dalnoki-Veress, E. Raphaël and J. A. Forrest, *Science*, 2014, **343**, 994–999.
42 M. Rauscher, A. Münch, B. Wagner and R. Blossey, *Eur. Phys. J. E*, 2005, **17**, 373.
43 A. Münch, B. Wagner, M. Rauscher and R. Blossey, *Eur. Phys. J. E*, 2006, **20**, 365.
44 M. Benzaquen, T. Salez and E. Raphaël, *Europhys. Lett.*, 2014, **106**, 36003.
45 M. Bowen and T. P. Witelski, *SIAM J. Appl. Math.*, 2006, **66**, 1727.
46 T. G. Myers, *SIAM Rev.*, 1998, **40**, 441.
47 M. Benzaquen, T. Salez and E. Raphaël, *Eur. Phys. J. E*, 2013, **36**, 82.
48 A. Bertozzi, *Notices of the AMS*, 1998, **45**, 689.
49 G. I. Barenblatt, *Scaling, self-similarity, and intermediate asymptotics*, Cambridge University Press, Cambridge, 1996.
50 M. Abramowitz and I. Stegun, *Handbook of mathematical functions*, Dover Publications, Mineola, 1965.
51 I. S. Gradshteyn and I. M. Ryzhik, *Table of integrals, series,and products*, Academic Press, Salt Lake City, 1965.

Summary of paper 3

Relaxation and intermediate asymptotics of a rectangular trench in a viscous film
Oliver Bäumchen, Michael Benzaquen, Thomas Salez, Joshua D. McGraw, Matilda Backholm, Paul Fowler, Elie Raphaël, and Kari Dalnoki-Veress, Physical Review E, **88**, 035001 (2013).

This paper is also a study on capillary driven flows. In this work we follow the evolution of a trench geometry. As we anneal above T_g the trench fills in to the minimize surface area of the system. In the initial stages, the two edges of the trench are separated and do not interact with one another. At later times the two edges begin to interact and we observe faster levelling dynamics. By considering the boundary conditions for each of these two regimes we are able to understand this change in levelling dynamics. We observe excellent agreement between experiment and the theory developed from the thin film equation. As was the case in the work of Paper 1, we find that the surface profiles converge to the universal self similar attractor.

For this work, I was primarily involved in developing the sample preparation techniques in collaboration with O. Bäumchen and my supervisor. In the initial stages of this work, I prepared samples and performed experiments to test the project's feasibility. All experiments presented in the paper were performed by O. Bäumchen and M. Backholm. Additionally, I wrote the MATLAB scripts used to analyze the data, starting from code originally written by J. McGraw. M. Benzaquen and T. Salez developed the theory presented in this work in collaboration with their supervisor E. Raphaël. O. Bäumchen wrote the first draft of the paper. I prepared the figures which appear in the appear paper and was involved in the writing of later versions of the manuscript.

PHYSICAL REVIEW E **88**, 035001 (2013)

Relaxation and intermediate asymptotics of a rectangular trench in a viscous film

Oliver Bäumchen,[1,*] Michael Benzaquen,[2,*] Thomas Salez,[2] Joshua D. McGraw,[1,†] Matilda Backholm,[1] Paul Fowler,[1]
Elie Raphaël,[2] and Kari Dalnoki-Veress[1,2,‡]
[1]*Department of Physics and Astronomy and the Brockhouse Institute for Materials Research, McMaster University, Hamilton, Canada*
[2]*Laboratoire de Physico-Chimie Théorique, UMR CNRS Gulliver 7083, ESPCI, Paris, France*

(Received 24 June 2013; published 13 September 2013)

The surface of a thin liquid film with nonconstant curvature flattens as a result of capillary forces. While this leveling is driven by *local* curvature gradients, the *global* boundary conditions greatly influence the dynamics. Here, we study the evolution of rectangular trenches in a polystyrene nanofilm. Initially, when the two sides of a trench are well separated, the asymmetric boundary condition given by the step height controls the dynamics. In this case, the evolution results from the leveling of two noninteracting steps. As the steps broaden further and start to interact, the global symmetric boundary condition alters the leveling dynamics. We report on full agreement between theory and experiments for the capillary-driven flow and resulting time dependent height profiles, a crossover in the power-law dependence of the viscous energy dissipation as a function of time as the trench evolution transitions from two noninteracting to interacting steps, and the convergence of the profiles to a universal self-similar attractor that is given by the Green's function of the linear operator describing the dimensionless linearized thin film equation.

DOI: 10.1103/PhysRevE.88.035001 PACS number(s): 47.15.gm, 47.55.nb, 47.85.mf, 83.80.Sg

Thin films are prevalent in applications such as lubricants, coatings for optical and electronic devices, and nanolithography to name just a few. However, it is also known that the mobility of polymers can be altered in thin films [1–5]. Thus, understanding the dynamics of thin films in their liquid state is essential to gaining control of pattern formation and relaxation on the nanoscale [6,7]. For example, high-density data storage in thin polymer films is possible by locally modifying a surface with a large two-dimensional array of atomic force microscope probes [8]. This application relies on control of the time scales of the flow created by a surface profile to produce or erase a given surface pattern. In contrast to this technologically spectacular example is the surface of freshly applied paint, which relies on the dynamics of leveling to provide a lustrous surface.

Much has been learned about the physics of thin films from dewetting, where an initially flat film exposes the substrate surface to reduce the free energy of the system [9–18]. Other approaches, for example studying the evolution of surface profiles originating from capillary waves [19], embedding of nanoparticles [5], or those created by an external electric field [20,21], have also been utilized to explore mobility in thin films. Although the capillary-driven leveling of a nonflat surface topography in a thin liquid film has been reported in various studies [22,23], experiments with high resolution compared to a general theory that relates time scales to spatial geometries and properties of the liquid are still lacking. Recently, we studied the leveling of a *stepped film*: a new nanofluidic tool to study the properties of polymers in thin film geometries [24–28].

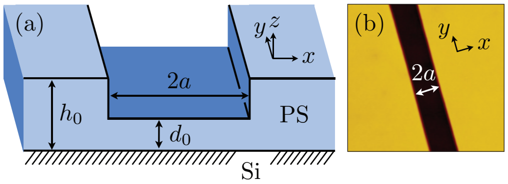

FIG. 1. (Color online) (a) Schematic of the initial geometry of a polystyrene film on a silicon wafer (not to scale: $2a$ is a few microns, while h_0 and $d_0 \sim 100$ nm). (b) Atomic force microscopy image of a typical trench (image width 30 μm, height range 115 nm).

In this work, we study the leveling of perfect *trenches* in thin liquid polymer films as shown in Fig. 1. A trench is composed of two opposing steps separated by a distance $2a$. This structure evolves because of gradients in the Laplace pressure resulting from gradients in the curvature. Initially, the trench levels as two noninteracting steps, with an asymmetric global boundary condition set by the height h_0 of the film at the top of the step and the height d_0 of the film at the bottom of the step. However, as the steps broaden, they interact with one another, which results in an overall symmetric boundary condition, with h_0 on both sides. As will be shown, the crossover from asymmetric to symmetric boundary conditions modifies the scaling law for the energy dissipation in the film. This striking feature reveals the fundamental role played by the boundary conditions in the evolution of global quantities of the system. Furthermore, the trench geometry provides an ideal illustration of the theory of *intermediate asymptotics* [29]: a key tool underlying historical examples such as the Reynolds drag force [30], Kelvin's nuclear explosion [31,32], and scaling theory in general in a situation that is highly relevant for industry and fundamental nanorheology. Intermediate asymptotics theory is based on self-similarity, addresses complex nonlinear partial differential equations, and provides solutions at intermediate times: a time range far enough from the initial state so that details of the initial condition can be forgotten and far enough from the trivial equilibrium state. The value of those intermediate solutions is thus to bring a certain generality by offering an alternative to the principle of superposition, which is lacking in

---

[*] These authors contributed equally to this work.

[†] Present address: Department of Experimental Physics, Saarland University, D-66041 Saarbrücken, Germany.

[‡] dalnoki@mcmaster.ca

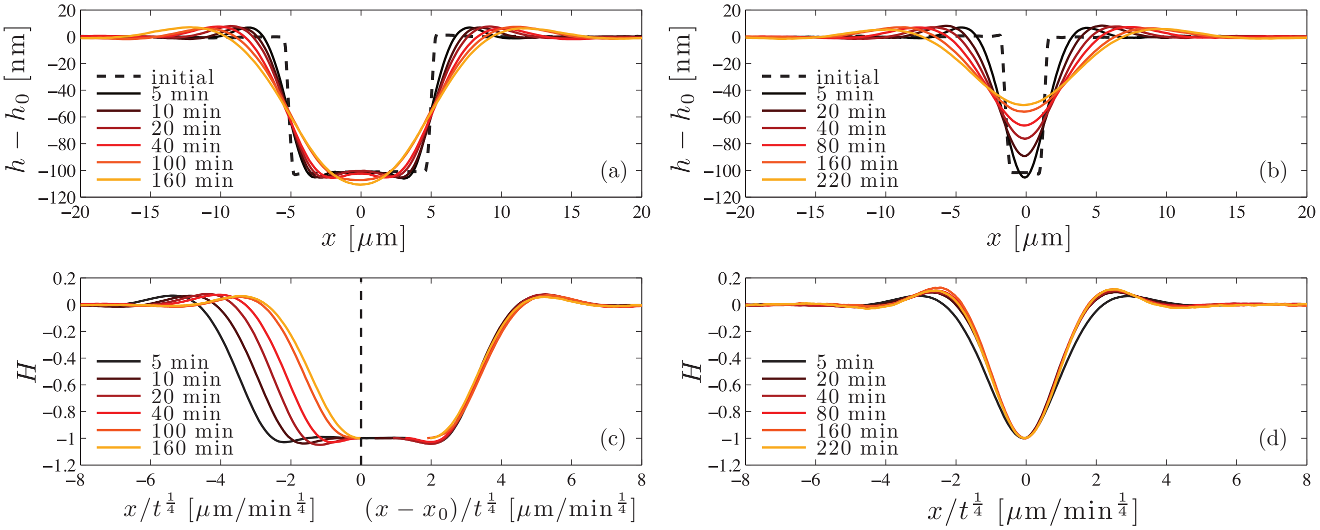

FIG. 2. (Color online) (top) Experimental surface profiles at various times ($5 \leqslant t \leqslant 220$ min). The initial rectangular trenches are shown with dashed lines and exhibit widths of (a) $a = 5.3$ μm and (b) $a = 1.6$ μm. (bottom) The normalized height data of (a) and (b) are rescaled in accordance with the scaling predictions of the theory. The right panel of (c) shows the data shifted to illustrate the collapse of the self-similar profiles, where $x_0(t)$ is a horizontal shift for each right front. Profiles in (a) and (c) show the approach of two noninteracting steps, whereas in (b) and (d) the steps are interacting and the trench depth decreases.

nonlinear physics. In the work presented here, the profile does not evolve self-similarly for early times. However, after some transient period the profile becomes self-similar and converges to a universal attractor that depends on the boundary condition: the intermediate asymptotic solution [33].

Polymer films exhibiting rectangular trench geometries, as illustrated in Fig. 1, were prepared as follows. Polystyrene (PS) films were spin cast from a toluene (Fisher Scientific, Optima grade) solution onto freshly cleaved mica sheets (Ted Pella Inc.). The PS has molecular weight $M_\mathrm{w} = 31.8$ kg/mol with a polydispersity index of 1.06 (Polymer Source Inc.). The samples were annealed in a vacuum oven ($\sim 10^{-5}$ mbar) for 24 h at 130 °C. This temperature is well above the glass transition temperature ($T_\mathrm{g} \approx 100\,^\circ$C) and ensures removal of residual solvent and relaxation of the polymer chains. Films were then floated onto the surface of ultrapure water (18.2 MΩ cm, Pall, Cascada LS) and picked up with 1 cm × 1 cm Si wafers (University Wafer). Si wafers were cleaned by exposure to air plasma (low power, Harrick Plasma, for 30 s), with subsequent rinses in ultrapure water, methanol (Fisher Scientific, Optima grade), and toluene. After the film was transferred to the Si, the floating transfer was repeated, resulting in a second film with the same thickness on top of the first polymer film. The polymer films are not highly entangled and easily fracture on the surface of the water, resulting in straight float gaps. These float gaps can be hundreds of microns long and only a few microns wide. Thus, the second transfer creates a rectangular trench such that $h_0 = 2d_0$ (see Fig. 1). The edges of the trench were checked with atomic force microscopy (AFM, Veeco Caliber) and optical microscopy to ensure that there were no defects in the trench and the vicinity. We stress that the samples are prepared at room temperature, well below T_g, and only flow when heated above T_g.

In all cases studied, the width of the trench was constant and much smaller than its length. The problem can thus be safely treated as invariant in the y coordinate along the length of the trench. Prior to each measurement, the initial condition was recorded using AFM, as shown in Figs. 2(a) and 2(b): the width of the trench $2a$, as well as the depth $h_0 - d_0$, was determined from an analysis of height profiles. Independently, thicknesses were measured with AFM from float gaps or a small scratch made through the film to the substrate. Samples were annealed in ambient conditions [34] at 140 °C on a hot stage (Linkam) with a heating rate of 90 °C/min. Height profiles $z = h(x,t)$ representing the vertical distance between the substrate-liquid and liquid-air interfaces at position x of the trenches were recorded using AFM after various times t, following a quench to room temperature. Figures 2(a) and 2(b) show the evolution of rectangular trenches for $h_0 = 2d_0 = 206$ nm, with $a = 5.3$ μm and $a = 1.6$ μm, respectively, as a function of the annealing time t. We deliberately used two different initial widths in order to address the two different temporal regimes in a single rescaled description, as detailed below. As can be seen in Fig. 2(a), the profiles broaden and are accompanied by a bump at the top of the step and a dip at the bottom of the step that are characteristic of isolated steps [25]. Initially, both sides of the trench in Fig. 2(a) level independently of each other until $t \sim 100$ min, when both dips merge into a single minimum. The subsequent stage is characterized by the decreasing depth of the profile, as shown in Fig. 2(b), while the profile continues to broaden.

The relaxation process of the surface can be described by considering capillary driving forces originating from the nonconstant curvature of the surface [35]: Gradients in the Laplace pressure $p(x,t)$ provide a driving force for leveling the surface topography. The Laplace pressure is given by $p(x,t) \approx -\gamma \partial_x^2 h$, where γ is the air-liquid surface tension. The height scales in this study were chosen to be small enough that gravitational forces can be neglected [36] but sufficiently large to neglect disjoining forces [37]. Moreover, we can safely exclude phenomena related to the polymer chain size, e.g., confinement effects, as the film thicknesses are much larger than characteristic polymer chain length scales. The time scale of the longest relaxation time of PS (31.8 kg/mol) at 140 °C is orders of magnitude shorter than the time scales considered here [38]; thus, we can treat the film as a simple Newtonian liquid. The theoretical description of the problem is thus based on the Stokes equation for highly viscous flows and the lubrication approximation, which states that all vertical length scales are small compared to horizontal ones [39–42]. A no-slip boundary condition at the liquid-substrate interface and the no-stress boundary condition at the liquid-air interface result in the familiar Poiseuille flow along the z axis. Invoking conservation of volume leads to the capillary-driven thin film equation (TFE):

$$\partial_t h + \frac{\gamma}{3\eta}\partial_x\left(h^3\partial_x^3 h\right) = 0, \tag{1}$$

where η is the viscosity of the film [39–41]. The ratio γ/η provides the typical speed of leveling and is termed the *capillary velocity*. Equation (1) is highly nonlinear and has no known general analytical solution. Nevertheless, it can be solved numerically using a finite difference algorithm [27,43]. Equation (1) can also be linearized and solved analytically in the particular situation where the trench is a perturbation: $h_0 \approx d_0$ [26,33]. In this linear case, we recently showed that the solutions converge to a self-similar attractor [33]:

$$h(x,t) \xrightarrow[t\to\infty]{} h_0 + 2\,(d_0 - h_0)\,\mathcal{G}(U,T), \tag{2}$$

where we introduced the two dimensionless variables

$$U = \frac{x}{t^{1/4}}\left(\frac{3\eta}{\gamma h_0^3}\right)^{1/4}, \tag{3}$$

$$T = \frac{\gamma h_0^3 t}{3\eta a^4}\,, \tag{4}$$

as well as the Green's function of the linear operator describing the dimensionless linearized thin film equation,

$$\mathcal{G}(U,T) = \frac{1}{2\pi T^{1/4}}\int_{-\infty}^{\infty} dQ e^{-Q^4} e^{iQU}\,. \tag{5}$$

Thus, the experimental profiles should collapse at long times when the vertical axis is normalized by the depth of the trench, $H = [h(x,t) - h_0]/[h_0 - h(0,t)]$, and the horizontal axis is rescaled as $x/t^{1/4}$. We checked numerically that this statement is still true in the nonlinear case of Eq. (1) [33]. The self-similar regime represents the intermediate asymptotics solution of this thin film problem [29].

We first consider the nonlinear situation, where $h_0 = 2d_0$. In Figs. 2(c) and 2(d) we show the rescaled data corresponding to the noninteracting [Fig. 2(a)] and interacting [Fig. 2(b)] regimes of the trench evolution. Excellent agreement with the theoretical predictions is obtained. The noninteracting steps all have the same profile in their frame of reference. This is demonstrated by shifting the data as shown on the right side of Fig. 2(c), where $x_0(t)$ is a horizontal shift for each right front. At long times, self-similarity in $x/t^{1/4}$ is obtained for the interacting steps. Thus, there are two distinct regimes: first, an initial stage where the steps broaden and are self-similar in their frame of reference but are not yet interacting and, second, a crossover to a final self-similar stage where the steps have merged and the depth of the profile diminishes. These two distinct stages correspond to the crossover of the system from the asymmetric boundary condition of the noninteracting steps to the symmetric global boundary condition of the profile. As discussed, it is possible to numerically solve Eq. (1) for the trench geometry [27,43]. The experimental data are in excellent agreement with nonlinear calculations as shown in Fig. 3(a) for $t = 80$ min. We note that this agreement is typical and is obtained for all such comparisons. In the self-similar representation of the data, only a lateral stretch is required to match the experimental data and the calculation. According to Eq. (1), the stretching factor is directly related to the capillary velocity, and we obtain $\eta/\gamma = 0.034$ min/μm for PS (31.8 kg/mol) at 140 °C. This value is in excellent agreement with literature values [28,44] and is consistent with the capillary velocity that can be determined from the noninteracting steps according to the technique described in [25].

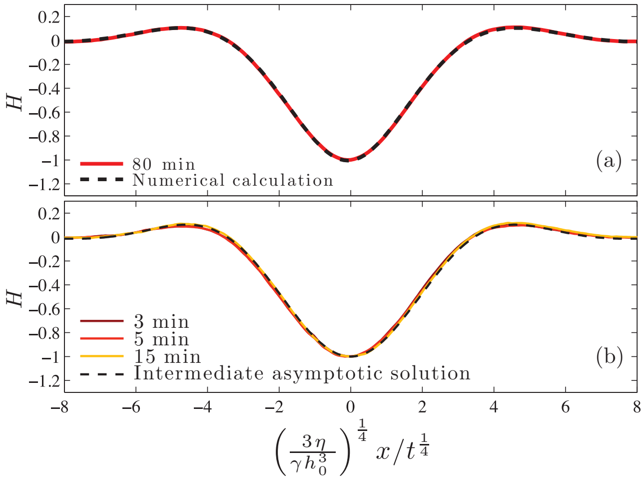

FIG. 3. (Color online) Normalized height profiles for experiments (solid line) annealed at 140 °C and best-fit theory (dashed lines). (a) A trench with $a = 1.6$ μm, $h_0 = 206$ nm, $d_0 = 103$ nm after annealing for $t = 80$ min, with a corresponding numerical solution to Eq. (1). (b) A trench where the depth is a small perturbation ($a = 2.5$ μm, $h_0 = 611$ nm, $d_0 = 59$ nm) at 140 °C. The dashed line is the analytical Green's function of the linear operator describing the linearized thin film equation.

With the theoretical tools described above, we are able to analyze the *entire* evolution from noninteracting to interacting steps. A relevant quantity that can be extracted from the data is the excess contour length $\Delta\mathcal{L}$ as a function of time. For small slopes, one has

$$\Delta\mathcal{L} \approx \int dx \frac{1}{2}(\partial_x h)^2. \tag{6}$$

From the specific dimensional invariance of Eq. (1), one can show that

$$\frac{a\Delta\mathcal{L}}{h_0^2} = \left(\frac{\gamma h_0^3 t}{3\eta a^4}\right)^{-1/4} f\left(\frac{\gamma h_0^3 t}{3\eta a^4}, \frac{h_0 - d_0}{h_0}\right), \tag{7}$$

where f is a function of two variables. This intrinsic similarity comes from the fact that any initial profile $h_\lambda(\lambda x,0) = h(x,0)$

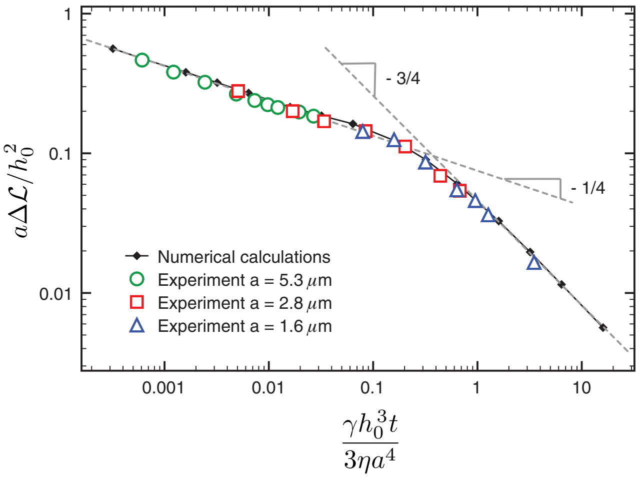

FIG. 4. (Color online) Excess contour length $\Delta\mathcal{L}$ of rectangular trenches (half width a, reference film height h_0) in a nondimensionalized representation as a function of the nondimensionalized time. Experimental data (open circles, rectangles, and triangles) and nonlinear numerical calculations (solid circles) both show a transition from a $-1/4$ to a $-3/4$ power-law scaling. Experimental error bars are less than 2% of reported values.

obtained from a horizontal stretch of factor λ yields the evolution $h_\lambda(\lambda x, \lambda^4 t) = h(x,t)$ through Eq. (1). Thus, the excess contour length evolution of trenches with the same vertical aspect ratio, $h_0/d_0 = 2$, but with different widths can be rescaled in a single master plot as shown in Fig. 4. In accordance with the theory, our experiments demonstrate a $\Delta\mathcal{L} \sim t^{-1/4}$ scaling regime for early times which corresponds to two independent relaxing steps [25]. Afterwards, the two steps interfere, and there is a crossover to a long-time $\Delta\mathcal{L} \sim t^{-3/4}$ scaling regime. This observation can be understood by combining Eqs. (2) and (6). Having done so, we obtain

$$\frac{a\Delta\mathcal{L}}{h_0^2} \underset{t\to\infty}{\longrightarrow} \frac{\Gamma(3/4)}{2^{7/4}\pi}\left(\frac{\gamma h_0^3 t}{3\eta a^4}\right)^{-3/4}\left(\frac{h_0 - d_0}{h_0}\right)^2, \tag{8}$$

which is valid in the linear case. The numerical calculations shown in Fig. 4 confirm this asymptotic $\Delta\mathcal{L} \sim t^{-3/4}$ scaling in the nonlinear case as well. This is expected since any profile will eventually become a perturbation at long times. The comparison of the data for three trenches with different widths and the numerical calculations shown in Fig. 4 clearly validates the theoretical predictions.

Finally, in order to study the intermediate asymptotics in more detail, we realized experimentally the linear case of a small surface perturbation: $h_0 \approx d_0$. This geometry evolves faster towards the intermediate asymptotic regime, and a full analytic solution was obtained for the linearized thin film equation [33]. The sample was prepared by spin coating a thick PS film directly onto a clean Si wafer, while another, much thinner, PS film was prepared on a freshly cleaved mica sheet. The sample annealing and floating of the top layer to prepare the trenches were done exactly as described for the previous $h_0 = 2d_0$ samples. In Fig. 3(b), we show the self-similar profiles for three different annealing times, as well as the fit of the universal self-similar attractor given by the Green's function of the linearized thin film equation [33]. Excellent agreement is found, with the only free parameter being the ratio $\eta/\gamma = 0.016$ min/μm. This value is again in very good agreement with expected literature values [28,44], demonstrating the validity of the intermediate asymptotics.

To conclude, we provided insights into the relaxation of a trench at the free surface of a viscous film. The surface relaxes due to the nonconstant curvature of the free interfaces which drives flow. We found that the transition from the asymmetric boundary condition of two noninteracting steps to the symmetric boundary condition of the two interacting steps greatly influences the scaling of global properties such as the energy dissipation in the film. Specifically, the excess contour length crosses over from a $-1/4$ power law to a $-3/4$ power law with time in complete accordance with theoretical expectations. The profiles were found to be in quantitative agreement with full numerical resolution of the nonlinear thin film equation. Moreover, we have verified experimentally that a small perturbative trench atop a flat film converges to a universal self-similar attractor that is given by the Green's function of the linear operator describing the linearized thin film equation. Therefore, although relevant to nanolithography, relaxation of a painted surface, and many other industrial processes that do not necessary involve polymers, the simple trench geometry developed here also provides an ideal application of intermediate asymptotics. For a flat symmetric boundary condition, the properly rescaled self-similar attractor is *universal* and should not depend on the initial profile or on the viscous material used.

The authors thank NSERC of Canada, the German Research Foundation (DFG) under Grant No. BA3406/2 and SFB1027, École Normale Supérieure of Paris, Fondation Langlois, and the ESPCI Joliot Chair for financial support.

---

[1] P. A. O'Connell and G. B. McKenna, Science **307**, 1760 (2005).
[2] L. Si, M. V. Massa, K. Dalnoki-Veress, H. R. Brown, and R. A. L. Jones, Phys. Rev. Lett. **94**, 127801 (2005).
[3] H. Bodiguel and C. Fretigny, Phys. Rev. Lett. **97**, 266105 (2006).
[4] K. Shin, S. Obukhov, J.-T. Chen, J. Huh, Y. Hwang, S. Mok, P. Dobriyal, P. Thiyagarajan, and T. Russell, Nat. Mater. **6**, 961 (2007).
[5] Z. Fakhraai and J. A. Forrest, Science **319**, 600 (2008).
[6] T. Leveder, S. Landis, and L. Davoust, Appl. Phys. Lett. **92**, 013107 (2008).
[7] J. Teisseire, A. Revaux, M. Foresti, and E. Barthel, Appl. Phys. Lett. **98**, 013106 (2011).
[8] P. Vettiger, G. Cross, M. Despont, U. Drechsler, U. Dürig, B. Gotsmann, W. Häberle, M. A. Lantz, H. E. Rothuizen, R. Stutz, and G. K. Binnig, IEEE Trans. Nanotechnol. **1**, 39 (2002).
[9] D. J. Srolovitz and S. A. Safran, J. Appl. Phys. **60**, 255 (1986).
[10] F. Brochard Wyart and J. Daillant, Can. J. Phys. **68**, 1084 (1990).
[11] G. Reiter, Phys. Rev. Lett. **68**, 75 (1992).

[12] R. Seemann, S. Herminghaus, and K. Jacobs, Phys. Rev. Lett. **87**, 196101 (2001).

[13] R. Fetzer, K. Jacobs, A. Münch, B. A. Wagner, and T. P. Witelski, Phys. Rev. Lett. **95**, 127801 (2005).

[14] G. Reiter, M. Hamieh, P. Damman, S. Sclavons, S. Gabriele, T. Vilmin, and E. Raphaël, Nat. Mater. **4**, 754 (2005).

[15] T. Vilmin and E. Raphaël, Eur. Phys. J. E **21**, 161 (2006).

[16] O. Bäumchen, R. Fetzer, and K. Jacobs, Phys. Rev. Lett. **103**, 247801 (2009).

[17] J. H. Snoeijer and J. Eggers, Phys. Rev. E **82**, 056314 (2010).

[18] O. Bäumchen, R. Fetzer, M. Klos, M. Lessel, L. Marquant, H. Hähl, and K. Jacobs, J. Phys. Condens. Matter **24**, 325102 (2012).

[19] Z. Yang, Y. Fujii, F. K. Lee, C.-H. Lam, and O. K. C. Tsui, Science **328**, 1676 (2010).

[20] D. R. Barbero and U. Steiner, Phys. Rev. Lett. **102**, 248303 (2009).

[21] F. Closa, F. Ziebert, and E. Raphaël, Phys. Rev. E **83**, 051603 (2011).

[22] E. Rognin, S. Landis, and L. Davoust, Phys. Rev. E **84**, 041805 (2011).

[23] E. Rognin, S. Landis, and L. Davoust, J. Vac. Sci. Technol. B **30**, 011602 (2012).

[24] J. D. McGraw, N. M. Jago, and K. Dalnoki-Veress, Soft Matter **7**, 7832 (2011).

[25] J. D. McGraw, T. Salez, O. Bäumchen, E. Raphaël, and K. Dalnoki-Veress, Phys. Rev. Lett. **109**, 128303 (2012).

[26] T. Salez, J. D. McGraw, O. Bäumchen, K. Dalnoki-Veress, and E. Raphaël, Phys. Fluids **24**, 102111 (2012).

[27] T. Salez, J. D. McGraw, S. L. Cormier, O. Bäumchen, K. Dalnoki-Veress, and E. Raphaël, Eur. Phys. J. E **35**, 114 (2012).

[28] J. D. McGraw, T. Salez, O. Bäumchen, E. Raphaël, and K. Dalnoki-Veress, Soft Matter **9**, 8297 (2013).

[29] G. I. Barenblatt, *Scaling, Self-Similarity, and Intermediate Asymptotics* (Cambridge University Press, Cambridge, 1996).

[30] O. Reynolds, Philos. Trans. R. Soc. London **186** 123 (1895).

[31] G. I. Taylor, Proc. R. Soc. London, Ser. A **201**, 159 (1950).

[32] G. I. Taylor, Proc. R. Soc. London, Ser. A **201**, 175 (1950).

[33] M. Benzaquen, T. Salez, and E. Raphaël, Eur. Phys. J. E **36**, 82 (2013).

[34] We have previously verified that for these experiments there is no difference in annealing in an ambient or inert environment.

[35] P.-G. de Gennes, F. Brochard-Wyart, and D. Quéré, *Capillarity and Wetting Phenomena: Drops, Bubbles, Pearls, Waves* (Springer, New York, 2003).

[36] H. Huppert, J. Fluid Mech. **121**, 43 (1982).

[37] R. Seemann, S. Herminghaus, and K. Jacobs, Phys. Rev. Lett. **86**, 5534 (2001).

[38] A. Bach, K. Almdal, H. Rasmussen, and O. Hassager, Macromolecules **36**, 5174 (2003).

[39] L. G. Stillwagon and R. Larson, J. Appl. Phys. **63**, 5251 (1988).

[40] A. Oron, S. Davis, and S. Bankoff, Rev. Mod. Phys. **69**, 931 (1997).

[41] R. Craster and O. Matar, Rev. Mod. Phys. **81**, 1131 (2009).

[42] R. Blossey, *Thin Liquid Films* (Springer, Dordrecht, 2012).

[43] A. Bertozzi, Not. Am. Math. Soc. **45**, 689 (1998).

[44] S. Wu, *Polymer Handbook*, Vol. 4 (Wiley-Interscience, New York, 1999).

Summary of paper 4

Relaxation of non-equilibrium entanglement networks in thin polymer films
Joshua D. McGraw, Paul D. Fowler, Melissa L. Ferrari, and Kari Dalnoki-Veress,
European Physical Journal E, **36**, 7 (2013).

This work uses the technique of crazing to probe the entanglement network in two non-equilibrium systems. First we study films prepared by spincoating. Previous work has established that the spincoating process results in films which have non-equilibrium chain conformations. Our crazing experiments suggest that after spincoating, the chains are highly stretched compared to their equilibrium Gaussian conformation. Furthermore, measurements of the craze ratio, $(h_c/h)^2$, as a function of annealing time ($T > T_g$) reveal that the entanglement network equilibrates on a time scale on the order of one bulk reptation time. In a second set of experiments we prepare films with a thickness comparable to the molecular size. At room temperature we stack two such films to create a glassy bilayer film. Since the chains are unable to cross the mid-plane of the bilayer, according to Silberberg's reflection principle there is an entropic cost associated with such an interface. In the melt, this 'entropic interface' heals. Crazing measurements show that it takes less than one bulk reptation time for a bilayer to become indistinguishable from a single film. This result is in agreement with recent molecular dynamics studies on the healing of polymer-polymer interfaces [56].

Under the co-supervision of J. McGraw and my supervisor, I performed all measurements presented in this paper and did all the data analysis. The experiment was designed by J. McGraw in collaboration with my supervisor. In addition, J. McGraw wrote the MATLAB scripts which were used for the analysis and performed preliminary measurements as a proof of concept. M. Ferrari performed a version of the bilayer experiment which led to significant improvements in the experimental design and sample preparation techniques. J. McGraw wrote the first draft of the paper and I was involved in the writing of subsequent versions.

Eur. Phys. J. E (2013) **36**: 7
DOI 10.1140/epje/i2013-13007-2

THE EUROPEAN
PHYSICAL JOURNAL E

Regular Article

Relaxation of non-equilibrium entanglement networks in thin polymer films

Joshua D. McGraw[1], Paul D. Fowler[1], Melissa L. Ferrari[1], and Kari Dalnoki-Veress[1,a]

Department of Physics & Astronomy and the Brockhouse Institute for Materials Research, McMaster University, Hamilton, Canada

Received 11 October 2012 and Received in final form 7 January 2013

Abstract. It is known that polymer films, prepared by spin coating, inherit non-equilibrium configurations which can affect macroscopic film properties. Here we present the results of crazing experiments that support this claim; our measurements indicate that the as-cast chain configurations are strongly stretched as compared to equilibrium Gaussian configurations. The results of our experiments also demonstrate that the entanglement network equilibrates on a time scale comparable to one reptation time. Having established that films can be prepared with an equilibrium entanglement network, we proceed by confining polymers to films in which the thickness is comparable to the molecular size. By stacking two such films, a bilayer is created with a buried entropic interface. Such an interface has no enthalpic cost, only an entropic penalty associated with the restricted configurations of molecules that cannot cross the mid-plane of the bilayer. In the melt, the entropic interface heals as chains from the two layers mix and entangle with one another; crazing measurements allow us to probe the dynamics of two films becoming one. Healing of the entropic interface is found to take less than one bulk reptation time.

1 Introduction

The dynamics of a sufficiently long polymer chain in a melt of like chains will be restricted by topological constraints called entanglements. To a good approximation, each chain in the melt has the configuration of a random walk. Such chains have an "end-to-end" distance —the distance between the ends of the molecule— that scales as the square root of the number of monomers that make up the chain: $R_{\mathrm{ee}} \propto N^{1/2}$. While random walks are not space filling, polymer melts are [1, 2]. The result of this dichotomy is that each melt chain shares its pervaded volume and interacts with many other chains. A fraction of these interactions are entanglements. Though the precise nature of what constitutes an "entanglement" is still unknown, the chains suffer a restricted mobility as a result of these interactions. The collective effect of the entanglements is to create a "tube" in which the molecule is confined [1, 2]. The chain's motion, termed "reptation", is restricted predominantly to directions along the tube. It is well known that these entanglement constraints are largely responsible for many phenomena in polymer physics, such as: high melt viscosity [2, 3] and viscoelasticity [4–6]; enhanced adhesion [7, 8]; glassy failure mechanisms [9–11]; pronounced confinement effects [12, 13]; and alterated hydrodynamic boundary conditions [14, 15].

Since the entanglement network of a polymer melt greatly influences many properties, it is important to make the distinction between equilibrium and non-equilibrium melts. If the chain statistics in a melt are not at equilibrium, then the entanglement network will also be out of equilibrium. As such, measurements of the properties listed above are typically affected. There has been significant interest in non-equilibrium network effects: several studies have investigated the effects of preparation and annealing treatments on the viscosity [16, 17], capillary wave spectra [18], thermal expansion [19] and residual stress [20–26] in polymer films. In these studies, the non-equilibrium structure is inherited from the film casting process. During the preparation of films by casting from solution, polymer chains vitrify at non-zero solvent content. The presence of solvent results in chains that are swollen in comparison to melt conformations. Since the solvent is volatile, most of it leaves the system and the chains are forced into configurations that are not typical of the equilibrium melt. Since the lateral extent of a film does not change during this evaporation process, the structure must compress in the direction normal to the film as solvent leaves —annealing above the glass transition temperature, T_{g}, allows these perturbed networks a chance to evolve towards equilibrium. A schematic of the typical experiment, showing a chain with a "non-equilibrium con-

---

[a] e-mail: `dalnoki@mcmaster.ca`

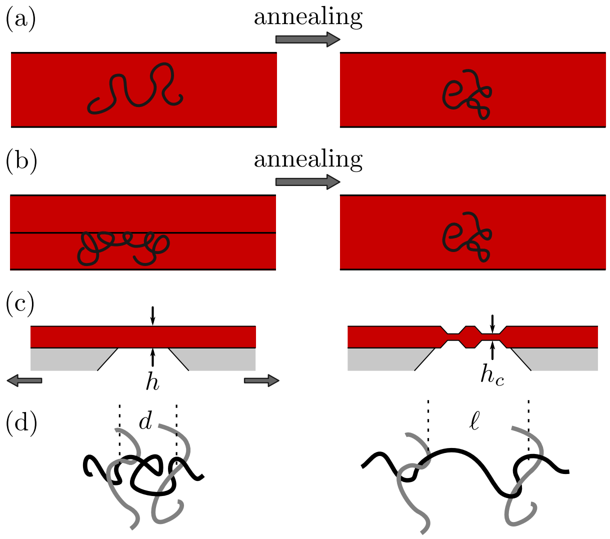

Fig. 1. Schematics of the experiments presented in this work. (a) A chain with a swollen configuration after spin coating. The ensemble of chains recovers equilibrium chain statistics after some period of annealing above T_g. (b) A chain at the “entropic interface” of a bilayer film prepared by stacking two glassy films. Upon annealing above T_g, the Brownian motion of segments allows the entropy-deprived ensemble to relax towards equilibrium. (c) In a crazing experiment, a glassy free standing film with thickness h is strained and necks of material, with thickness h_c are formed. (d) Microscopically, the segments of chains between entanglements have typical size d before straining, and are pulled to a length of ℓ during the crazing experiment.

figuration” being annealed towards an “equilibrium configuration” is seen in fig. 1(a).

The interface of a film also perturbs chain conformations, which results in another method of preparing non-equilibrium samples. Chains at a neutral interface, like a free air or vacuum surface, were described by Silberberg [27]. According to Silberberg’s reflection principle, chains that in the absence of a boundary would cross it are instead reflected back into the melt. These chains are thus unable to explore some conformations resulting in a loss of entropy. The significance of this entropy loss has been discussed in relation to the number of inter-chain entanglements, those between two different chains, that exist near an interface [12]. In [12], Brown and Russell suggest that there is a reduction in the number of inter-chain entanglements near an interface; corresponding measurements support this idea [13,15,28]. In these studies, a distinction is made between inter-chain entanglements and those that occur between two segments far apart on the same chain. In light of the chain packing models [29,30] which define entanglements through the interactions of a test chain with other chains, in [13] it was proposed that inter-chain entanglements and intra-chain entanglements do not contribute equally to the integrity of the network. The topological difference between inter- and intra-chain entanglements was suggested to be responsible for the observed thickness dependence of crazing experiments on thin glassy films [13].

While it is possible for polymer chains in a film to be in equilibrium with a reflective boundary, it is also possible to destroy that equilibrium by stacking two such films. This bilayer film results in a sample with what we will refer to as an “entropic interface” —an interface that has an entropic cost associated with the restricted configurations of the molecules that do not cross the mid-plane of the bilayer. As chain segments undergo Brownian motion when annealed above T_g, entropy is recovered as the chains explore a larger pervaded volume. This experiment is schematically depicted in fig. 1(b).

The literature on chains crossing such entropic interfaces is vast. In particular, early experiments by Klein [31] and others [32–34] were some of the first to put on firm footing the reptation arguments [1,2,35] that have been crucial to understanding the physics of long chain polymer melts. In other experiments, the fracture energy is measured as a function of annealing time between the interfaces [36]. Reptation arguments have been employed to understand these results [7,37,38] and simulations are used to investigate these problems [39]. Up to now, however, direct measurements of the entanglement density across an atomically smooth entropic interface have not been made, in part because we have few experimental probes to quantify this property.

As mentioned above, entangled polymeric materials can fail in a way that is distinct from many other modes of glassy failure. The difference arises from the glass being composed of an entangled polymer network. This failure mode, called crazing [9,10,40,41], is like the ductile failure that occurs in metals in that a drawing stress can produce “necks” of deformed material. However, the crazing process is quite different on a molecular level, as the drawn material has a fibrillar structure in which the polymer chains have configurations that are strongly non-Gaussian. The fibrillar material in a craze is characterized by an extension ratio, λ, defined by the ratio of the craze width, to the width of undeformed material that went into forming the craze. If a thin film with thickness h is crazed, using conservation of volume and assuming that the density of the crazed film and unperturbed film are the same, it can be shown that $\lambda \propto h/h_c$, where h_c is the average thickness of crazed material [13,42–44]. A schematic of the crazing process in a thin film is shown in fig. 1(c).

Donald and Kramer [45,46] proposed that for equilibrated polymer films the extension ratio can be understood by assuming that entanglements act like chemical cross links, which remain fixed throughout the crazing process. While a polymer glass is being crazed, the chain segments between entanglements (entanglement strands), with entanglement molecular weight M_e, are extended such that the distance between entanglements after crazing is $\ell \propto M_e$. Polymer chains undergo random walks down to length scales approaching the monomer size, thus the end-to-end distance of the entanglement strand before crazing was $d \propto M_e^{1/2}$. Since the macroscopic response is a result of the microscopic process, the extension ratio of the craze is the same as that for an average entanglement strand. Therefore, we have $(h_c/h)^2 \propto (d/\ell)^2 \propto 1/M_e$. By recognizing that the density of entanglements is inversely proportional to the mass of a chain segment between entanglements, we have the relation

$$\left(\frac{h_c}{h}\right)^2 \propto \nu_{\text{eff}}, \tag{1}$$

where ν_{eff} is the density of effective entanglements that would be present in a system of equilibrated Gaussian chains. Therefore, by making a measurement of the essentially macroscopic extension ratio, we directly gain information about the microscopic entanglement network. This model was verified by Donald and Kramer [45,46] in experiments, was observed in molecular dynamics simulations by Rottler and Robbins [40,41], and has since been used in many other experiments [10,13,44,47].

In this work, we take advantage of the fact that measuring the craze extension ratio provides information about the entanglement network [13,44] to gain insight into the equilibration process of two non-equilibrium polymer entanglement networks. In the first case, we examine the dependence of the measured $(h_c/h)^2$ on the temperature and subsequent annealing time. After learning how to equilibrate an entanglement network, insomuch as the crazing measurement is concerned, we turn to the creation and healing of the entropic interface provided by a bilayer film.

2 Experiment

Polystyrene (PS) with weight averaged molecular weights $M_w = 785$ and 1144 kg/mol and polydispersity indices ≤ 1.07 (Polymer Source, Inc.) were used to prepare the samples; we refer to these as PS(785k) and PS(1144k). Polymer of a given molecular weight was dissolved into toluene (Fisher Scientific, Optima grade) in various weight fractions ($0.5 < \phi < 2.5$ wt%) and spin coated onto freshly cleaved, $30 \times 30\,\text{mm}^2$ mica sheets (Ted Pella, Inc., Hi-Grade, V2). Spin coating was carried out at room temperature in air; however, in order to explore the effects of temperature several films were also prepared with the substrate attached to a temperature controlled spin coater chuck. The chuck, an aluminum plate in intimate contact with the substrate, ranged in temperature from $5 \leq T \leq 40\,^\circ\text{C}$. Since the thermal mass of the mica substrate and PS/toluene solution is small compared with that of the spin coater chuck, we assume that the solution temperature at the onset of spin coating is close to that measured on the chuck. Because the temperature gradients are large due to the evaporative cooling of the solvent, the temperature controlled measurements serve only to vary the initial temperature of spin coating. For all monolayer experiments of the type depicted in fig. 1(a), samples were $105 \pm 10\,\text{nm}$ thick and composed of PS(785k). Note that we use the terminology "monolayer" to describe a sample consisting of a single film, rather than a molecular monolayer; we refer to two such films stacked on top of one another as a "bilayer". For the study of spin coating effects, monolayers were annealed at $130 \pm 1\,^\circ\text{C} > T_g \approx 97\,^\circ\text{C}$ in a home built vacuum oven (pressure $\sim 10^{-5}$ mbar provided by a turbo molecular pump), for times $0 \leq t_m \leq 348\,\text{hr}$. Here and throughout, the subscript "m" refers to monolayer samples.

In order to prepare bilayer films, we first followed the above procedure for monolayer preparation, except that the monolayers were prepared from PS(1144k), were $50 \pm 3\,\text{nm}$ thick, and annealed at $150\,^\circ\text{C}$ for $t_m = 48\,\text{hr}$[1]. We note that this thickness was chosen such that the monolayers, as described in the work of Si and co-workers [13], would show a thickness dependent $(h_c/h)^2$, while a film with twice the monolayer thickness would be in a range for which $(h_c/h)^2$ had saturated. After annealing, a monolayer was floated onto the surface of an ultra pure water bath (18.2 MΩ cm, Pall, Cascada LS) and a second monolayer, still on a mica substrate, was placed onto the floating monolayer with the polymer-side down, thus creating a PS bilayer[2]. After preparation, the bilayers were annealed for periods $0.5 \leq t_b \leq 90\,\text{hr}$ at $130\,^\circ\text{C}$ (subscript "b" refers to bilayers) in vacuum ovens or on a microscope hot stage (Linkam) in air. The temperature is always known to within $1\,^\circ\text{C}$.

With mono- and bilayers prepared, $\sim 9 \times 9\,\text{mm}^2$ sections of the films were floated onto the surface of an ultra clean water bath and were picked up using a set of two polished and sharp aluminum blocks. The blocks had a fixed gap of $l = 1.5\,\text{mm}$ between the two sharp edges. After drying, one of the blocks was held in place while the other was attached to a translation stage (Newport MFA-CC, SMC100CC). The blocks were then unfixed and the film was deformed with a strain rate of $\dot{\Delta l}/l = 2 \times 10^{-4}\,\text{s}^{-1}$ until crazes were visible under an optical microscope, see fig. 1(c). The samples were typically strained to $\Delta l/l = 0.1$, which resulted in a film with both crazed and undeformed material. Typical craze widths were $\sim 10\,\mu\text{m}$.

Crazed PS films ($\sim 1.5 \times 9\,\text{mm}^2$) were placed onto $10 \times 10\,\text{mm}^2$ Si wafers. Surface forces pull the crazed film that bridges the aluminum gap into contact with the wafer, thereby transferring the delicate sample to the robust Si surface [13,44]. Scratches were put into the film using a scalpel blade. By measuring an appropriate spot along the edge of a scratch, we are able to simultaneously measure the undeformed film height, h, and the height of the craze, h_c relative to the Si substrate surface. An example of such a measurement is shown in fig. 2.

---

[1] As will become clear below, this time is sufficient to ensure an equilibrium entanglement network within the resolution of our experiment

[2] One particular advantage of doing these experiments with spin-coated monolayers is that the surfaces have a highly uniform topography (rms roughness $\sim 0.3\,\text{nm}$ as measured with AFM), ensuring intimate contact between the interfaces. A second advantage of this approach is the fact that we prepare an entropic interface while ensuring that the chains at that interface will not have suffered chain scission. Thus, we can assume a monodisperse chain length distribution at the interface.

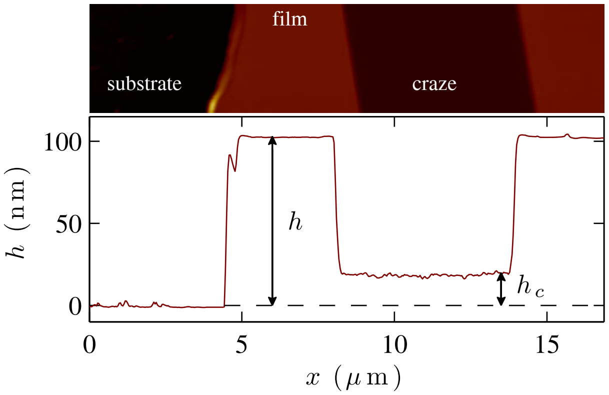

Fig. 2. Height as a function of position from an AFM experiment for a typical crazed thin film after transfer to a Si substrate. From data sets such as these, the film height h, and the craze height h_c are easily determined.

3 Results and discussion

This section is broken into two parts. First, we describe the results of experiments on simple monolayer PS films as shown in fig. 1(a): both the state of as-cast films, and the evolution of these films towards equilibrium will be discussed. We establish that, with extensive annealing above T_g, films may be prepared such that they display the same entanglement density as that of the bulk. Then, we discuss our results on bilayer films with a buried entropic interface, as shown schematically in fig. 1(b).

3.1 Monolayers

3.1.1 As-cast films

In fig. 3(a) is shown a plot of the measured ratio $(h_c/h)^2$ as a function of the temperature of the spin coater chuck on which films were prepared. Additionally, the inset of fig. 3(a) shows the data obtained at $T = 20\,°\mathrm{C}$ in the main figure. For each trial number, data is grouped according to preparation under a given set of experimental conditions. The data in the inset was obtained at room temperature using various initial solution concentrations, while adjusting the spin speed to ensure constant resultant thickness. Additionally, we varied the toluene solvent content in the atmosphere during spin coating. It is clear from the inset that there is considerable scatter in the resulting $(h_c/h)^2$.

In fig. 3(b) are shown two histograms of $(h_c/h)^2$ for films prepared on a spin coater chuck at $T = 5$ and $30\,°\mathrm{C}$; N is the number of measurements of the type shown in the plot of fig. 2. Each data point in figs. 3, 4 and 5 is the mean value of such a distribution: in figs. 3 and 4, the distance from the bottom to the top of an error bar is one standard deviation of the distribution. As such, the reported error in these figures indicates the range of expected values one might obtain from an experimental measurement of $(h_c/h)^2$.

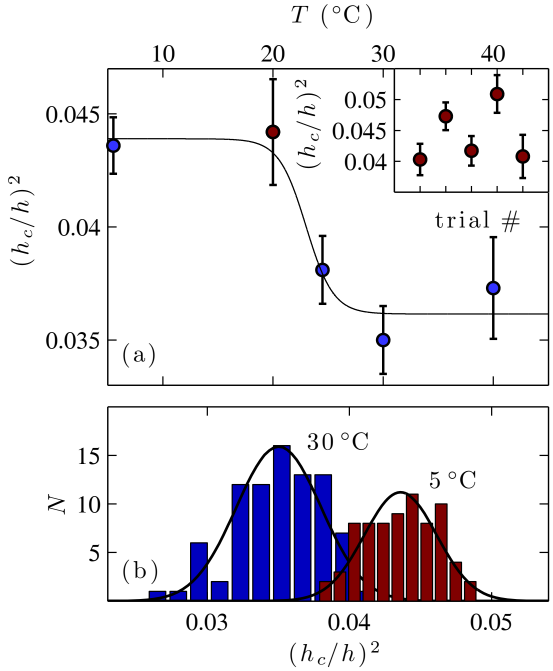

Fig. 3. (a) Plot of $(h_c/h)^2$ for PS(785k) films with thickness 105 ± 10 nm as a function of the temperature of the spin coater chuck on which the films were prepared. The data point in red at $T = 20\,°\mathrm{C}$ is detailed in the inset. There, data from films prepared at room temperature under different casting conditions are shown (different solution concentrations and atmospheric solvent content). The solid black line is a guide for the eye. (b) Histograms for a number of measurements of the type shown in fig. 2. For all data in (a), error bars represent are standard deviations from distributions of the type shown in (b).

The data of fig. 3 indicate that $(h_c/h)^2$ of as-cast films is sensitive to the temperature of the spin coater chuck on which they are prepared. Furthermore, at a given temperature, this quantity is non-trivially dependent on the preparation conditions; even at room temperature the data spread is 20% of the mean value measured at room temperature. Despite our best efforts, we find that there is great variation in the measured values of $(h_c/h)^2$ for films cast with the same initial chuck temperature.

In fig. 4, we see that the values of $(h_c/h)^2$ at $t_m = 0$ (no annealing above T_g) are enhanced as compared to the data at late times. As explained in detail below, chain stretching can account for an enhanced $(h_c/h)^2$ as compared to the measured equilibrium values at long times in fig. 4. Thus, we will now describe two mechanisms by which chains in the as-cast state may become swollen or stretched as compared to their melt equilibrium. We note that while the experimental results provide a robust characterization of the films, the interpretation of the as-cast data is speculative.

The first mechanism we consider results from the fact that chains in the presence of an athermal solvent are swollen in comparison to the melt. The well-established crazing model, described in the introduction, tells us that $(h_c/h)^2 \sim \nu_{\rm eff}$ is valid for equilibrated films because it is based on the Gaussian random statistics of polymer chains: $d \propto M_e^{1/2}$. Clearly, we must take care to interpret the measured values of $(h_c/h)^2$ plotted in figs. 3 and 4 as simply proportional to the entanglement density. More generally, the entanglement segments can have end-to-end distance $d \propto M_e^n$, see fig. 1(d). While for equilibrated polymer films, $n = 1/2$, here we assume $n > 1/2$ since the chain configurations are formed during the spin coating process while still swollen by solvent. After crazing, the segments between entanglements are stretched and we have $\ell \propto M_e$. Following the same logic that precedes eq. (1), we have $h_c/h \propto d/\ell \propto M_e^{n-1}$. Thus, if $n > 1/2$ for swollen chains, then for constant M_e, the measured value of $(h_c/h)^2$ will be larger as compared to an equilibrated system. The enhancement would be due to the fact that swollen chains can be stretched less before having to draw new material into a craze[3].

The second mechanism which can explain an enhanced value of $(h_c/h)^2$ for as-cast films is due to the hydrodynamics of spin coating. During spin coating a polymer solution is deposited onto a substrate at rest. From rest, the substrate is rapidly rotated, producing considerable shear at the substrate-solution interface. As described by Emslie and co-workers several decades ago [48], the height profile of the liquid atop the substrate quickly becomes flat and there is a radial flow that is balanced by a viscous Poiseuille flow in the vertical direction. This flow produces shear both in the plane of and in the direction normal to the substrate. The shear may be large enough for polymer chains to become oriented to the flow. At vitrification, these flow oriented chains would become trapped in configurations that are stretched in comparison to Gaussian chains. This stretching would result in an enhanced value of $(h_c/h)^2$.

In the studies by Steiner and co-workers [16, 17], the apparent viscosity of as-cast polymer films is measured using an electro-hydrodynamic method. Their films, prepared on Si from PS and toluene solutions, showed a decrease in the viscosity of the as-cast state as compared to annealed films. Tsui and co-workers [18] also measure the viscosity of PS films on Si cast from solvents of various quality, ranging from $T \lesssim \Theta$, with Θ the temperature at which chain dimensions are indistinguishable from the melt, to $T > \Theta$ (by contrast, our films are always prepared with $T \gg \Theta$). Using a method of spectral analysis, they find the viscosity of as-cast films to be reduced from its value at long annealing times. All of these results are consistent with a reduced entanglement density in as-cast films, and this idea is often invoked to explain these types of observations. If the interpretation of our results for as-cast films is to be consistent with the reduced entanglement density claimed by others, then it must be that the chain configurations trapped in the as-cast films are stretched beyond that of typical Gaussian chains (either due to swelling by solvent or hydrodynamic shearing effects). Since we measure an enhanced $(h_c/h)^2$ in the as-cast state, it must be that the degree of chain stretching we observe is quite severe. A lower entanglement density with Gaussian statistics would lead to a depressed $(h_c/h)^2$; thus, the stretching and swelling must be enough to dominate this effect. Support for this chain stretching idea can be found in the systematic studies of the pre-stress in spin-coated polymer films [20–24]. Specifically, Reiter and co-workers [19,22,23,26] have used dewetting to probe the behaviour of as-cast films. They observe that the radius of a dewetting hole is larger for an as-cast film when compared to a hole grown for an identical period in a film aged below T_g. In these works, the idea of molecular chain stretching is precisely the supposed origin of the studied pre-stress.

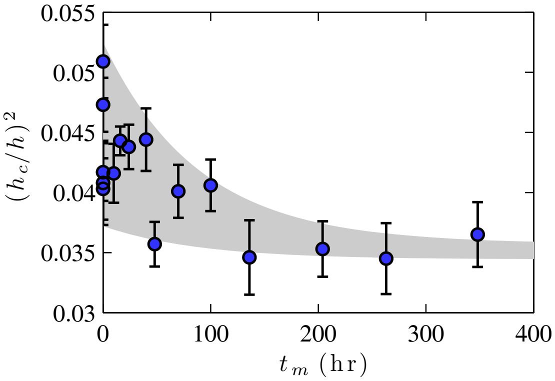

Fig. 4. $(h_c/h)^2$ for PS(785k) monolayers with thickness 105 ± 10 nm spin cast and annealed for times t_m at 130 °C. Since the non-equilibrium state at $t_m = 0$ could not be well controlled, there are a range of values reported. We expect a measurement at subsequent annealing times to be found anywhere within the shaded region.

We now turn to the dependence of $(h_c/h)^2$ on the temperature of the spin coating chuck. The temperature range shown in fig. 3 is high enough so that the PS chain statistics in toluene can be considered as athermal; that is, the average size of an isolated chain in solution does not vary significantly with temperature. Therefore, with this solvent we cannot attribute the observed temperature dependence of $(h_c/h)^2$ to changes in the solvent quality of the film preparation. The solvent quality was claimed as the dominant effect responsible for some of the rheological behaviour seen in previous studies [18, 19, 23]. During the spin coating process, solvent continuously evaporates and the sample vitrifies at a non-zero solvent content. At a lower initial chuck temperature, the sample vitrifies with a higher solvent concentration than at a higher initial temperature. Therefore, without considering the highly violent, non-equilibrium process of spin coating, the chains in films prepared at lower temperatures are necessarily more swollen than their counterparts prepared at higher temperatures. As discussed above, crazing a sample in which the chains were trapped in pre-stretched configurations may account for the general trend of higher $(h_c/h)^2$ observed at lower temperatures in fig. 3.

---

[3] In [42,43], it is shown that crazes grow in width by continuously drawing new material from the undeformed film and maximally stretching this new material, before drawing in more.

To summarize our results on the as-cast monolayer films, we find that the measured value of $(h_c/h)^2$ is enhanced in an as-cast film as compared to a film annealed above T_g for long times (see fig. 4). We propose that the enhancement is due to pre-stretching of the chains during the spin coating process that may occur because of solvent swelling or hydrodynamic shearing. Lastly, the initial temperature at which spin coating proceeds greatly affects the nature of entanglements in as-cast films, even for films prepared from an athermal solvent.

3.1.2 Temporal evolution of as-cast films towards equilibrium

Given the sensitive temperature and environmental dependence of the as-cast extension ratio, the as-cast chain configurations cannot represent those of the equilibrium melt. As such, high-temperature annealing, with $T > T_g$, is expected to result in an evolution towards the equilibrium melt chain statistics. Following a quench to room temperature after an annealing treatment, we would expect to observe differences in $(h_c/h)^2$. In fig. 4 are shown the results of experiments, using PS(785k), for which films were annealed for various times, t_m, before crazing. The data in the inset of fig. 3(a) is shown at $t_m = 0$. As described above, it can be seen that the as-cast state has a larger $(h_c/h)^2$ than for longer annealing times. The data plateaus on a time scale $\tau_m \approx 80$ hr. To extract this time scale, we have performed a best fit to all the data using an exponential function: $(h_c/h)^2 = A_m + B_m e^{-t_m/\tau_m}$. The best fit parameters were $A_m = 0.035$, $B_m = 0.010$ and $\tau_m = 80$ hr.

From the data at $t_m = 0$ in fig. 4, we can see that our preparation under standard laboratory conditions yields a spread of measured $(h_c/h)^2$. However, independent of the preparation, thermal annealing brings all samples toward the same equilibrium state. Within the error of our experiment, all values of $(h_c/h)^2$ after $t_m = 100$ hr are the same. The longest relaxation time of a polymer melt is the reptation time, τ_{rep}, which represents the typical time taken for a molecule in the bulk to lose memory of all previous strains [2]. For PS(785k) at 130 °C, the reptation time is approximately 35 hr [49]. Thus we conclude that the out-of-equilibrium network of the as-cast films relaxes on a time scale ($\tau_m = 80$ hr) that is on the order of one reptation time ($\tau_{rep} \sim 35$ hr).

In the work by Steiner and co-workers [16, 17] as well as Tsui and co-workers [18] described above, the viscosity is probed. In these cases, the time constants for the evolution of the viscosity towards equilibrium is found to be between two and five orders of magnitude longer than the bulk reptation time. These measurements are in stark contrast to the crazing results presented here. As a possible explanation for the discrepancy, we note that in the measurements of Steiner and coworkers, the film surface is perturbed by only ~ 5 nm —a distance that is similar to the distance between entanglement points, or tube-diameter, of PS [29]. Similarly, in the experiments of Tsui and co-workers, it is the capillary wave spectra that are measured, and variations in the height of the samples in the sub-nanometre regime are typical. In addition, the capillary wave measurements are carried out on 14 nm thick samples, which may already be thin enough to observe confinement effects. Thirdly, Napolitano and Wübbenhorst [50] observe that changes in the dielectric response of thin PS films on aluminum substrates take up to 3 orders of magnitude longer than the bulk reptation time. Their results are attributed to the formation of an adsorbed polymer layer that is between 4 and 8 nm thick. By contrast, in the crazing measurement the entire film of ~ 100 nm thickness is probed —crazing reports a "bulk" film property. It is then possible that the origin of the significant discrepancy in relaxation time scales is the result of a subtle and interesting effect which is particular to the interfacial regions of the polymer films studied in [16–18, 50].

3.2 Bilayers

In the previous section, we discussed that as-cast films are characterized by a non-equilibrium entanglement network. Furthermore, we established that the as-cast films can be equilibrated on time scales comparable to the longest relaxation time of the polymer. We now turn to the results observed in another non-equilibrium entanglement network: bilayer films with a buried entropic interface, as shown schematically in fig. 1(b).

As discussed in the introduction, chains at an interface are subject to the Silberberg reflection principle [1, 12, 27], which states that chain segments that would have crossed the interface are instead reflected back into the polymer melt. These chains thus share their pervaded volumes with fewer other chains, compared to chains in the bulk (see p. 61 in [1]). The influence of the reflection principle on the measurement of $(h_c/h)^2$ was exploited by Si and co-workers [13]. It was found that a film whose thickness is similar to the unperturbed coil radius has a lower $(h_c/h)^2$. The results were interpreted as being due to a reduced inter-chain entanglement density at an interface, similar to ideas first proposed by Brown and Russell [12].

In our experiments, the monolayers used to prepare the bilayers were thin enough to have $(h_c/h)^2$ values that are markedly different from the thick film regime as measured by Si and co-workers [13]; while the end-to-end distance of PS(1144k) is approximately 70 nm [51], the bilayers were made from two films with $h \approx 50$ nm. These monolayers were annealed as described in the experimental section, with annealing times $t_m > 10\,\tau_{rep}$ [49]. Given the results of fig. 4, we assume that the resulting monolayers had chain statistics described by the equilibrium value corresponding to the confined films. We stress that the thickness of the monolayers was chosen specifically: the monolayers are thin enough such that they exhibit a reduced effective entanglement density, while a film thickness corresponding to twice that thickness has a bulk-like entanglement density according to the work by Si and co-workers [13]. Thus, a bilayer film will show a reduced $(h_c/h)^2$ which approaches the bulk value upon annealing.

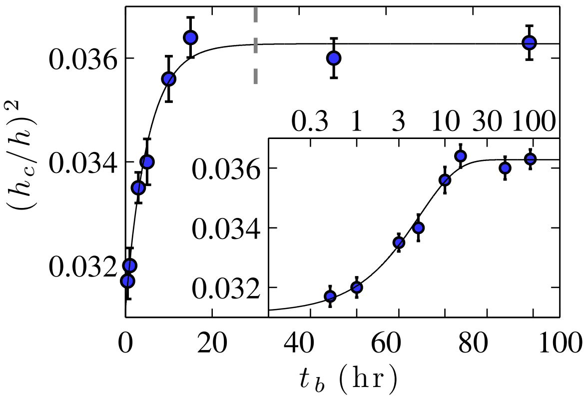

Fig. 5. $(h_{\rm c}/h)^2$ as a function of annealing time, $t_{\rm b}$ at 130 °C, for PS(1144k) bilayer samples prepared by stacking two monolayer films with thickness 50 ± 3 nm. The error bars in this figure are the standard error of the mean, rather than the standard deviation as reported in figs. 3(a) and 4. The vertical dashed line indicates $\tau_{\rm rep}/4$. To emphasize the data at early times and the agreement with an exponential relaxation, the inset shows the same data as in the main figure, except with a logarithmic time axis.

In fig. 5 are shown the results of measurements on bilayer films annealed for times $t_{\rm b}$ at $T = 130\,^\circ$C, well above $T_{\rm g}$. The errors reported are the standard error of the mean as taken from distributions similar to those in fig. 3(b). The data in fig. 5 is well described by an exponential: $(h_{\rm c}/h)^2 = A_{\rm b} - B_{\rm b} e^{-t_{\rm b}/\tau_{\rm b}}$. The best fit to the data corresponds to $A_{\rm b} = 0.0363$, $B_{\rm b} = 0.0051$ and $\tau_{\rm b} = 5.1$ hr. Given that the reptation time of PS(1144k) at 130 °C is approximately equal to 120 hr, we find that the relaxation across the entropic interface is achieved much faster than one bulk reptation time. Since at $t_{\rm b} = 0$ there are no entanglements across the interface, and after equilibration the bulk-like entanglement density is achieved, we can interpret the increase in $(h_{\rm c}/h)^2$ as a direct measure of the change in entanglement density across the interface.

Here we consider the scenario in which a molecule is most severely confined by the entropic interface. This occurs when the molecule's centre of mass would have been found at the location of the interface in the absence of a barrier (see fig. 1(b)). In this case, the chain's average pervaded volume is exactly half of that in the bulk. Since a molecule in this state is maximally perturbed, this scenario provides an upper bound on the time it takes the bilayers to lose memory of the entropic interface. Even though polymer chains are confined near a reflecting boundary, we expect the molecules to move predominantly by reptation. This is the assumption that has been made in models used to explain, for example, the recovery of fracture toughness of polymer-polymer interfaces, and more generally the diffusive processes across these interfaces [7, 36, 37]. A molecule that is maximally perturbed must relax such that its pervaded volume increases by a factor of two. By analogy with molecular relaxation in the bulk, the molecule must diffuse by a distance of roughly $R_{\rm ee}/2$ to lose the memory of its confinement. Notwithstanding the possibility that the dynamics of polymer chains at an interface may be altered by confinement [28], the diffusion equation dictates that the time it takes for a typical bulk polymer chain to diffuse by a distance $R_{\rm ee}/2$ corresponds to a time $\tau_{\rm rep}/4$. Thus, by making a simple bulk reptation argument, and invoking the reflection principle, we find that the maximum time taken to lose memory of the bilayer interface is less than $\tau_{\rm rep}$. In fig. 5, we have inserted a vertical dashed line at $t_{\rm b} = \tau_{\rm rep}/4$. The data has clearly saturated by this time. The relaxation time that we measure, $\tau_{\rm b}$, is representative of the average relaxation time for perturbed chains near the interface, with $\tau_{\rm rep}/4$ being an upper bound.

3.3 Equilibria of as-cast monolayer and bilayer films

A condition for equilibrium is that a system can arrive at the state independent of the initial condition. In the previous two sections of this work, we have described the preparation and evolution towards equilibrium of two non-equilibrium states: as-cast monolayer films and bilayers prepared with an entropic interface. In both cases, we observe that after a sufficient relaxation time $(h_{\rm c}/h)^2$ reaches a plateau. Examining the long time behaviour of figs. 4 and 5 we see that, within error, both non-equilibrium systems reach the same plateau value having started from different initial conditions. That $(h_{\rm c}/h)^2$ is independent of the preparation after long annealing times is a strong indication that these films are at true equilibrium. To qualify this statement, we cannot rule out long term changes beyond the resolution of the crazing measurement.

4 Conclusion

We have performed a series of crazing measurements designed to probe non-equilibrium states of thin polymer films. In the first case, we examine the effect of spin coating on the resulting craze characteristic, $(h_{\rm c}/h)^2$. We find that the as-cast films display strongly non-equilibrium behaviour that is difficult to control even under seemingly identical initial conditions. The measured values of $(h_{\rm c}/h)^2$ can be reconciled with results from other researchers [16–19, 22, 23, 26] if we interpret the as-cast films as having trapped molecular configurations that are stretched compared to the equilibrium Gaussian statistics. Thermal annealing of these films results in an approach to a plateau in $(h_{\rm c}/h)^2$, and the equilibration time is consistent with relaxation on a time scale comparable to the polymer reptation time.

Having established that it is possible to prepare monolayer films with an equilibrium entanglement density, we measured $(h_{\rm c}/h)^2$ in bilayers prepared by stacking two monolayer films. Such a bilayer film is then chemically equivalent to a film with the thickness of two monolayers, but differs in that there is an entropic interface. The interface has no enthalpic penalty and only a diminished entropy due to fewer available molecular configurations.

The monolayers were chosen such that they confine the long chain molecules resulting in a reduced effective entanglement density, while a film of twice the monolayer thickness exhibits a bulk-like entanglement density. We find that the as-prepared bilayers craze in a way that is consistent with previously reported measurements on confined monolayers. Thermal annealing above T_g causes the entropic interface in the middle of the bilayer to heal, effectively converting the bilayer into a single film. The healing of the entropic interface occurs on a time scale that is shorter than one bulk reptation time.

Financial support from NSERC of Canada is gratefully acknowledged.

References

1. P.G. de Gennes, *Scaling Concepts in Polymer Physics* (Cornell University Press, 1979).
2. M. Rubinstein, R.H. Colby, *Polymer Physics* (Oxford University Press, 2003).
3. G.C. Berry, T.G. Fox, Adv. Polym. Sci. **5**, 261 (1968).
4. J.D. Ferry, *Viscoelastic Properties of Polymers*, 3rd edition (John Wiley & Sons, Inc., 1980).
5. T.C.B. McLeish, Adv. Phys. **51**, 1379 (2002).
6. A.E. Likhtman, T.C.B. McLeish, Macromolecules **35**, 6332 (2002).
7. H.H. Kausch, M. Tirrell, Annu. Rev. Mater. Sci. **19**, 341 (1989).
8. C. Creton, E.J. Kramer, H.R. Brown, C.-Y. Hui, Adv. Polym. Sci. **156**, 53 (2001).
9. E.J. Kramer, Adv. Polym. Sci. **52/53**, 1 (1983).
10. E.J. Kramer, L.L. Berger, Adv. Polym. Sci. **91/92**, 1 (1990).
11. H.R. Brown, Macromolecules **24**, 2752 (1991).
12. H.R. Brown, T.P. Russell, Macromolecules **29**, 798 (1996).
13. L. Si, M.V. Massa, K. Dalnoki-Veress, H.R. Brown, R.A.L. Jones, Phys. Rev. Lett. **94**, 127801 (2005).
14. F. Brochard-Wyart, P.G. de Gennes, H. Hervet, C. Redon, Langmuir **10**, 1566 (1994).
15. O. Bäumchen, R. Fetzer, K. Jacobs, Phys. Rev. Lett. **103**, 247801 (2009).
16. D.R. Barbero, U. Steiner, Phys. Rev. Lett. **102**, 248303, (2009).
17. K.R. Thomas, A. Chenneviere, G. Reiter, U. Steiner, Phys. Rev. E **83**, 021804 (2011).
18. R.N. Li, A. Clough, Z. Yang, O.K.C. Tsui, Macromolecules **45**, 1085 (2012).
19. A. Clough, M. Chowdhury, K. Jahanshahi, G. Reiter, O.K.C. Tsui, Macromolecules **45**, 6196 (2012).
20. S.G. Croll, J. Appl. Polym. Sci. **23**, 847 (1979).
21. G. Reiter, M. Hamieh, P. Damman, S. Sclavons, S. Gabriele, T. Vilmin, E. Raphaël, Nat. Mater. **4**, 754 (2005).
22. P. Damman, S. Gabriele, S. Coppée, S. Desprez, D. Villers, T. Vilmin, E. Raphaël, M. Hamieh, S. Al Akhrass, G. Reiter, Phys. Rev. Lett. **99**, 036101 (2007).
23. A. Raegen, M. Chowdhury, C. Calers, A. Schmatulla, U. Steiner, G. Reiter, Phys. Rev. Lett. **105**, 227801 (2010).
24. K.R. Thomas, U. Steiner, Soft Matter **15**, 7839 (2011).
25. F. Closa, F. Zeibert, E. Raphaël, Phys. Rev. E **83**, 051603 (2011).
26. M. Chowdhury, P. Freyberg, F. Zeibert, A.C.-M. Yang, U. Steiner, G. Reiter, Phys. Rev. Lett. **109**, 136102 (2012).
27. A. Silberberg, J. Colloid Interface Sci. **90**, 86 (1982).
28. H. Bodiguel, C. Fretigny, Phys. Rev. Lett. **97**, 266105 (2006).
29. L.J. Fetters, D.J. Lohse, D. Richter, T.A. Witten, A. Zirkel, Macromolecules **27**, 4639 (1994).
30. L.J. Fetters, D.J. Lohse, W.W. Graessley, J. Polym. Sci. Polym. Phys. **37**, 1023 (1999).
31. J. Klein, Nature **12**, 144 (1978).
32. P.F. Green, E.J. Kramer, Macromolecules **19**, 1108 (1986).
33. Y. Liu, G. Reiter, K. Kunz, M. Stamm, Macromolecules **26**, 2134 (1993).
34. A. Karim, G.P. Felcher, T.P. Russell, Macromolecules **27**, 6973 (1994).
35. P.G. de Gennes, J. Chem. Phys. **35**, 572 (1971).
36. K. Jud, H.H. Kausch, J.G. Williams, J. Mater. Sci. **16**, 204 (1981).
37. S. Prager, M. Tirrell, J. Chem. Phys. **75**, 5194 (1981).
38. F. Brochard-Wyart. *Fundamentals of Adhesion*, Chapter 6 (Plenum Press, New York, 1991).
39. F. Pierce, D. Perahia, G.S. Grest, EPL **95**, 46001 (2011).
40. J. Rottler, M.O. Robbins, Phys. Rev. E. **68**, 011801 (2003).
41. J. Rottler, J. Phys.: Condens. Matter **21**, 463101 (2009).
42. H.R. Brown, J. Mater. Sci. **14**, 237 (1979).
43. B.D. Lauterwasser, E.J. Kramer, Philos. Mag. A **39**, 469 (1979).
44. J.D. McGraw, K. Dalnoki-Veress, Phys. Rev. E **82**, 021802 (2010).
45. A.M. Donald, E.J. Kramer, J. Polym. Sci. Part B: Polym. Phys. **20**, 899 (1982).
46. A.M. Donald, E.J. Kramer, Polymer **23**, 461 (1982).
47. A.C.-M. Yang, E.J. Kramer, C.C. Kuo, S.L. Phoenix, Macromolecules **19**, 2020 (1986).
48. A.G. Emslie, F.T. Bonner, L.G. Peck, J. Appl. Phys. **20**, 858 (1958).
49. A. Bach, K. Almdal, H.K. Rasmussen, O. Hassager, Macromolecules **36**, 5174 (2003).
50. S. Napolitano, M. Wübbenhorst, Nat. Commun. **2**, 260 (2011).
51. J.P. Cotton, D. Decker, H. Benoit, B. Farnoux, J. Higgins, G. Jannink, R. Ober, C. Picot, J. des Cloizeaux, Macromolecules **7**, 863 (1974).

Chapter 4

Conclusions

In this thesis the results of three types of experiments are presented. First, in Paper 1 we address the formation of non-uniform spincast polymer films. We find the the formation of instabilities during spincoating is dependent on temperature. Furthermore, our results indicate that non-uniform spincast films form as a result of a Marangoni process. Finally, we show the non-uniformities in the film thickness can be entirely avoided simply by spincoating at cooler temperatures.

In Papers 2 and 3 we prepare polymer films with non-uniform surface geometries. Above T_g, gradients in the Laplace pressure drive the surface to level. We follow the evolution of the film height profiles using AFM and compare the results with the theoretical predictions of the two-dimensional capillary driven thin film equation. In Paper 2 we prepare films with small surface perturbations and find that the perturbations converge to a universal self-similar attractor, regardless of initial condition, as predicted by theory. The convergence time depends on the volume on the perturbation. In Paper 3 we study samples with a rectangular trench geometry. At long times, we observe a cross-over in the levelling dynamics that can be understood by considering the boundary conditions governing the flow.

Finally, in Paper 4 we have used crazing to probe non-equilibrium entanglement networks. Our results indicate the chain conformations in spincast films are highly stretched compared to Gaussian chains. We find that annealing the films above T_g for times on the order of one reptation is sufficient for chains to equilibrate. In a second experiment we confine polymers to films with a thickness that is thinner than the equilibrium size of the molecule. In the glassy state, we stack two such films to create a bilayer. On either side of the mid-plane of the bilayer the chain conformations are restricted, which results in a loss of entropy. As we anneal the bilayer above T_g the 'entropic interface' heals as chains from the two layers entangle with one another. It takes less than one reptation time for the interface to heal and the bilayer to become indistinguishable from a single film.

Bibliography

[1] P.G. de Gennes, F. Brochard-Wyart, and D. Quéré. *Capillarity and Wetting Phenomena*. Springer, 2002.

[2] P. G. de Gennes. *Scaling concepts in polymer physics*. Cornell University Press, Ithaca, N.Y., 1979.

[3] R. A. L. Jones. *Soft condensed matter*. Oxford University Press, USA, 2002.

[4] M. Rubinstein and R. H. Colby. *Polymer Physics*. Oxford University Press, 2003.

[5] J. P. Cotton, D. Decker, H. Benoit, B. Farnoux, J. Higgins, G. Jannink, R. Ober, C. Picot, and J. Des Cloizeaux. Conformation of polymer chain in the bulk. *Macromolecules*, 7(6):863–872, 1974.

[6] R. L. Jones, S. K. Kumar, D. L. Ho, R. M. Briber, and T. P. Russell. Chain conformation in ultrathin polymer films. *Nature*, 400(6740):146–149, 1999.

[7] L. J. Fetters, D. J. Lohse, D. Richter, T. A. Witten, and A. Zirkel. Connection between polymer molecular weight, density, chain dimensions, and melt viscoelastic properties. *Macromolecules*, 27(17):4639–4647, 1994.

[8] A. E. Likhtman and M. Ponmurugan. Microscopic Definition of Polymer Entanglements. *Macromolecules*, 47(4):1470–1481, 2014.

[9] J. Klein. Evidence for reptation in an entangled polymer melt. *Nature*, 271:143–145, 1978.

[10] A. Bach, K. Almdal, H. K. Rasmussen, and O. Hassager. Elongational Viscosity of Narrow Molar Mass Distribution Polystyrene. *Macromolecules*, 36(14):5174–5179, 2003.

[11] J. D. McGraw, N. M. Jago, and K. Dalnoki-Veress. Capillary levelling as a probe of thin film polymer rheology. *Soft Matter*, 7(17):7832, 2011.

[12] J. D. McGraw, T. Salez, O. Bäumchen, E. Raphaël, and K. Dalnoki-Veress. Self-Similarity and Energy Dissipation in Stepped Polymer Films. *Phys. Rev. Lett.*, 109(12):128303, 2012.

[13] S. Onogi, T. Masuda, and K. Kitagawa. Rheological properties of anionic polystyrenes. I. Dynamic viscoelasticity of narrow-distribution polystyrenes. *Macromolecules*, 3(2):109–116, 1970.

[14] L. J. Fetters, D. J. Lohse, S. T. Milner, and W. W. Graessley. Packing Length Influence in Linear Polymer Melts on the Entanglement, Critical, and Reptation Molecular Weights. *Macromolecules*, 32(20):6847–6851, 1999.

[15] E. Kramer and L. Berger. Fundamental processes of craze growth and fracture. *Advances in Polymer Science*, 90/91:1–68, 1990.

[16] E. J. Kramer. Microscopic and molecular fundamentals of crazing. *Advances in Polymer Science*, 52(3):1–56, 1983.

[17] A. M. Donald and E. J. Kramer. Craze microstructure and molecular entanglements in polystyrene-poly (phenylene oxide) blends. *Polymer*, 23(3):461–465, 1982.

[18] L. L. Berger and E. J. Kramer. Chain disentanglement during high-temperature crazing of polystyrene. *Macromolecules*, 20(8):1980–1985, 1987.

[19] A. C. M. Yang, E. J. Kramer, C. C. Kuo, and S. L. Phoenix. Crazes in diluted entanglement networks of polystyrene. *Macromolecules*, 19(7):2020–2027, 1986.

[20] H. R. Brown. Measurement of craze density by quantitative transmission electron microscopy. *Journal of Materials Science*, 14(1):237–239, 1979.

[21] A. M. Donald and E. J. Kramer. Effect of molecular entanglements on craze microstructure in glassy polymers. *Journal of Polymer Science: Polymer Physics Edition*, 20(5):899–909, 1982.

[22] L. Si, M. V. Massa, K. Dalnoki-Veress, H. R. Brown, and R. A. L. Jones. Chain Entanglement in Thin Freestanding Polymer Films. *Phys. Rev. Lett.*, 94(12):127801, 2005.

[23] J. McGraw and K. Dalnoki-Veress. Swelling molecular entanglement networks in polymer glasses. *Phys. Rev. E*, 82(2):021802, 2010.

[24] J. Rottler and M. Robbins. Growth, microstructure, and failure of crazes in glassy polymers. *Phys. Rev. E*, 68(1):011801, 2003.

[25] J. Rottler. Fracture in glassy polymers: a molecular modeling perspective. *J. Phys.: Condens. Matter*, 21(46):463101, 2009.

[26] P. G. de Gennes. Wetting: statics and dynamics. *Rev. Mod. Phys.*, 57:827–863, 1985.

[27] A. Marchand, J. H. Weijs, J. H. Snoeijer, and B. Andreotti. Why is surface tension a force parallel to the interface? *Am. J. Phys.*, 79(10):999, 2011.

[28] A. Oron, S. H. Davis, and S. G. Bankoff. Long-scale evolution of thin liquid films. *Rev. Mod. Phys.*, 69(3):931, 1997.

[29] T. Salez, J. D. McGraw, O. Bäumchen, K. Dalnoki-Veress, and E. Raphaël. Capillary-driven flow induced by a stepped perturbation atop a viscous film. *Phys. Fluids*, 24(10):102111, 2012.

[30] T. Salez, J. D. McGraw, S. L. Cormier, O. Bäumchen, K. Dalnoki-Veress, and E. Raphaël. Numerical solutions of thin-film equations for polymer flows. *Eur. Phys. J. E*, 35(11):114, 2012.

[31] M. Benzaquen, T. Salez, and E. Raphaël. Intermediate asymptotics of the capillary-driven thin-film equation. *Eur. Phys. J. E*, 36(8):82, 2013.

[32] J. D. McGraw. *Non-Equilibrium Topographies: Surface Tension Driven Flows Reveal Polymer Properties at the Nanoscale.* PhD thesis, McMaster University, 2013.

[33] J. R. A. Pearson. On convection cells induced by surface tension. *J. Fluid Mech*, 4(5):489–500, 1958.

[34] R. Craster and O. Matar. Dynamics and stability of thin liquid films. *Rev. Mod. Phys.*, 81(3):1131–1198, 2009.

[35] N. Bassou and Y. Rharbi. Role of BénardMarangoni Instabilities during Solvent Evaporation in Polymer Surface Corrugations. *Langmuir*, 25(1):624–632, 2009.

[36] M. F. Schatz, S. J. Vanhook, W. D. McCormick, J. B. Swift, and H. L. Swinney. Onset of surface-tension-driven Bénard convection. *Phys. Rev. Lett.*, 75(10):1938, 1995.

[37] M. F. Schatz and G. P. Neitzel. Experiments on thermocapillary instabilities. *Annual review of fluid mechanics*, 33(1):93–127, 2001.

[38] P. G. de Gennes. Instabilities during the evaporation of a film: Non-glassy polymer+ volatile solvent. *Eur. Phys. J. E*, 6(1):421–424, 2001.

[39] H. Bodiguel and C. Fretigny. Reduced Viscosity in Thin Polymer Films. *Phys. Rev. Lett.*, 97(26):266105, 2006.

[40] K. Shin, S. Obukhov, J. Chen, J. Huh, Y. Hwang, S. Mok, P. Dobriyal, P. Thiyagarajan, and T. P. Russell. Enhanced mobility of confined polymers. *Nat Mater*, 6(12):961–965, 2007.

[41] K. Thomas, A. Chenneviere, G. Reiter, and U. Steiner. Nonequilibrium behavior of thin polymer films. *Phys. Rev. E*, 83(2):021804, 2011.

[42] K. R. Thomas and U. Steiner. Direct stress measurements in thin polymer films. *Soft Matter*, 7(17):7839, 2011.

[43] A. Raegen, M. Chowdhury, C. Calers, A. Schmatulla, U. Steiner, and G. Reiter. Aging of Thin Polymer Films Cast from a Near-Theta Solvent. *Phys. Rev. Lett.*, 105(22):227801, 2010.

[44] G. Reiter, M. Hamieh, P. Damman, S. Sclavons, S. Gabriele, T. Vilmin, and E. Raphaël. Residual stresses in thin polymer films cause rupture and dominate early stages of dewetting. *Nat Mater*, 4(10):754–758, 2005.

[45] R. N. Li, A. Clough, Z. Yang, and O. K. C. Tsui. Equilibration of Polymer Films Cast from Solutions with Different Solvent Qualities. *Macromolecules*, 45(2):1085–1089, 2012.

[46] D. R. Barbero and U. Steiner. Nonequilibrium Polymer Rheology in Spin-Cast Films. *Phys. Rev. Lett.*, 102(24):248303, 2009.

[47] P. Damman, S. Gabriele, S. Coppée, S. Desprez, D. Villers, T. Vilmin, E. Raphaël, M. Hamieh, S. Akhrass, and G. Reiter. Relaxation of Residual Stress and Reentanglement of Polymers in Spin-Coated Films. *Phys. Rev. Lett.*, 99(3):036101, 2007.

[48] D. P. Birnie. Rational solvent selection strategies to combat striation formation during spin coating of thin films. *J. Mater. Res.*, 16(04):1145–1154, 2011.

[49] P. G. de Gennes. Solvent evaporation of spin cast films:“crust” effects. *Eur. Phys. J. E*, 7(1):31–34, 2002.

[50] P. Müller-Buschbaum, J .S. Gutmann, M. Wolkenhauer, J. Kraus, M. Stamm, D. Smilgies, and W. Petry. Solvent-Induced Surface Morphology of Thin Polymer Films. *Macromolecules*, 34(5):1369–1375, 2001.

[51] P. Müller-Buschbaum, J. S. Gutmann, J. Kraus, H. Walter, and M. Stamm. Suppression of Roughness Replication in Bilayer Films Prepared by Spin-Coating. *Macromolecules*, 33(2):569–576, 2000.

[52] P. Müller-Buschbaum and M. Stamm. Correlated roughness, long-range correlations, and dewetting of thin polymer films. *Macromolecules*, 31(11):3686–3692, 1998.

[53] K. E. Strawhecker, S. K. Kumar, J. F. Douglas, and A. Karim. The Critical Role of Solvent Evaporation on the Roughness of Spin-Cast Polymer Films. *Macromolecules*, 34(14):4669–4672, 2001.

[54] C. Wang and S. Yen. Theoretical analysis of film uniformity in spinning processes. *Chemical engineering science*, 50(6):989–999, 1995.

[55] D. E. Bornside, C. W. Macosko, and L. E. Scriven. Spin coating: One-dimensional model. *J. Appl. Phys.*, 66(11):5185, 1989.

[56] T. Ge, F. Pierce, D. Perahia, G. S. Grest, and M. O. Robbins. Molecular Dynamics Simulations of Polymer Welding: Strength from Interfacial Entanglements. *Phys. Rev. Lett.*, 110(9):098301, 2013.